

Refined Adaptive Optics simulation with wide field of view for the E-ELT

Manal Chebbo

▶ **To cite this version:**

Manal Chebbo. Refined Adaptive Optics simulation with wide field of view for the E-ELT. Instrumentation and Methods for Astrophysic [astro-ph.IM]. Aix-Marseille Université, 2012. English. NNT : . tel-00742873

HAL Id: tel-00742873
https://theses.hal.science/tel-00742873

Submitted on 18 Oct 2012

HAL is a multi-disciplinary open access archive for the deposit and dissemination of scientific research documents, whether they are published or not. The documents may come from teaching and research institutions in France or abroad, or from public or private research centers.

L'archive ouverte pluridisciplinaire **HAL**, est destinée au dépôt et à la diffusion de documents scientifiques de niveau recherche, publiés ou non, émanant des établissements d'enseignement et de recherche français ou étrangers, des laboratoires publics ou privés.

ÉCOLE DOCTORALE ”PHYSIQUE ET SCIENCES DE LA MATIÈRE”
UNIVERSITÉ AIX-MARSEILLE

THÈSE DE DOCTORAT

présentée pour obtenir le grade de
docteur de l'Université Aix-Marseille
Spécialité: *Optique, Photonique et traitement d'image*

par

MANAL CHEBBO

SIMULATION FINE D'OPTIQUE ADAPTATIVE A TRES GRAND CHAMP POUR DES GRANDS ET FUTURS TRES GRANDS TELESCOPES

Encadrée et
dirigée par

Brice Le ROUX
& Marc FERRARI

et soutenue publiquement le 24 septembre 2012
devant le jury composé de

M. Philippe Amram	Président
M. Marcel Carbillet	Examinateur
M. Marc Ferrari	Directeur de thèse
M. Richard Myers	Rapporteur
M. Roberto Ragazzoni	Rapporteur
M. Brice Le Roux	Co-directeur
M. Jean-Francois Sauvage	Examinateur

Laboratoire d'Astrophysique de Marseille
Technopole de Château-Gombert
38, rue Frédéric Joliot-Curie
13388 Marseille cedex 13

إذا كنت لا ترى غير ما يكشف عنه الضوء ولا تسمع غير ما يُعلنُ عنه الصوت، فأنت في الحق لا تبصر ولا تسمع.

If you only see what the light reveals and only hear what sound announces, then truthfully you can neither see nor hear.
Gibran Khalil Gibran

Acknowledgment

Though only my name appears on the cover of this dissertation, a great many people have contributed to its production. I owe my gratitude to all those people who have made this dissertation possible and because of whom my graduate experience has been one that I will cherish forever.
First and foremost i express my profound sense of reverence to Thierry Fusco for his constant guidance, support, motivation and untiring help during the course of my PhD. I would never have been able to finish my dissertation without his help. A few discussions for a few time made the work plane for days.
My deepest gratitude is to my advisor Marc Ferrari, I have been amazingly fortunate to have him as an advisor, thanks for boosting my morale throughout the course of research. He has always been carying, a source of wisdom and motivation. He is a great leader.
I would like to thank Richard Myers and Roberto Ragazzoni for being my thesis referees, your evaluation and report was very reassuring and cheerful. And also a special thanks to Marcel Carbilet and Jean Francois Sauvage for beeing the examinors of my thesis and to Philippe Amram for beeing the president of my jury.
Now i jump back to Paris to thank the ONERA's team with whom I have interacted during one unforgettable year of my graduate studies. First of all i am grateful to Vincent Michau for accepting me among his team, a special thanks to Jean-Marc Conan, Laurent Mugnier, Clelia Robert, Cyril Petit and Serge Meimon for been always there to listen and give advices. I am deeply grateful to all of you for the long discussions that helped me sort out.
I am grateful to Jean-Francois Sauvage for his comments and constructive criticisms, he was more than a supervisor. Thanks for all the time he gave it to me, holding me to a high research standard and enforcing strict validations for each research result, and thus teaching me how to do research.
Always at DOTA-HRA, i would like to thanks all the PhD students: Amelie, Marie, Bruno, the special Rudolph, good luck for your PhD defense. Gaetano, our footballer Julietta, the hero Bertrand..... I am missing all of you especially our coffee time.

I would like always to thanks the LOOM team: Starting from my co-advisor Brice Le Roux, thanks for all any sort of help you made it for me, your care, being there to listen was very important. A special thanks to Frederic for his advise and help during the last stage of my PhD round, thanks for your comments and discussions. Thanks to Silvio and Pierre, i'll allways remember you.

Now i would like to thanks those with whom i shared the LAM life time: Many thanks to the LOOM's Girls PhD Mary and the lauréate Zalpha, a lot of memories that can never be forgotten (San Francisco at the Macy's center starting with the raspberry taste...., on s'est fait éclabousser avec Zalpha....), thanks for always being there to listen and help. Then i would like to thanks the LOOM's doctors, Manu, Arthur and Mamdu. A special thanks to Jeanne my officemate, she helps me developing my French language and tried

hard to understand the Libano-Franco language, thanks for all the frensh expressions that she teaches me. Many thanks to Flo, Jeanne, Zalpha, Audery, Emily, Claire the resto team ;). I would also like to thanks Fred and all the LAM administration for their help and adorable discussions. Thanks to Guill and Virginie the lovely couple, hope to see you one more time.

I would also like to thank my lovely friends Salam, Widad, Mhmd, Iman, Kamar, Hanan, Rayan and Nour. Thanks for always being there to help and support me facing all the troubles, you were like family. Without you by my side i would never be able to survive.

For my family:

لن أجد الكلمات التي يمكن إن تعبر عن مدى امتناني وتقديري لكم ، وسوف لن تكفيني
أوراق لشكركم ، امي وبيي ، سليم محمد وأحمد يا أغلى من في حياتي....

And finally an affectionate thought to my lover Jamil, who support me along the final trip of my study courses.

Résumé

La simulation fine de systèmes d'OA à grand champ de type MOAO, MCAO ou LTAO pour l'ELT se heurte à deux problématiques:

1. l'augmentation du nombre de degrés de liberté du système (au carré du diamètre du télescope). Cette augmentation rend les codes de simulation classiques peu (ou pas) utilisables, en particulier en ce qui concerne les processus d'inversion et de calcul matriciel. Il faut donc envisager des approches d'inversion itératives d'un modèle direct $y = A \times x$ en s'appuyant sur les théories d'optimisation à base de matrices creuses.

2. la complexité des systèmes, combinant des étoiles naturelles et laser, de grands miroirs déformables couvrant tous le champs et des miroirs dédiés dans les instruments eux-mêmes, des rotations différentielles de pupille et ou de champs. Cette complexité conduit aux développements de procédures nouvelles d'étalonnages, de filtrages et fusion de données, de commandes distribuée ou globale. Ces procédures doivent être simulées finement, comparées et quantifiées en termes de performances, avant d'être implantées dans de futurs systèmes.

Pour répondre à ces deux besoins. J'ai développé, en collaboration avec l'ONERA, un code de simulation complet basé sur une approche de résolution itérative de systèmes linéaires à grand nombre de paramètres (utilisation de matrices creuses). Sur cette base, j'ai introduit de nouveaux concepts de filtrage et de fusion de données (étoiles laser et étoiles naturelles) pour gérer efficacement les modes de tip/tilt/defoc dans le processus complet de reconstruction tomographique. Ce code permettra aussi, à terme, de développer et tester des lois de commandes complexes (multi-miroir déformable et multi-champs) ayant à gérer la combinaison du télescope adaptatif et d'instrument post-focaux comportant eux aussi des miroirs déformables dédiés.
La première application de cet outil s'est faite naturellement dans le cadre du projet de spectrographe multi-objets EAGLE, un des instruments phares du futur E-ELT, qui, du point de vue de l'optique adaptative combinera l'ensemble de ces problématiques.

Abstract

Refined simulation tools for wide field AO systems (such as MOAO, MCAO or LTAO) on ELTs present new challenges. Increasing the number of degrees of freedom (scales as the square of the telescope diameter) makes the standard simulation's codes useless due to the huge number of operations to be performed at each step of the Adaptive Optics (AO) loop process. This computational burden requires new approaches in the computation of the DM voltages from WFS data. The classical matrix inversion and the matrix vector multiplication have to be replaced by a cleverer iterative resolution of the Least Square or Minimum Mean Square Error criterion (based on sparse matrices approaches).

Moreover, for this new generation of AO systems, concepts themselves will become more complex: data fusion coming from multiple Laser and Natural Guide Stars (LGS NGS) will have to be optimized, mirrors covering all the field of view associated to dedicated mirrors inside the scientific instrument itself will have to be coupled using split or integrated tomography schemes, differential pupil or/and field rotations will have to be considered, etc.

All these new entries should be carefully simulated, analysed and quantified in terms of performance before any implementation in AO systems. For those reasons i developed, in collaboration with the ONERA, a full simulation code, based on iterative solution of linear systems with many parameters (use of sparse matrices). On this basis, I introduced new concepts of filtering and data fusion (LGS / NGS) to effectively manage modes such as tip, tilt and defoc in the entire process of tomographic reconstruction. The code will also eventually help to develop and test complex control laws (Multi-DM and multi-field) who have to manage a combination of adaptive telescope and post-focal instrument including dedicated deformable mirrors.
The first application of this simulation tool has been studied in the framework of the EAGLE multi-object spectrograph project, one of the main instrument of the future E-ELT, which, in terms of adaptive optics combine all of these issues.

Contents

Acknowledgment **iii**

Introduction **5**

I Imaging through the atmosphere and the role of Adaptive Optics **9**

1 Observing through the atmosphere **11**

1.1 **Modeling Earth's Atmosphere** 11

1.1.1 Structure functions and refractive index fluctuations 12

1.1.2 Turbulence Models 14

1.1.3 Wave front distortion 14

1.2 Optical effect of Atmospheric Turbulence 16

1.2.1 Fried Parameter 16

1.2.2 Anisoplanatism effect 17

1.2.3 Strehl Ratio 18

1.3 Surface fitting method for characterizing the wave front aberrations 19

1.3.1 Zonal Representation 20

1.3.2 Modal Representation 20

2 Adaptive Optics in Astronomy **25**

2.1 Synopsis 25

2.2 Adaptive Optics Background 26

2.3 Concepts of adaptive optics system 26

2.4 Adaptive Optics Sub-Systems 27

2.4.1 Wave front sensor: Shack-Hartmann 28

2.4.2 Deformable Mirrors 30

2.4.3 Real Time Computer 31

2.4.4 Wave front Reconstruction: An inverse problem 32
2.4.5 Inverse problem: Estimation via the DM 34
2.4.6 Error Sources and AO limitations 35

3 New Concepts of AO **39**
3.1 Ground Layer Adaptive Optics (GLAO) 40
3.2 Multi-Conjugate Adaptive Optics (MCAO) 40
3.3 Laser Tomography Adaptive Optics (LTAO) 41
3.4 Multi-Object Adaptive Optics (MOAO) 43

II Simulation Tools for AO systems **45**

4 Simulation of Adaptive Optics systems **47**
4.1 Simulation needs 49
4.1.1 Why and how to simulate an AO system 49
4.1.2 Simulation costs 49
4.2 Different approaches for the AO simulation tools 50
4.2.1 Analytical Models: Error Budget 50
4.2.2 Pseudo-Analytical Models 51
4.2.3 End to End Models 55
4.2.4 Conclusion 58

5 Sparse End To End Simulator **59**
5.1 Introduction 60
5.2 High number of degrees of freedom : identifying the bottleneck 60
5.3 Sparse Matrix Technology Primer 62
5.3.1 Sparse matrix storage format 63
5.3.2 Conclusion 65
5.4 E2E-S Global Structure 65
5.4.1 Assumptions of the E2E-s simulation code 65
5.5 Description of the different modules 66
5.5.1 Configuration System 66
5.5.2 Atmospheric Turbulence 67
5.5.3 Wave Front Sensor Sparse-Model 68
5.5.4 Deformable Mirror Model 72

5.6 Sparse Wave Front Reconstruction . . . 77
5.6.1 Propagation $P^h_{s,\alpha}$ . . . 79
5.6.2 Maximum *A Posteriori* estimator . . . 80
5.6.3 Conclusion . . . 86
5.7 Validation of the code on an AO system . . . 87
5.7.1 First simulation: Turbulence Case study . . . 87

6 Conclusion **93**

III Challenges of AO with Tomography **95**

7 LASER Guide Stars **97**
7.1 Introduction . . . 97
7.1.1 Outline of problems . . . 97
7.1.2 Types of LGS . . . 98
7.2 *Tip, Tilt and Defocus* Indetermination . . . 100
7.2.1 Investigation methods for *tip, tilt and defocus* modes filtering . . . 100
7.2.2 Conclusion . . . 106
7.3 **Cone Effect issues** . . . 107
7.3.1 Description of the problem . . . 108
7.3.2 LGS hyperbolic projector . . . 109
7.3.3 Simulation of the cone effect . . . 111
7.3.4 Conclusion . . . 120

8 Merging Natural and Laser Guide Stars Data **123**
8.1 Split Tomography . . . 124
8.2 Integrated Tomography . . . 125
8.2.1 Characteristics of the numerical simulation . . . 125
8.2.2 Results and Conclusion . . . 127
8.3 Conclusion . . . 130

9 Simulation of an E-ELT instrument: EAGLE **131**
9.1 Description of the EAGLE Instrument . . . 132
9.2 EAGLE-like simulations . . . 133
9.2.1 Description and characterisation of the E2E-S EAGLE-like simulation . . . 133
9.2.2 EAGLE-like Results and conclusion . . . 134

Conclusion **137**

Version française **140**

A The sparse row-wise format **149**

B SOY library fine print **151**

B.1 Functions and Routines 151

Bibliography **154**

List of Figures

0.1 Galileo telescope (1610) 5

0.2 Title page of the first edition of Sidereal Messenger published by Galileo Galilei in March 1610. 5

1.1 Leonardo da Vinci illustration of the turbulence phenomena 12

1.2 C_n^2 profiles observed at Haute Provence Observatory 14

1.3 Effect of the turbulence on the image of a star: Compensated and uncompensated short exposure image 16

1.4 Principle of the anisoplanatism phenomena: the turbulence induced wave front distortion for two propagation paths, with only slightly different propagation directions is different (ESO courtesy). 19

1.5 Wave front modes for first 5 orders of Zernike polynomials 21

2.1 AO concept. Image credits: Lawrence Livermore National Laboratory and NSF Center for Adaptive Optics. 27

2.2 Sketch of the basic concept behind the Shack-Hartmann wave front sensor. Image credits: Visa Korkiakoski 2008 28

2.3 Right: Influence function sketch of a Stack Array Mirror (SAM) type mirror. Left: Concept of the SAM mirror type. 30

2.4 AO system error sources using an NGS as wave front reference. Diagram adapted from Hardy and Thompson (2000). 35

2.5 Limitation of the AO correction at the center of the FOV due to the anisoplanatism effect for different positions in an FOV of 60 arcsec. 36

3.1 The principle of GLAO : in this figure the turbulence is analysed in three sky directions and one DM conjugated to the pupil plane, providing a lower correction than an MCAO system but in a wide FOV (Courtesy ESO) 41

3.2 The principle of MCAO : in this figure three WFSS probe the volume of turbulence, WFC combines signals from all stars to command a given DM associated to a WFS (Courtesy ESO). 42

3.3 The principle of LTAO : in this figure the turbulence is analysed in two sky directions using Laser GS and one DM conjugated to the pupil plane, providing on-axis correction (Courtesy ESO) 42

3.4 The principle of MOAO : in this figure two WFS probe the volume of turbulence, the correction is then provided by a DM in an open loop (Courtesy ESO). 43

4.1 Modules of the software package CAOS and the spftware package MAOS used within the CAOS application in order to design a GLAO simulation. 57

5.1 Computing CAOS time characterization running on both octo and bi-processor 2.1GHZ, 480 min are required for a telescope of 42m on the octo-processor machine 61

5.2 Total time in terms of number of iterations. 62

5.3 Variation of the simulation time with number of layers. 62

5.4 Vector Matrix Multiplication (VMM) computing time 64

5.5 Ratio of allocated memory using sparse and full matrices 64

5.6 Variation of the DSP of the turbulent phase for different outer scale . . . 68

5.7 Illustration of the Fried geometry 69

5.8 Wave front errors resulting from the white wave front slope noise 70

5.9 variation of the residual wave front error in terms of SNR 71

5.10 Ds is calculated using the realistic WFS geometry model. Zonal representation for a system of 20 *20 subapertures, where 308 are fully or partly illuminated in the pupil 72

5.11 The IFs is set to zero beyond the second actuator from the center 74

5.12 Answer of the mirror to a tip mode 74

5.13 The IFs is set to zero beyond the third actuator from the center 74

5.14 Answer of the mirror to a tip mode 74

5.15 Minimisation of the mechanical coupling in terms of the residual phase formed by the DM of 14 linear actuators, using an iterative resolution with Jaccobi preconditionner 75

5.16 Comparision of the fitting error in terms of the number of actuators presented on the DM using the Fourier formalism or a numerical simulation with E2E-S, where the mechanical coupling is fixed to 45%. 76

5.17 Principle of an AO wide field of view system of a diameter D, using 3 turbulent layers and $n_{GS} = 3$ 77

5.18 Projector matrix model. 2 layers are presented, rays traced from the guide stars (GS) through the phase screens to obtain the total contribution in the telescope aperture plane. The blue phase in the telescope aperture is then the sum of φ_0 and φ_{0167}, this last is obtained by a bilinear interpolation given $\varphi_{0,1,6and7}$ 80

5.19 A sparse approximation of C_{kol}^{-1} represented for a grid of 50×50 in the pupil of the telescope, the matrix is 0.5 % filled. 83

5.20 The laplacian operator ∇^2 represented in sparse RCO scheme attains a sparseness of 0.2%. 83

5.21 Covariance matrix $F_s^T F_s$ of the sparse influence functions (8×8 actuators). Each row or column of the matrix corresponds to an actuator of the mirror. 88

5.22 Variance of the Zernike modes simulated and analytical, over 4000 iterations for the given parameters: $L_0 = 100m, D/r_0 = 7$. 89

5.23 PSD of the turbulent phase, generated by the mirror and the residual phase, The x-axis is on f/pitch. 89

5.24 Computational time in terms of the number of subaperture for a simple AO case running over 100 cycles, we plot for comparison in blue line the time needed by CAOS to achieve the simulation calibration and iterations. 90

7.1 Spot elongation: nonsymmetrical elongation at the WFS subaperture, each sees the LGS from different angle, at the edge of the telescope pupil the elongation is maximum. 98

7.2 Outgoing laser beacon is refracted by the tilt of the atmosphere and the incoming beam is refracted in the oposite direction to the outgoing laser beam. 101

7.3 Model scheme review the procedure to be used given the slopes vector S and finding the space parallel and orthogonal to the tip, tilt and defocus . 101

7.4 Projection of the turbulent phase onto the Zernike basis(solid line), the filtered phase (green triangles) 105

7.5 Comparison between a reconstructor used in our simulation(blue line) and the reconstructor via the WFS(green line), in the case where $M^\dagger$ is the generalized inverse of M 105

7.6 Projection of the filtered phase onto the KL basis 107

7.7 Propagation from the Laser spot at a finite distance and from a celestial object. As it is seen the volume lit by the LGS is different from the volume lit by a natural guide star which is represented by a cylinder (Courtesy ESO). 108

7.8 Principle of tomography using Laser Guide Star. The covered area of the atmosphere decreases with the layer's altitude. We present the NGS/LGS footprint. 110

7.9 Principle of the hyperbolic projector. Each turbulent layer is rescaled to the inverse of the cone compression factor, providing a non linear displacement of the center of each LGS footprint evaluated as $\alpha_{expand} = \alpha \times \frac{H}{H-h}$ relative to each layer altitude. 111

7.10 4 LGS configuration case for the MUSE simulation case 115

7.11 Strehl ratio at the center of the field given the measurements from LGS at different positions in the field, for comparison we plot the NGS case measurements. LTAO case is considered. 115

7.12 Highest LGS *metapupil* given 4 LGSs placed on the on-axis pupil cylinder, the unseen turbulence zone affect the optimal LGSs position 116
7.13 Strehl ratio at the center of the field of view for 6 guide stars placed on a circle of variable diameter, NGS performance is plotted for comparison . 117
7.14 Strehl ratio at the center of the field of view for 8 guide stars placed on a circle of variable diameter 117
7.15 6 LGS configuration in the FOV for the LTAO performance study at the center of the field 117
7.16 8 LGS configuration in the FOV for the LTAO performance study at the center of the field. 117
7.17 LGS performance at the center of the FOV, using 4, 6 and 8 LGSs as measurement sources, for a different configuration of Laser GSs in the field-of-view. 117
7.18 Analytical and numerical comparison using Tyler equation and the E2E-S, one layer is simulated with D/r0=67.5 at 500nm. 119
7.19 SR performance obtained at different wavelength under a good seeing (upper line) and median seeing conditions, compared to the theoretical one obtained with the analytical formula of Tyler. 120
7.20 SR performance evaluated in functions of the wavelength, one LGS is considered as source of measurements compared to 4 LGSs (upper line), where the cone effect is limited. 121

8.1 Split tomography architecture 125
8.2 Integrated tomography architecture. The TOMO block is built given the concatenation of both hyperbola-LGS and linear-NGS projectors. 125
8.3 Sketch of two LGSs placed on a cercle of 22 arcsec. 128
8.4 Mean square residual error, obtained at the center of the FOV for split and integrated methods. 128
8.5 Reconstruction given the HO LGS measurements and the LO LGS measurements 129
8.6 SR performance obtained at different wave length under a good seeing (upper line) compared to the theoretical one obtained with the analytical formula of Tyler using the fusion data HO/LO spherical distortion. 130

9.1 MOAO configuration using a combination of LGS and NGS to map the atmospheric turbulence. One DM is dedicated to each IFU. 132
9.2 EAGLE simplified edge launching geometry. 6 LGSs launched from 4 launching telescopes located 2m outside the pupil. 134
9.3 SR EAGLE-like simulation, calculated at 5 sky directions inside the 7.5 arcmin FOV. The correction is done by a DM conjugated to the pupil plane. We show the ten GSs used as source of measurements in yellow, and in dark the 14 scientific targets. 135

9.4 PSF profile for compensated turbulence of the EAGLE-LIKE simulation (blue line). The dark line shows the diffraction-limited PSF profile. 136

List of Tables

5.1 RCO format of the WFS matrix initialized to zero colomns, rows and entries, where Ns_valide2 is the total number of valid subaperture, dim_alt_px2 is the square of the phase grid size. 72

5.2 Preconditioned conjugate gradient solver for a symmetric positive definite sparse linear system, with Jacobi preconditioner M. This algorithm is implemented straight out of Numerical Recipes, with the matrix-vector multiplications carried out sparsely by the ruoxv(a,v) function. Note that when M is identity, PCG reduces to CG 86

5.3 Turbulence conditions for the considered study case 88

7.1 Turbulence parameters of the MUSE simulation case. 112

7.2 Turbulence parameters 119

7.3 Theoretical and numerical comparison of the cone effect using 1 LGS, 8 meter telescope is simulated under good seeing (r_0 = 0.25m). 119

9.1 Turbulence parameters of the EAGLE-like simulation case. 134

Table of acronyms

AO	Adaptive Optics
EAGLE	ELTAdaptive optics for GaLaxy Evolution
ELT	Extremely Large Telescope
E-ELT	European Extremely Large Telescope
ESO	European Southern Observatory
PSF	Point Spread Function
PSD	Power Spectral Density
RMS	Root Mean Square
FT	Fourier Transform
KL	Karhunen-Loëve
LSE	Least Square Error
MMSE	Minimum Mean Square Error
MAP	Maximum *A Posteriori*
TMT	Thirty Meter Telescope
VLT	Very Large Telescope
WFE	Wave Front Error
XAO	eXtreme Adaptive Optics
GLAO	Ground Layer Adaptive Optics
SCAO	Single Conjugate Adaptive Optics
MCAO	Multi Conjugate Adaptive Optics
LTAO	LASER Tomography Adaptive Optics
MOAO	Multi Object Adaptive Optics
LGS	Laser Guide Star
NGS	Natural Guide Star
E2E	End To End
FOV	Field Of View
SR	Strehl Ratio
RTC	Real Time Computer

Introduction

Phoenicians cooking on sand discovered glass around 3500 BCE, but it took about 5,000 years more for glass to be shaped into a lens for the first telescope. A spectacle maker probably assembled the first telescope. Hans Lippershey (c1570-c1619) of Holland is often credited with the invention. Hans Lippershey was not the first to make one, however, he was the first to make the new device widely known making a concrete demonstration of a telescope with magnification of just three times.

The news of this new invention spread rapidly through Europe, and the device itself quickly followed in September 1608. Once the telescope was known and began to spread, several people, including Thomas Harriot, turned it to the sky in early 1609 to observe celestial objects. But it was Galileo who made the instrument famous, who became the first man to see the craters of the moon, and who went on to discover sunspots, the four large moons of Jupiter, and the rings of Saturn with a telescope of 2 cm of diameter. Unfortunately, the history retains only Galileo's work, this latter published his observations in



Figure 0.1: Galileo telescope (1610)

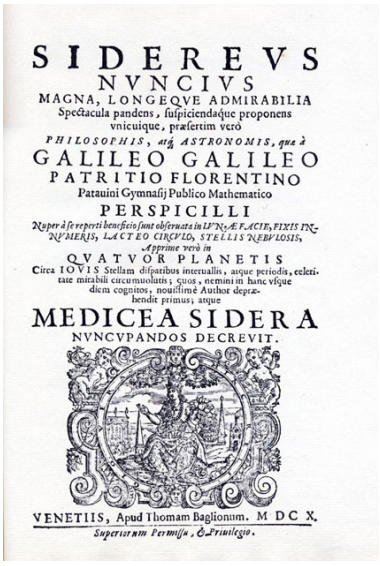

SIDEREVS
NVNCIVS
MAGNA, LONGEQVE ADMIRABILIA
Spectacula pandens, suspiciendaque proponens
vnicuique, præsertim verò
PHILOSOPHIS, atq; ASTRONOMIS, quæ à
GALILEO GALILEO
PATRITIO FLORENTINO
Patauini Gymnasij Publico Mathematico
PERSPICILLI
Nuper à se reperti beneficio sunt obseruata in LVNÆ FACIE, FIXIS IN-
NVMERIS, LACTEO CIRCVLO, STELLIS NEBVLOSIS,
Apprime verò in
QVATVOR PLANETIS
Circa IOVIS Stellam disparibus interuallis, atque periodis, celeri-
tate mirabili circumuolutis; quos, nemini in hanc vsque
diem cognitos, nouissimè Author deprã-
hendit primus; atque
MEDICEA SIDERA
NVNCVPANDOS DECREVIT.
VENETIIS, Apud Thomam Baglionum. M DC X.
Superiorum Permissu, & Priuilegio.

Figure 0.2: Title page of the first edition of Sidereal Messenger published by Galileo Galilei in March 1610.

a modern style *Sidereus Nuncius* or Sidereal Messenger (figure 0.2) in english in Marsh 1610. Today, the diameters of the telescopes are about 10 meters and multiple projects aim to build telescopes from 30 to 50 meters in diameter.

This dramatic evolution has two fundamental reasons: the total flux collected by a telescope is proportional to its surface and its angular resolution is proportional to its diameter. A larger aperture D not only increases the amount of light collected, but also reduces the diameter of an image of an unresolved star so that its peak intensity increases as D^4. However, on ground the telescope resolution is limited in the visible to the one of a telescope of 10 cm of diameter. This paradox is due to the atmospheric turbulence, which perturbates the formation of images.

Several approaches have been proposed to go beyond the resolution imposed by the atmosphere. The ”speckle interferometry", proposed by A. Labeyrie in 1970 [Labeyrie (1970)] is based on recording short exposures to overcome the limitation set by seeing. The images obtained are then analyzed in order to obtain the real resolution of the telescope. But these solution suffer from a poor signal to noise.
Adaptive optics (AO) is a technology used to compensate in real time the aberrations that occur when light propagates through an inhomogeneous medium. Currently its most important applications are in astronomy and in military domains, although also medical uses are becoming more and more important.
The genesis for AO was in 1953 when [Babcock (1953)] first proposed the use of a spatial light modulator to correct for aberrations introduced into images produced by ground-based telescopes due to atmospheric turbulence. However, it was not until 1970s before sufficiently sophisticated technologies became available at military fields [Tyson (1991)]. In 1977, a first AO system was reconstruct able to sharpen two-dimensional images of satellites placed on orbit [Hardy et al. (1977)]. The 19 actuator COME-ON (*Cge Observatoire de Paris-MEudon ONera*) [Kern et al. (1989), Rousset et al. (1990),Rigaut et al. (1992)] system was installed on the telescope in 1989 at La Silla in Chile. After then many AO systems have been installed on all large telescopes. At La Silla, COME-ON + [Rousset et al. (1992a),Rousset et al. (1994)] then ADONIS [Hubin et al. (1994)] have successively improved the first system COME-ON. The Hokupa’a [Roddier et al. (1994)] and PUEO [Arsenault et al. (1994), Rigaut et al. (1994)] systems have been installed on the Canada-France-Hawaii telescope at Mauna Kea in Hawaii, providing the astronomical community with high quality data.

The celestial light coming from a very distant object forms a plane wave front. When it propagates through the atmosphere, differences in the refractive index of air cause the shape of the wave front to change. The device measuring these deformations is called a Wave Front Sensor (WFS). Currently the main AO solutions are based on a closed-loop operation: the celestial light is reflected from a deformable mirror (DM) and one part of this light is directed to a scientific camera, one part to the WFS. The sensor measures the wave front distortions and the measurements are fed to a control system that computes new commands to be sent to the DM. The mirror then adapts to further reduce the residual distortions. This process thus iteratively compensates the atmospheric effects.

The advent of AO has breathed new life into the telescopes in which it has succeed to correct for the deleterious effects of atmospheric turbulence.
This AO success has prompted planners of the next generation of telescopes, dubbed Extremely Large Telescopes (ELTs), to plan for more AO developments.
Today AO systems are using large number of actuators (10^2,10^3), but AO for ELT yields to a very high number of actuators (10^4,10^5). This is due to both increasing telescope diameters and new higher-resolution applications planned for AO systems. On the other hand, current AO systems are using Vector Matrix Multiply (VMM) reconstructors to convert gradient measurements into an estimated phase. The computing for such a methods needs N^3 operations. This complexity requires optimization before good performance can be achieved. Unfortunately, increasing the number of degrees of freedom makes the standard codes useless due to the huge number of operations to be performed at each step of the AO loop process. This computational burden requires new approaches in the computation of the DM voltages from WFS data. The classical matrix inversion and the VMM have to be replaced by a cleverer iterative resolution of the Least Square (LS) or Minimum Mean Square Error (MMSE) criterion (based on sparse matrices approaches). Moreover, for this new generation of AO systems, concepts themselves will become more complex: data fusion coming from multiple Laser and Natural Guide Stars (LGS / NGS) will have to be optimized, mirrors covering all the Field Of View (FOV) associated to dedicated mirrors inside the scientific instrument itself will have to be coupled using split or integrated tomography schemes, differential pupil or/and field rotations will have to be considered, etc.

All these new entries should be carefully simulated, analysed and quantified in terms of performance before any implementation in AO systems. For those reasons we develop in collaboration with the ONERA, a full simulation code, based on iterative solution of linear systems with many parameters (use of sparse matrices). On this basis, it incorporates new concepts of filtering and data fusion (LGS , NGS) to effectively manage modes such as tip, tilt and defocus in the entire process of tomographic reconstruction. It will also help to develop and test complex control laws (multi-DM and multi-field) who have to manage a combination of adaptive telescope and post-focal instrument including dedicated deformable mirrors.

The thesis presented in this manuscript is dedicated to a **Refined Adaptive Optics simulation with wide field of view for the ELT**. We present the developement of an IDL-based End to End sparse (E2E-S) simulation tool. This E2E modelling of AO system includes atmospheric effects, telescope parameters, AO sub-system, as well as science observations at large FOV.
This dissertation presents three parts. The first part is dedicated to the study of phenomena responsible for the partial correction and anisoplanatism in adaptive optics. This study recall for both turbulence in chapter [1] and for the adaptive optics in chapter [2, 3]. This first part is therefore to introduce the general problem of the thesis and to study phenomena responsible for any performance degradation. In part [II], we present in chapter [4] different approaches for the AO simulation tools. We describe as well, the advantages and the limitations of the different existing E2E and analytical models. In chapter [5] we present the E2E-S, our main simulation tools, and what we can achieve with. This

simulator is used to quantify the global system performance, and also offers a detailed physical study of each sub-AO-system. E2E-S is a set of sparse IDL functions and routines, developed at LAM in collaboration with the ONERA AO team in Paris, to simulate the different AO components. These separated functions can be assembled freely to simulate various systems (OA ... MOAO) with various levels of complexity and degrees of freedom. It takes advantages of the sparse row wise format that brings down the computational load coming with the new generation of AO systems. All the functions have been developed during this thesis. The work consisted in developing a generator of turbulent wave front, a geometric sparse modelling of the WFS, mirror sparse modelling, the LGS implementations and the tip/tilt indetermination, and the LGS/NGS data fusion.
In part [III] we manage the LGS issues. In chapter [7] we propose new strategies for well managing Tip, Tilt and deFocus (TTF) modes. We propose a global study based on the configuration of LGS in the FOV to obtain the best performance of an LTAO system (LASER Tomography Adaptive Optics). New concepts of coupling between LGS and NGS in the entire process of tomographic reconstruction are proposed. Split tomography and integrated tomography are then compared. Fusion data for Low Order (LO) and High Order (HO) modes with and without TTF are also presented.
Chapter [9] is dedicated to the numerical simulation of the EAGLE instrument, two cases are presented (an EAGLE-like and a full EAGLE E2E-S simulations). For the EAGLE-like simulation, a 42m telescope is studied using 11 NGS in a wild FOV of 7.5 arcmin, and considering 9 turbulent thin layers and 83×83 sub-apertures per WFS.
Finally, a concluding chapter provides an overview and outlook of this research and proposes a number of points to explore.

Part I

Imaging through the atmosphere and the role of Adaptive Optics

Chapter 1

Observing through the atmosphere

When visible light or other electromagnetic radiation passes though a medium, local variations in the properties of that medium can lead to differences in how that light travels along different pathways through that medium. In a traveling wave front or beam of such radiation, this is perceived as distortions that can cause problems in trying to transmit or receive images, signals, or simply the energy itself through that medium. If the goal is to produce an image then these distortions may change the apparent shape and position of objects in that image, or degrade its overall resolution. Adaptive Optics (AO) was originaly designed to correct real-time optical effects of atmospheric turbulence and ameliorate the resolution. To better understand the framework within which AO was developed, it is necessary to recall basic notions related to atmospheric turbulence and its impact on image formation at the focus of a telescope. First, we recall the basics of theory to characterize atmospheric turbulence and fluctuations of the refractive index of the turbulent phase in part [1.1], and we characterize the optical effects of turbulence in part [1.2]. Then we care about the statistical properties of the turbulence decomposed onto the Zernike and the Karhunen Loëve basis in part [1.3].

1.1 Modeling Earth's Atmosphere

The movement of air masses of different densities within the Earth's atmosphere generates turbulent structures, making the atmosphere a turbulent medium. Fig 1.1 presents an illustration of the turbulence observed in water by Leonardo da Vinci, the first to attempt scientific study of turbulence.
Turbulence is a pure meteorological phenomena. The earth's atmosphere is in constant motion with a given kinetic energy, creating eddies characterized by an outer scale L_0 of tens to hundreds of meters. Turbulent motion is a stochastic process in the sense that density and velocity fluctuations emerge randomly so that the energy is transferred along a whole cascade of eddies of progressively decreasing size, down to a length scale l_0 at which energy is dissipated. Hence, the atmosphere shows turbulent behaviour on length scales between l_0 and L_0 , known as the inner and outer scales of turbulence, respectively. The area between these two characteristic sizes, where turbulence is totaly developed, is called as inertial subrange. These eddies will entails a mixture of air masses and hence



Figure 1.1: Leonardo da Vinci illustration of the turbulence phenomena

fluctuations in the refractive index of air, which directly affect the propagation of the wave front within the atmosphere. As a result, a previous knowledge of the physical characteristics of this domain allows us to well understand the effects of atmospheric turbulence on imaging in astronomy that leads to a loss of resolution while observing from the earth and at a visible wavelenght.
It is important to note that the theory of energy cascade was developed by [Kolmogorov (1941)]. The Kolmogorov model supposes that the turbulence is totaly developed, that is to say that the transfer of kinetic energy takes place at all spatial scales. This simple model, used for alot of studies doesn't take into consideration the inner and outer scales that both characterize the turbulence. When it is necessary to take into account the outer and inner scales it is better to refer to the Von Karman model [Karman (1948)]. This latter is used by default in this dissertation. In this section we care about the description of the statitical behavior given by the Von Karman model.

1.1.1 Structure functions and refractive index fluctuations

Many functions encountered in turbulence theory are non stationary and represent mean values that are continually changing over time, to avoid this variation the difference function $F(\tau) = f(t+\tau) - f(t)$ is used, so that $F(\tau)$ may be considered as a stationary random function of time, even though $f(t)$ is not. The structure function introduced by Kolmogorov in 1941 is also discussed in Tatarskii (1971). The structure function is then defined as

$$D_f(\tau) =< [F(\tau)]^2 >=< [f(t+\tau) - f(t)]^2 > \tag{1.1}$$

where <.> denotes the average value, the structure function is a measure of the intensity of the fluctuations in $f(t)$ over a period comparable to τ. In meteorology the pressure and the temperature have a mean value continually changing over time and space, producing a fluctuation of the refractive index of the atmosphere, this latter can be characterized by a structure function between two components of fluctuation of the refractive index $\Delta_n(r,h)$ separated by a distance ρ from its position r at a layer of altitude h:

$$D_{\Delta_n(\rho,h)} =< [\Delta_n(r,h) - \Delta_n(r+\rho,h)]^2 > \tag{1.2}$$

The statistics of the intensity of the fluctuation depends then only on the distance ρ between two points. This structure function related directly to the covariance matrix avoid the convergence of this latter at $\rho = 0$ while using the Kolmogorov model. [Corrsin (1951), Obukhov (1949)] demonstrate that, in the inertial subrange ($l_0 < \rho < L_0$), the structure function of the temperature fluctuations and then of the refracive index fluctuations can be evaluated as

$$D_{\Delta_n(\rho,h)} = C_n^2(h)\rho^{\frac{2}{3}} \tag{1.3}$$

where C_n^2 denotes the structure constant of the refractive index [units $m^{\frac{-2}{3}}$] that characterized the turbulence strenght. Moreover, the refractive index fluctuations can also be characterized statistically by its Power Spectral Density via a simple Fourier transform of the refractive index covariance function which is given by

$$W_{\Delta_{n,h}(f)} = 0.033(2\pi)^{\frac{-2}{3}} C_n^2(h) f^{\frac{-11}{3}} \tag{1.4}$$

Where f is the modulus of the spatial frequency f. This is the so-called Kolmogorov spectrum widely used in theoretical calculations, however it is limited to the inertial subrange so other models of the spectrum of the refractive-index fluctuations are required in order to cover the entire frequency domain. [Consortini et al. (1973), Chassat (1992)] proposed a model based on the spectrum of Von Karman, taking into consideration the inner and outer scales, Equation [1.5] changes to

$$W_{\Delta_{n,h}(f)} = 0.033(2\pi)^{\frac{-2}{3}} C_n^2(h)((\frac{1}{L_0})^2 + f^2)^{\frac{-11}{3}} exp - (fl_0)^2 \tag{1.5}$$

1.1.2 Turbulence Models

The structure constant of the refractive index C_n^2 appeared in equation 1.3 is a measurement of the turbulence strength. In practice C_n^2 is not constant as it varies with geographical location, altitude and time. The measurement of the C_n^2 provide a general property: the turbulence is mainly localized in certain layers. Assuming that the atmosphere consists of discrete independent turbulent layers, we move from a continuous profile of C_n^2 to a discontinuous profile. In this model, the electromagnetic wave passes successively through the different turbulent layers at altitudes h_i before reaching the ground. Thus, the C_n^2 profile provides informations about turbulence distribution in the different thin layers.

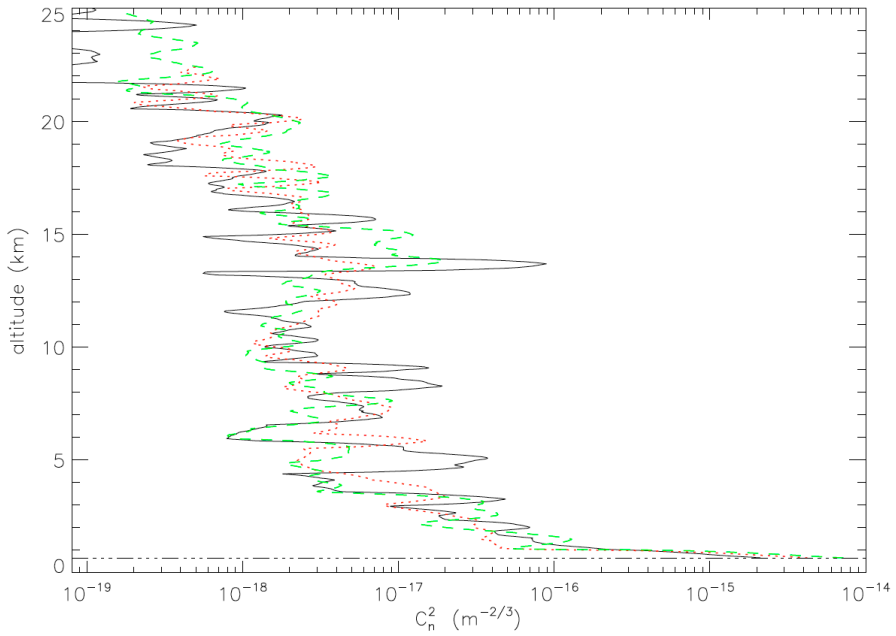


Figure 1.2: C_n^2 profiles observed at Haute Provence Observatory

Figure 1.2 shows some C_n^2 profiles measured by the team of LUAN [Dessenne (1998)] at Haute Provence Observatory (France) using a weather balloon. We can seen that the turbulence is strongly presented near the ground, and other layers of variable energy can be distinghuished around 5 and 15 km. Note that this profile change spatially (from one site to another) and temporally (between day and night), so that a regular updateing of the C_n^2 profile measurements is required for a precise knowledge of the turbulence properties.

1.1.3 Wave front distortion

It is important to analyze the effect of the variation of the refractive index on the wave front propagation, for a well comprehension of the effect of the turbulence on the image formation. As assumed in paragraph [1.1.2], the atmosphere is considered as a succession of discret statistically independent thin turbulent layers. To deduce the statistics of the turbulent phase from those of the refractive index we should make the simplifying

assumption that the amplitude fluctuations of the electromagnetic field are negligible, so that the amplitude change due to Fresnel propagation is neglected. This is the so-called near-field approximation [Roddier (1981)].
Given this approximation, the wave front propagation along the turbulence atmosphere is then the sum of the wave front distortion affected by all different thin layers

$$\phi^{tur}(r) = \sum_i \varphi^{tur}(r, h_i) \tag{1.6}$$

where ϕ represents the value of the wave front distortion at the pupil of the telescope and φ are a set of values representing the distortion wave front within the volume of turbulence. The wave front distortion propagating along a turbulent layer placed at height h of thickness δh is then affected by the turbulence present on this layer and it is then related to the optical path by the relation :

$$\phi^{tur}(r, h) = \frac{2\pi}{\lambda}\Delta_n(r, h)\delta h \tag{1.7}$$

from equation [1.3] and by adding the contribution of all the layers, for the Kolmogorov model the phase structure function at the telescope pupile plane is then given by

$$D_\phi(\rho) = 2.91\left(\frac{2\pi}{\lambda}\right)^2 \rho^{\frac{5}{3}} \int_0^\infty dh C_n^2(h) \tag{1.8}$$

$$D_\phi(\rho) = 6.88\left(\frac{\rho}{r_0}\right)^{5/3} \tag{1.9}$$

and the PSD is given by

$$W_\phi(\rho) = 0.033\,(2\pi)^{\frac{-2}{3}}\left(\frac{2\pi}{\lambda}\right)^2 f^{\frac{-11}{3}} \int_0^\infty dh C_n^2(h) \tag{1.10}$$

In the next section we care about all the parameters appeared in those developed expressions, that participate to the optical effect of atmospheric turbulence.

1.2 Optical effect of Atmospheric Turbulence

In this section we care about the influence of the turbulence on the propagation of a plane electromagnetic wave front. We remind some characteristic parameters of the turbulence, these quantities presented below determine the dimension of the AO system.

1.2.1 Fried Parameter

Fried parameter or Fried coherence lenght r_0 is another parameter that characterize the total turbulence strenght encountered by a wave front propagated through the different turbulent layers. For an initially flat wave front propagated through the Kolmogorov turbulent layer of thickness δh at height h this parameter is given by:

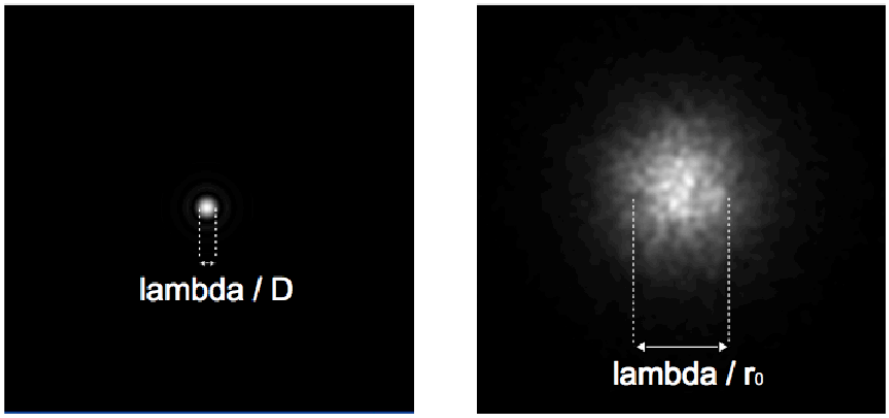


Figure 1.3: Effect of the turbulence on the image of a star: Compensated and uncompensated short exposure image

$$r_0 = \left(0.42 \times \left(\frac{2\pi}{\lambda}\right)^2 \frac{1}{cos\gamma} \int_0^\infty dh C_n^2(h)\right)^{-3/5} \tag{1.11}$$

which is a function of the turbulence strenght, zenith angle and wavelength.The Fried parameter is a measure of the aperture over which there is approximately 1 radian of rms phase aberration, so it is a crucial parameter for describing the seeing through a turbulent atmosphere. The seeing describes the theoretical angular resolution that can be reachable by a telescope of diameter larger than r_0, and its width is inversely proportional to the Fried parameter and it is given by equation 1.12.
We present in Figure 1.3 an illustration of a short exposure image of a star at the focal plane of the telescope. In the absence of wavefront distortion, the angular diameter of the image is determined by the diffraction limit of the telescope proportional to λ/D as

shown in figure 1.3 left. In the case of ground based imaging, the image is distorted by the atmospheric turbulence, and the angular size for short exposure, referred to as the seeing disk, is determined by the ratio λ/r_0 as depicted in figure 1.3 right.

$$d_{seing} = \frac{\lambda}{r_0}(rad) \tag{1.12}$$

The resolution of seeing-limited images obtained through an atmosphere with turbulence characterized by a Fried parameter r_0 is the same as the resolution of diffraction-limited images taken with a telescope of diameter r_0. Observations with telescopes much larger than r_0 are seeing-limited, whereas observations with telescopes smaller than r_0 are essentially diffraction-limited.

1.2.2 Anisoplanatism effect

The question that is addressed now is: will two stars that are very close together, yield the same instantaneous speckle pattern (of course, slightly shifted with respect to each other)? In fact, the light from two stars separated by an angle θ on the sky passes through different patches of the atmosphere and therefore experiences different phase variations. This angular anisoplanatism limits the field corrected by adaptive optics systems and causes phase decorrelation for off-axis objects in interferometers. This phenomena is illustrated in figure 1.4. To calculate the effect of anisoplanatism, we trace back the rays to two stars separated by an angle θ from the telescope pupil. They coincide at the pupil, and their separation r(d) at a distance d is θ d. At zenith angle γ, the distance is related to the height h in the atmosphere by $d = h.\frac{1}{cos\gamma}$. Now we evaluate the phase structure function

$$D_\phi(r) =< |\phi(0) - \phi(r)|^2 >= 2.91\left(\frac{2\pi}{\lambda}\right)^2 \frac{1}{cos\gamma} C_n^2(h)\delta h r^{5/3} \tag{1.13}$$

if we integrate over the height h, we obtain :

$$\begin{aligned} < \sigma_\varphi^2 > &= 2.91\left(\frac{2\pi}{\lambda}\right)^2 \frac{1}{cos\gamma}\int_0^\infty dh C_n^2(h)\left(\theta h\frac{1}{cos\gamma}\right)^{5/3} && (1.14)\\ &= 2.91\left(\frac{2\pi}{\lambda}\right)^2 \left(\frac{1}{cos\gamma}\right)^{8/3}\theta^{5/3}\int_0^\infty dh C_n^2(h)h^{5/3} && (1.15)\\ &= \left(\frac{\theta}{\theta_0}\right)^{5/3} && (1.16) \end{aligned}$$

Where θ_0 is defined as the *isoplanatic angle* for which the variance of the relative phase is 1 rad^2 [Fried (1982)]

$$\theta_0 = \left[2.91\left(\frac{2\pi}{\lambda}\right)^2\left(\frac{1}{cos\gamma}\right)^{8/3}\int_0^\infty dhC_n^2(h)hh^{5/3}\right]^{-5/3} \tag{1.17}$$

By comparing the definition of the Fried parameter r_0 and θ_0 we can write

$$\theta_0 = 0.314\frac{r_0}{\overline{H}} \tag{1.18}$$

Where

$$\overline{H} = \left(\frac{\int_0^\infty dhC_n^2(h)h^{5/3}}{\int_0^\infty dhC_n^2(h)}\right)^{3/5} \tag{1.19}$$

is the mean effective turbulence height. Equations 1.17 and 1.18 show that the isoplanatic angle is affected mostly by high-altitude turbulence; the anisoplanatism associated with ground layers and dome seeing is very weak. Moreover, we see that θ_0 scales with $\lambda^{6/5}$, but it depends more strongly on zenith angle than r_0. For r_0 = 20 cm and an effective turbulence height of 7 km, Eqn. 1.18 gives θ_0= 1.8 arcsec.

1.2.3 Strehl Ratio

The quality of an aberrated imaging system, or of the wave front after propagation through turbulence, is often measured by the Strehl ratio (SR). This quantity is defined as the on-axis intensity in the image of a point source divided by the peak intensity in a hypothetical diffraction-limited image taken through the same aperture. If the r.m.s phase error σ_φ is smaller than 2 rad, the SR can be approximated by the so-called *extended Marchal approximation*:

$$SR = exp(-\sigma_\varphi^2) \tag{1.20}$$

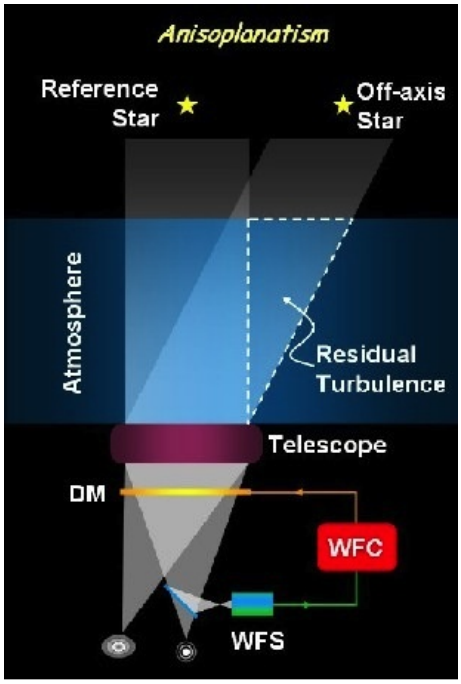


Figure 1.4: Principle of the anisoplanatism phenomena: the turbulence induced wave front distortion for two propagation paths, with only slightly different propagation directions is different (ESO courtesy).

1.3 Surface fitting method for characterizing the wave front aberrations

It was described by Ellerbroek (1994) that the phase-distortion profile $\phi(r)$ in the telescope's aperture plane or FOV is a continuous function defined on the Hilbert space. This phase distortion profile can be decomposed on a basis continuous function $(w_i)_i \in (N) : \mathbb{R}^2 \rightarrow \mathbb{R}$, thus the wave front surface may be written as

$$\phi(r) = \sum_{i=1}^{\infty} w_i(r)\varphi_i \tag{1.21}$$

It is important to decompose the wave front surface on a finit number of basis functions w_i, so that the phase distortion is represented by the vector space ϕ in $\mathbb{R}^2$. In this section we are going to present the different basis used to characterize the phase distortion profile, and that we are going to use in this dissertation. The E2E-S code is based on the Zonal aproach to represent the volumic turbulence as atmospheric grids, and we also needed the Karhunen-*Loëve* Modes taking advantages of the finit orthogonal decomposition.

1.3.1 Zonal Representation

The basis functions used in this approach are the interpolation functions with compact support. The wave front is described in optical path distance over a small area or zone and the turbulent layers are thus represented by a surface regular grid. That means we don't represent the frequency above the *Nyquist frequency*, i.e the surface of the phase distortion is filtered, the deformation of higher frequency are thus not considered. The phase is represented by a vector ϕ that are the coefficients calculated from a bilinear interpolation function, providing an inter pixelated displacement if necessary.
In this dissertation the phase distortion profile is represented by $N_{pix} \times N_{pix}$ regular grid surfaces of a randomly generated N_{pix}^2 values that respect the Von Karman model of turbulence. The vector phase are then the set of values seen by the telescopes aperture plane, we use the bilinear interpolation function to provide values at the intercepts of rays traced through phase atmospheric screens to the telescopes pupil plane.

1.3.2 Modal Representation

In the Modal approach, the wavefront surface is described in terms of a set of smoothly varying modes. These may be polynomials or other functions expansion over the pupil plane of the telescopes. Different bases can be utilized. It is possible to characterize the wave front distortion with the Karhunen-*Loëve* (KL) modes, which by definition allows a decomposition on a mode basis that are statistically independent . Or by decomposing the phase on the Zernike polynomials. In this dissertation we use both of these basis, the latter on which many theoretical studies have been conducted and allow to write the statistical properties of the turbulent phase [Noll (1976), Rigaut and Gendron (1992), Chassat (1992)]. This basis of Zernike modes has the advantage of being defined over a circular pupil and to write the most common optical aberrations. In addition we use the KL modes in chapter 7.2 for well managing modes such as tip,tilt, and defocus in the frame of the LGS measurements.

1.3.2.1 Zernike Polynomials

Zernike polynomials were introduced by Zernike on 1934 for his phase contrast method for testing the figure of circular mirrors [Zernike (1934)]. They were used by Nijboer [Nijboer (1942)] to study the effects of small aberrations on the diffraction images formed by rotationally symmetric systems with circular pupils. Noll used them to describe the aberrations introduced by Kolmogorov atmospheric turbulence. Today, they are in widespread use in optical design as well as in optical testing.
The aberration is defined on a full circular support and based on a representation in polar coordinates of the phase $r = (r, \theta)$ via the Zernike polynomials by

$$Z_i(\rho,\theta) = \sqrt{n+1}\begin{cases} R_n^m(r)\sqrt{2}cos(m\theta) & \text{if } m \neq 0 \text{ and } i \text{ odd} \\ R_n^m(r)\sqrt{2}sin(m\theta) & \text{if } m \neq 0 \text{ and } i \text{ even} \\ R_n^m(r) & \text{if } m = 0 \end{cases} \tag{1.22}$$

$$\mathbf{R_n^m} = \sum_{\mathbf{s=0}}^{\mathbf{(n-m)/2}} \frac{\mathbf{(-1)^s(n-s)!}}{\mathbf{s![(n+m)-s]![(n-m)-s]!}}\mathbf{r^{n-2s}} \tag{1.23}$$

Representation of some of the lower order Zernike aberrations can be seen in figure 1.5. The Zernike polynomials are commonly characterized by radial order n, and an azimuthal order m. Frequently, a continuous numeration with single index, j is used, instead of the two indices, n and m. For a given radial order N, there are a total of $(N+1)(N+2)/2$ Zernike polynomials. The power of Zernike modes comes from the fact that they are orthonormal over a circular pupil of surface S:

$$\frac{1}{S}\int_S Z_i(r) * Z_j(r)dr = \delta_{ij} \tag{1.24}$$

δ_{ij} is the Kronecker symbol, the product Z_iZ_j is equal to 1 if $i = j$ and zero otherwise.

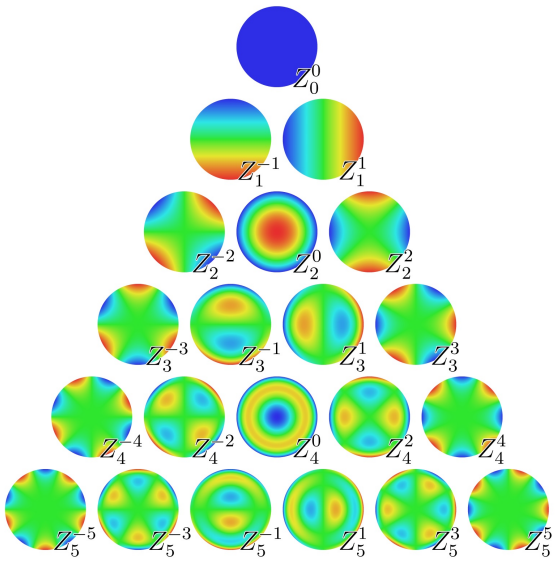


Figure 1.5: Wave front modes for first 5 orders of Zernike polynomials

1.3.2.1.1 Spatial characteristics of the wave front distortion decomposed on the Zernike The distortion profile can be decomposed onto the Zernike polynomials as :

$$\phi(r) = \sum_{i=1}^{\infty} a_i Z_i(r) \tag{1.25}$$

The base is orthonormal, thus the coefficients a_j of such decomposition we evaluated as

$$a_j = \frac{1}{S} \int_S \phi(r) Z_i(r) dr \tag{1.26}$$

It is possible to express the spatial and temporal properties of the phase on the Zernike basis assuming a statistics Kolmogorov turbulence. Using the expression of Fourier transforms of the Zernike polynomials, it is then possible to calculate the covariance matrix of the coefficients a_j as given by [Noll (1976)].

$$< a_i a_j > = 3.9[(n_i+1)(n_j+1)]^{\frac{1}{2}}(-1)^{(n_i+n_j-2m_i)/2}\delta_{ij}(\frac{D}{r_0})^{\frac{5}{3}} \tag{1.27}$$

$$\times \frac{2^{-\frac{14}{3}}\Gamma[\frac{14}{3}]\Gamma[(n_i+n_j-\frac{5}{3})/2]}{\Gamma[(-n_i+n_j+\frac{17}{3})/2]\Gamma[(n_i-n_j+\frac{17}{3})/2]\Gamma[(n_i+n_j+\frac{23}{3})/2]} \tag{1.28}$$

where D is the telescope diameter and the circular support of the polynomials, $\Gamma[x]$ denotes the Gamma function, n_i, n_j, m_i and m_j are respectively the radial and azimuthal orders of polynomials Z_i and Z_j. Using equation 1.25 we can write the residual error of the turbulent phase as

$$\sigma_\phi^2 = \frac{1}{S} \int_S < \phi^2(r) > dr = \sum_{i=1}^{\infty} < a_i^2 > \tag{1.29}$$

from expression of the amplitudes a_j the residual phase is then evaluated as

$$\sigma_\phi^2 \simeq 1.03 \left(\frac{D}{r_0}\right)^{5/3} \tag{1.30}$$

1.3.2.2 Karhunen-Loëve Modes

Another basis set that will be useful for our study is the basis of the Karhunen-Loëve functions, which like the Zernike are also orthogonal over a circular support, but are more appropriate as they have a diagonal covariance matrix. The KL expansion consists of modes that are a linear combination of Zernike polynomials and have statistically independent coefficients[Roggemann and Welsh (1995)]. In the KL basis the phase distortion profile is then decomposed over a finite number n of components and the equation (1.21) is expressed as

$$\bar{\phi}(r) = \sum_{i=1}^{n} w_i(r)\varphi_i \tag{1.31}$$

where n is the number of KL modes and $w_i(r)$ coefficients represent the weights given to each mode. For a Kolmogorov turbulence wave front distortion defined on an idealized circular telescope aperture, i.e., one not containing a central obscuration, unfortunately it is not that simple to calculate an analytical formula of the KL functions, but a numerical approximation is possible [Wang and Markey (1978)] in terms of the Zernike functions. [Lane and Tallon (1992)] have shown that when correcting more than about 20 modes the residual aberration start decreasing faster when using KL functions. In low order systems, this difference is negligible. Moreover, under Kolmogorov turbulence they are optimal for wave front decomposition in the sense that their expansion coefficients are statistically independent [Noll (1978)].

Chapter 2

Adaptive Optics in Astronomy

Contents

1.1 Modeling Earth's Atmosphere 11

1.1.1 Structure functions and refractive index fluctuations 12

1.1.2 Turbulence Models 14

1.1.3 Wave front distortion 14

1.2 Optical effect of Atmospheric Turbulence 16

1.2.1 Fried Parameter 16

1.2.2 Anisoplanatism effect 17

1.2.3 Strehl Ratio 18

1.3 Surface fitting method for characterizing the wave front aberrations 19

1.3.1 Zonal Representation 20

1.3.2 Modal Representation 20

1.3.2.1 Zernike Polynomials 20

1.3.2.1.1 Spatial characteristics of the wave front distortion decomposed on the Zernike 22

1.3.2.2 Karhunen-Loëve Modes 23

2.1 Synopsis

This chapter describes some major concepts and definitions of Adaptive Optics (AO). More complete presentations on this topic can be found in the literature [Roddier (1981)]. At first, a brief history is presented and the concept of AO is described in section 2.2, on which all of this dissertation will be based. We propose then in section 2.4 an illustration of the different sub-AO systems, providing the operating basis of each components for a better undertanding of the AO system behavior. Then we care about the wave front reconstruction given the WFS set of measurements, considering by default a Shack-Hartmann

(SH) WFS. Although many other sensors have been developped [Ragazzoni (1996), Roddier and Roddier (1988)], only SH is considered in this manuscript for the sake of simplicity.
Restoring the wave front distortion given the WFS data is an inverse problem which must be solved by using proper methods in order to improve the quality of the solution. We discuss in section [2.4.4] different approaches for the wave front aberration reconstruction, the commonly used (based on a least squares criterion) is presented, as well as more sophisticated approaches based on the consideration of a priori knowledge about the phase, and the phase statistics (Kolmogorov or von Karman). The remaining portions of this chapter will briefly discuss the limitation of an AO system, as some error sources degrade the AO performance. We describe these error sources and the consequences on the wave front distortion correction.

2.2 Adaptive Optics Background

The concept of AO was first proposed by [Babcock (1953)] to improve astronomical images otherwise degraded by the turbulence present in the atmosphere. AO systems correct for the deleterious effects of atmospheric turbulence. With AO, telescopes achieve diffraction-limited images (full-width, half maximum (FWHM) of $\sim \lambda/D$), rather than seeing-limited ($\sim$ 0.5-1 arcsec) images. Babcock suggested to use an active optical element to correct the instantaneous wave front distortions, after having measured them with a so-called wave front sensor which would deliver the signals necessary to drive the correcting device. But the limitaion of the technology did not allow to reconstruct such a system, till 1977. A first AO system was able to sharpen two-dimensional images of satellites placed on orbit [Hardy et al. (1977)]. The 19-actuator COME-ON (*Cge Observatoire de Paris-Meudon ONera*) [Kern et al. (1989), Rousset et al. (1990),Rigaut et al. (1992)] system was installed on the telescope at La Silla in Chile. After then many AO systems have been installed on all large telescopes. At La Silla, COME-ON + [Rousset et al. (1992a),Rousset et al. (1994)] then ADONIS (*ADaptive Optics Near Infrared System*) [Hubin et al. (1994)] have successively improved the first system COME-ON. The Hokupa'a [Roddier et al. (1994)] and PUEO (*Probing the Universe by Enhanced Optics*) [Arsenault et al. (1994), Rigaut et al. (1994)] systems have been installed on the Canada-France-Hawaii telescope at Mauna Kea in Hawaii, providing the astronomical community with high quality data.

2.3 Concepts of adaptive optics system

AO can be described as an optical system used to enhance the capabilities of a telescope by real-time closed-loop compensation of aberrations. In astronomy, AO is primarily used to compensate for the aberrations caused by atmospheric turbulence. In addition, AO can also be used to correct for wave front errors caused by optical fabrication errors, thermally induced distortions and misalignment errors. Whatever the distortion, it is important to

understand and characterize it before trying to compensate and correct it. A typical classical AO System consists of the following components: a DM, WFS, Real Time Computer (RTC). Those are illustrated in figure 2.1. A distorted wave front comes into the system through the telescope aperture. It is reflected from a deformable mirror to a beam splitter that divides the beam to a WFS and a scientific camera. The measurements from the WFS are fed to the RTC that computes the required instructions for the DM. The mirror is deformed using actuators, each of them having its own control voltage. The cycle from the WFS measurements to the mirror commands becomes typically an iterative process called closed-loop.

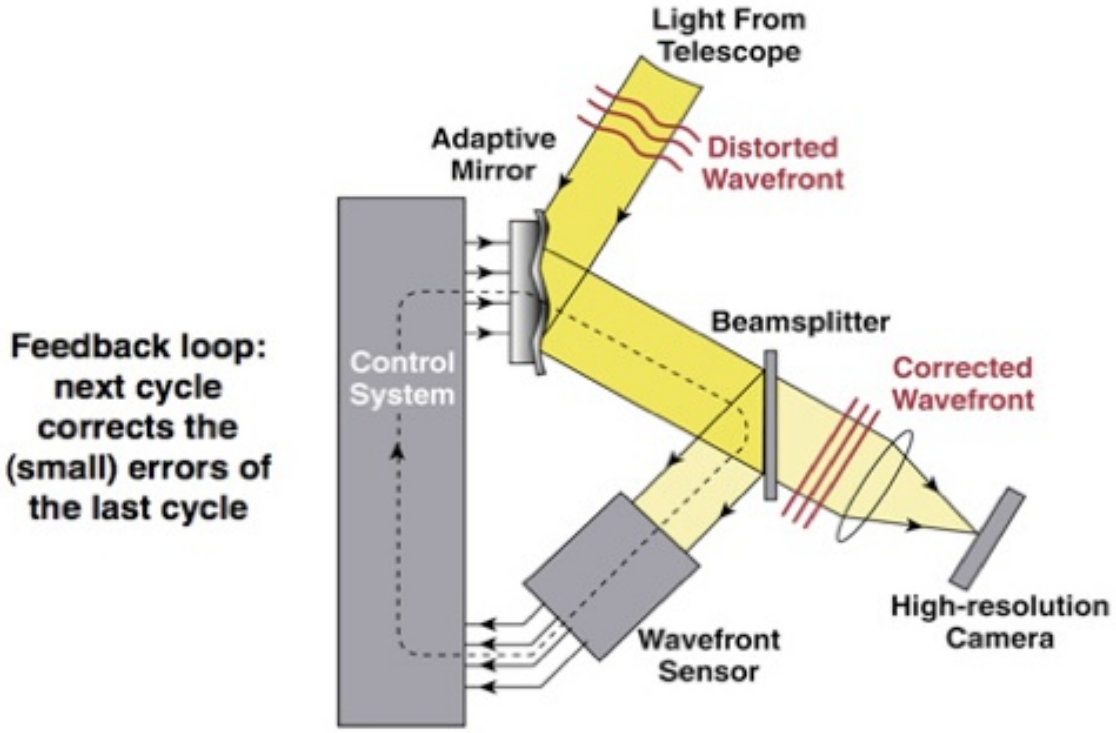


Figure 2.1: AO concept. Image credits: Lawrence Livermore National Laboratory and NSF Center for Adaptive Optics.

2.4 Adaptive Optics Sub-Systems

In general, most AO systems contain the required three key components, the WFS, the DM and the real time computer system. In this section we will call for all of these components, in order to propose in chapter 5 the sparse modules of the End-to-End Sparse simulator (E2E-S).

2.4.1 Wave front sensor: Shack-Hartmann

2.4.1.1 Description

As said above in this dissertation we care about the SH-WFS, it uses a variation on the traditional Hartmann test for real-time WF measurements. The concept of SH-WS is illustrated in figure 2.2. The wave front distortion is incident onto a two dimensional array of lenslets. Each subuperture produces a spot on a detector in the focal plane of the lenslet array. If no aberration, the image pattern is a grid of spots having constant intervals, thus if the wave front is turbulent, the spot will move with respect to this reference defined by the plane wave front. The movement of this spot on the camera provides information on the subaperture tilt (average slope) of the wave front seen by the subaperture. In fact this spot shift or displacement is directly proportional to the average derivative of the local phase and give a direct estimate of the angle of arrival (α_x, α_y) of the wave over each subaperture:

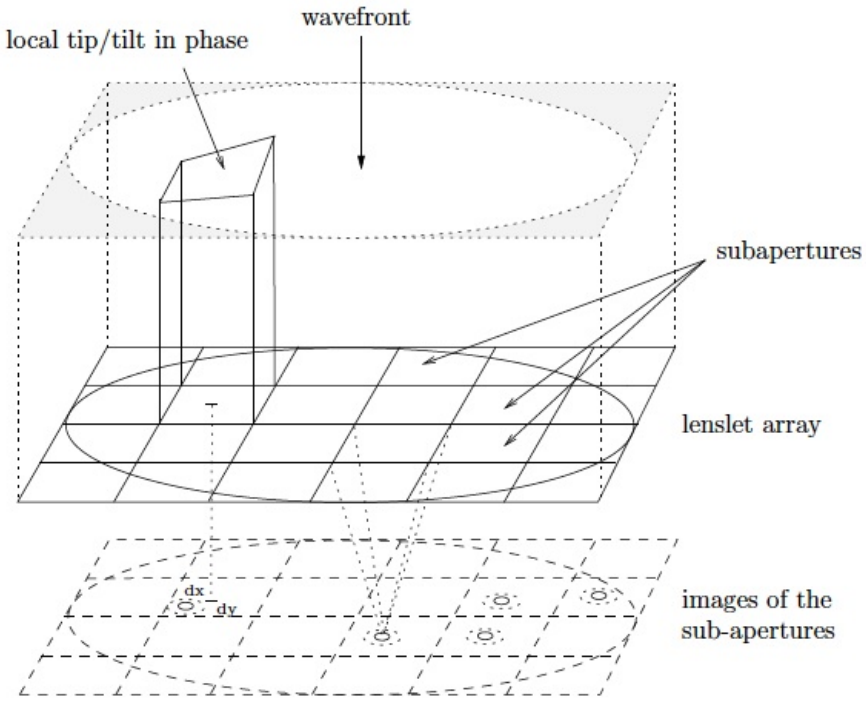


Figure 2.2: Sketch of the basic concept behind the Shack-Hartmann wave front sensor.
Image credits: Visa Korkiakoski 2008

$$\alpha_x = \frac{x_c}{f_{ml}} = \frac{\lambda}{2\pi S} \int\int_{sub\text{-}ap} \frac{\partial \varphi}{\partial x} dxdy \tag{2.1}$$

$$\alpha_y = \frac{y_c}{f_{ml}} = \frac{\lambda}{2\pi S} \int\int_{sub\text{-}ap} \frac{\partial \varphi}{\partial y} dxdy \tag{2.2}$$

where S is the surface of the subaperture, f_{ml} represents the focal of the lenslet and (x_c, y_c) represent the displacements of the center of gravity. These equations assume that the effect of scintillation is negligable. The displacement (x_c, y_c) are usually evaluated by measuring the center of Gravity (CoG) of the image spot created at the focus of sub-pupils by giving the position of reference obtained by calibration in the absence of turbulence. Several methods have been developed for the improvement of the measurement and to reduce the impact of the noise by thresholding and by windowing. This consists in using a circular window centered on the pixel with maximum intensity in order to remove the noisy pixels at the edge. There are also other techniques for estimating the image spot displacement, such as weighted COG [Fusco et al. (2004),Thomas et al. (2006)] involving a weighting function over each pixel for COG calculation, or correlation techniques [Michau et al. (1993), Poyneer et al. (2005)]. A more recent is the matched filter algorithm [Gilles and Ellerbroek (2006)].

2.4.1.2 Noise measurements

There is three main contributions on the WFS mesurement noises: photon noise, electrical noise in the detectors, and bias errors due to misalignment of the optics [Roddier (2004)]. The first is a Poisson process, the second is a Gaussian process. The photon noise on the measurements of the COG is given by:

$$\sigma^2_{phot} = \left(\frac{\pi}{\sqrt{2}}\right)^2 \frac{1}{N_{ph}} \left(\frac{X_T}{X_D}\right)^2 (rad^2) \tag{2.3}$$

where N_{ph} number of detected photoelectrons per subaperture (sum of all pixels), X_T is the FWHM of the subaperture Point Spread Function (PSF) and X_D is the FWHM of the diffraction-limited PSF.
The noise variance of the detector is given by

$$\sigma^2_{detect} = \left(\frac{\pi}{\sqrt{3}}\right)^2 \frac{\sigma_{e-}}{N_{ph}} \left(\frac{X_S^2}{X_D}\right)^2 (rad^2) \tag{2.4}$$

N_S^2 is the total number of pixels used in the COG computation after the sholding and windowing and σ_e, is the standard deviation of the detector noise, expressed in electron per pixel.

2.4.2 Deformable Mirrors

The Deformable Mirror (DM) corrects the aberrations caused by the atmospheric turbulence ϕ_{tur}, shaping its surface with a figure that nulls the shape of the wave front that passed through the atmosphere providing a new phase profile ϕ_{corr}. Different types of deformable mirrors have been developed over the last 30 years, a complete description can be found in [Séchaud (1999)]. However, the concept of the correction for any type of DM can be provided by the AO basic equation

$$\phi_{res} = \phi_{tur} - \phi_{corr} \tag{2.5}$$

$\phi_{res}(r)$ is the residual phase that we are looking to minimize and to make it zero as possible. Most DMs have actuators in an equally spaced rectangular grid, where their acting direction is parallel amongst them and perpendicular to the mirror membrane. By varying their length by a few microns, the membrane becomes locally deformed at the actuator position. The local deformation of the membrane is usually called the influence function produced by the actuator.

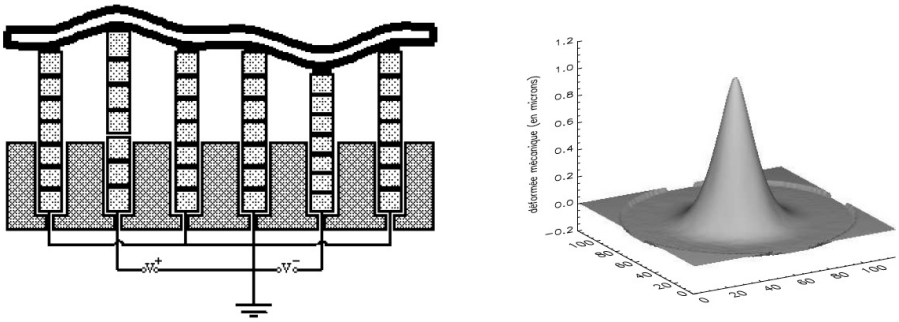


Figure 2.3: Right: Influence function sketch of a Stack Array Mirror (SAM) type mirror. Left: Concept of the SAM mirror type.

Spatially a DM is characterized by the number and position of the actuators, and also the shape that they give to the DM. In another word by the so-called influence functions F. The maximum spatial frequency that can be corrected by a DM may be approximated by $f_{max}^{DM} = 1/pitch$, where pitch is defined as the distance between two actuators. We check well the linearity of the spatial response of the mirror. In fact, the global DM deformation actuated by a vector voltage is generally well represented by the combination of the answer of each actuator. We define a linear relationship between applied voltages u and the deformation of the mirror, through a matrix F, called the influence matrix by

$$\phi_{corr} = Fu \tag{2.6}$$

2.4.3 Real Time Computer

The control in adaptive optics consist in controlling the DM given the measurements provided by the WFS to obtain the best possible correction of the phase. For this optimal correction, the temporal issues related to the control loop should be well managed, including the problems of system bandwidth, the loop stability and the optimal time of controls to be applied to the deformable mirror. In this dissertation we are not going to discuss the temporal control loop issues, many informations can be found in [Boyer et al. (1990), Ellerbroek et al. (1994)].
Now we are going to recall for the interaction matrix and the control matrix. As mentioned that the WFS and the DM are considered as linear systems. Assuming that we know the effect of applying the voltages on the DM to the WFS's slopes by the relation :

$$y = M_{inter} u \tag{2.7}$$

M_{inter} is the interaction matrix that converts the two dimensional array of measurements gradients into a corresponding array of drive signals for the deformable mirror, so that a vector of set voltages deformate the DM in order to correct the wave front distortion provided a set of turbulent measurements y^{tur} given by

$$u_{corr} = -M_c y^{tur} \tag{2.8}$$

M_c is the control matrix defined by the generalized inverse of the interaction matrix, rectangular in general, therefore non invertible. Thus M_c is evaluated as

$$M_c = (M_{inter}^T M_{inter})^{\dagger} M_{inter}^T \tag{2.9}$$

This method developed above is provided by the mean square methods which consists in minimizing the residual slopes measurements :

$$\epsilon(u) = \|y^{tur} - M_{inter} u\|^2 \tag{2.10}$$

In the next section we investigate the wave front reconstruction issues, which manifest in resolving an inverse problem so we present a theoretical analysis of reconstruction problem and the restoration of the phase. However, we don't consider the cloosed loop issues, and only consider a simple AO case in an open control loop. We will consider that the WFSs measures directly the phase perturbations introduced by the atmospheric turbulence and no temporal considerations wil be taken into account.

2.4.4 Wave front Reconstruction: An inverse problem

The wave front reconstruction problem or phase retrieval is fundamental to the more general problem of simultaneous wave front reconstruction and deconvolution. The problem of wave front reconstruction has been analysed as an inverse problem solved by the *maximum likelihood* methods [Fried (1977), Noll (1978), Gendron and Lena (1994)]. This chapter is devoted to a careful study of wave front reconstruction based on a theoretical analysis.

2.4.4.1 Direct Problem

Assuming that the WFS provides measurements of phase spatial derivatives linearly related to the wave front seen by the sensor :

$$S = D\phi + n \tag{2.11}$$

where ϕ is a vector of wave front values arrived at the WFS apertures, D is a linear operator providing the answer of the WFS on the incident phase, n accounts for the noise and model errors. This equation is valid as long as the wave front sensor is linear. The matrix D is dimension of $[N^2, 2 \times n_s]$, N is the number of degrees of freedom, n_s is the number of subaperture corresponding to the number of measurements in x.
The search for the inverse relationship leads to the corresponding inverse problem of wave front reconstruction or phase estimation. It consists in finding the best estimate $\hat{\phi}$ of ϕ given the set of measurement S, and assuming that the solution is a linear function of the data S, the restored wave front is given by

$$\hat{\phi}_{corr} = RS \tag{2.12}$$

where R is the restoration matrix. We are going to analyse in the next paragraph some different criterion to derive its expression.

2.4.4.2 Least Square Solution

In this section we review the Least Squares (LS) wave front reconstruction to solve this problem by minimizing the LS function:

$$\epsilon = ||S - D\hat{\phi}_{corr}||^2 \tag{2.13}$$

The goal of the LS wave front reconstruction is to determine an estimate $\hat{\phi}_{corr}$ of ϕ that yield to the best mean square fit to S, and this minimization problem can be solved by determining the value for which the partial derivatives $\partial||S - D\hat{\phi}_{corr}||^2/\partial S$ are identically zero. This is a standard linear LS problem. The minimum norm solution is given by the formula [Fried (1977), Hudgin (1977), Herrmann (1980)]

$$\hat{\phi}_{corr} = (D^T D)^{\dagger} D^T S \tag{2.14}$$

Here the superscript T means a matrix transpose, and superscript † means an inverse matrix. Matrix operations are very frequently encountered in adaptive optics. In almost all cases the matrix inversion presents problems because the matrix $D^T D$ is singular, which means that some parameters (or combinations of parameters) are not constrained by the data. In practice the matrix inversion is done by removing the undetermined (or poorly determined) parameters with the help of a singular value decomposition (SVD) algorithm.

2.4.4.3 Minimum Mean Square Error (MMSE / LMMSE)

The LS is not the optimal solution for the AO reconstruction problem. In order to improve the estimation using the least square and overcome the problems of inverting the matrices, we are going to estimate the correction phase that fit as best as possible to the true phase. That is to say that we want to estimate the correction phase that minimizes the mean square error, or the variance of the residual phase, that is to minimize the MMSE criteria

$$\epsilon = ||\hat{\phi}_{corr} - \phi||^2 \tag{2.15}$$

Minimum variance estimation is a Bayesian statistical approach in which a prior probability density is assumed on the phase. In our case, it can be accurately assumed that ϕ is a realization of a Gaussian random vector with mean 0 and known covariance matrix C_ϕ, and assuming that the noise vector n is Gaussian with mean 0 and covariance matrix C_n. The linear estimator that minimize the $MMSE$ is the optimal estimator [Van Trees Harry. L. (1968)] so-called $LMMSE$ (Linear Minimum Mean Square Error), given that the $LMMSE$ that minimize equation 2.15 can be written as

$$R_{MMSE} = (D^T C_n^{-1} D + C_\phi^{-1})^{-1} D^T C_n^{-1} \quad (2.16)$$
$$= C_\phi D^T (D C_\phi D^T + C_n^{-1})^{-1} \quad (2.17)$$

The phase covariance matrix can be described as the regularisation term while inverting the matrices in equation 2.14, avoiding the noise amplification by the eigenvalues. In the same conditions of Gaussian and linearity the $MMSE$ is equivalent to the another approach of type *maximum a propri* (MAP) described carefully in section 5.6.

2.4.5 Inverse problem: Estimation via the DM

In order to estimate the correction phase to be applied to the DM, we take as a direct model the operator connecting the measurements data to the mirror deformation, without expliciting the phase. This direct model is then expressed by

$$S = DFu + n \quad (2.18)$$

This linear model allows us to work with the measurements basis, known as the controllability and observabillity basis. Using the control matrix given by the equation 2.9 the voltages to be applied are then given by

$$u = M_{com} s \quad (2.19)$$
$$= M_{com} DFu + M_{com} n \quad (2.20)$$

where the last line represents the contribution of the propagated noise while inverting the matrix. The reconstruction methods presented above are based on a probabilitic approach and introduce a regularization term for resolving the inverse problem. They are all developed for the a simple AO open loop control case, that is to measure directly the atmospheric turbulence with the WFS, and then to correct with the DM controled given the WFSs measurements. This configuration is quickly limited by the WFS dynamics and faces its non-linearities. Furthermore, no information is reinjected on the system concerning the quality of the correction. In another word the correction is blind, unless we verify the final image.

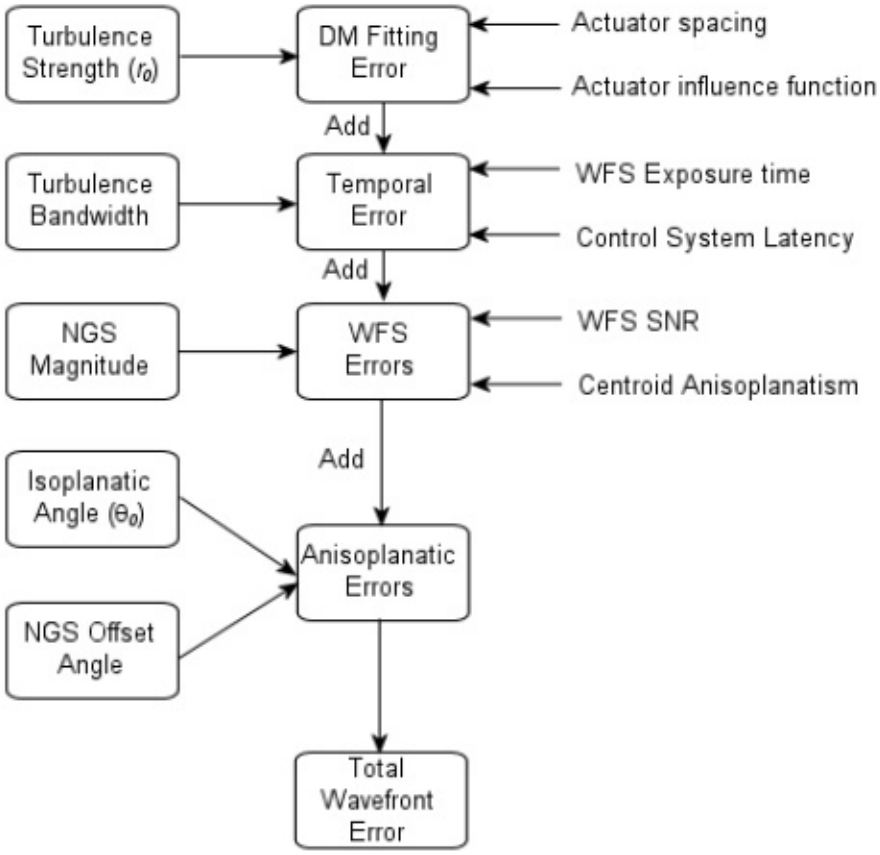


Figure 2.4: AO system error sources using an NGS as wave front reference. Diagram adapted from Hardy and Thompson (2000).

2.4.6 Error Sources and AO limitations

AO is an effective and powerful technique, nevertheless AO does not provide a perfect correction that remains only partial [Conan et al. (1992), Rousset et al. (1990),Rousset et al. (1992b),Roggemann (1991)]. In reality, many error sources limit the AO performances due to both the properties of the atmosphere (wind speed, the Fried parameter r_0) and the components that make up the AO system (number of actuators, number of subapertures, WFS camera performance, cte) as it is shown in figure 2.4.

We can identify the global system error, the magnitude of each error source shown in figure 2.4 must be combined. When errors in an adaptive system are calculated in terms of wave front variance σ^2_{res} of the residual phase given by equation 2.21, the system performance is described by the sum of the wave front variances due to each individual error source.

$$\sigma^2_{res} = \sigma^2_{scint} + \sigma^2_{aniso} + \sigma^2_{alias} + \sigma^2_{noise} + \sigma^2_{fit} + \sigma^2_{t} + \sigma^2_{calib} + \sigma^2_{aberr} + \sigma^2_{exo} \qquad (2.21)$$

Where σ^2_{scint}, σ^2_{aniso} , $\sigma^2_{alias}+\sigma^2_{noise}+\sigma^2_{fit}+\sigma^2_{t}$, $\sigma^2_{calib}+\sigma^2_{aberr}$ and σ^2_{exo} are the scintillation error, anisoplanatism error, errors due to the AO system, error due to the system calibration and the exogenous error. To study the performance and limitations of an AO system, we need to recall for the different types of errors that affect the performance of an AO system.

2.4.6.1 Errors due to the turbulence

2.4.6.1.1 Scintillation Error The scintillation is the cause of flickering stars observed with the naked eye and the effect of shadow bands observed in astronomy. This phenomena leads to a variation of the wave front amplitude in the telescope pupil plane . The direct consequence, and independent of OA, is a degradation of formed images on the imaging path. OA is unable to counteract these effects. Moreover, these amplitude variations disturb the measurement of the WFS. In fact, equation 2.11 is valid only because we assume homogeneity of the amplitude. Therefore, the scintillation phenomenon adds noise on the measurement of the Shack-Hartmann WFS. These effects of scintillation on the WFSs measurement have been studied by [Mahe (2000)] in the context of point objects and [Robert et al. (2006)] for the elongated object case. However, these effects of scintillation are generally neglected in astronomy, except in the case of observations of extended sources like the sun. They will also be neglected in the entire memory.

2.4.6.1.2 Anisoplanatism Error The wave front distortion measured using a reference at a given direction is only valid for an object in exactly the same direction since the turbulence is ditributed along the propagation path, so that the wave front error becomes decorrelated as the Field Of View (FOV) increase. This phenomena is called angular isoplanatism and is one of the major limitation of the AO system performance. It was describe in paragraph 1.2.2, and figure 1.4 demonstrated this effect. The anisoplanatism effect limits the FOV that can be corrected by the AO system. Once the angular offset between the science target and the bright NGS increases beyond the *isoplanatic angle* [equation 1.17], the degree of correction falls off rapidly. In order to overcome this limitation several solutions have been developed, either by creating artificial guide stars or by developing new concepts of AO. The combination of multiple reference sources located around the scientific field of interest allows the measurements of many different turbulent paths through the atmosphere.

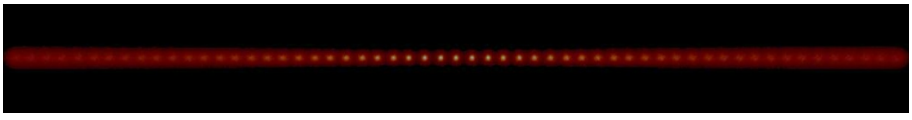


Figure 2.5: Limitation of the AO correction at the center of the FOV due to the anisoplanatism effect for different positions in an FOV of 60 arcsec.

2.4.6.2 Errors due to the AO system

2.4.6.2.1 Wave front measurement errors The aliasing error term is due to the limited spatial sampling of the wave front by the WFS. That causes high-order modes can alias into Low Order (LO) modes or high-frequency signals to be measured as low-frequency signals. The spatial aliasing error has been studied in the framework of AO [Herrmann (1981)]. Two aliasing types have been identified. The pure aliasing related to the sampling capabilities of the WFS (the number of subapertures) in line with the Shannon's sampling theorem and the undermodeling error.

This term of error can be reduced especially by spatial filtering of high frequencies before measurement by the WFS [Poyneer and Macintosh (2004), Fusco et al. (2005)]. The term σ^2_{alias} is associated to this error sources.
The second source of error is the WFS noise designed by σ^2_{noise} which is generally a superposition of photon noise and read-out noise presented in paragraph 2.4.1.2.

2.4.6.2.2 DM error source The DM will be able to correct only the phase fluctuations below its cutoff frequency $f_c = 1/(2d)$ where d is the actuator pitch (distance between the two adjacent actuators). As a consequence, the spectrum of spatial frequencies reproduced by the mirror is limited by the number of actuators in the pupil. The high spatial frequencies will not be corrected by the AO, these highest frequencies are transmitted to the AO system output and for the large error term, frequently referred to as *fitting* error designed by : $\sigma^2_{fitting}$.

2.4.6.2.3 Temporal errors Temporal errors are caused by the inability of AO systems to respond instantly to changes in the wave front, the delay between the measure of the wave front and the correction of the residual distortion results in a temporal error σ^2_t. This delay is due to the exposure time on the WFS, the integration time of the servo control loop, during which the WFS collects photons from the GSs, in addition to the read-out of the CCD detector and the processing of the wavefront data.

2.4.6.3 Error due to the system calibration

This error must be added to the errors presented above, it corresponds to a set of errors related to the interaction matrix, and implementation of the control law. These errors are difficult to quantify. They are noted by σ^2_{calib}. We don't consider this error in the rest of the memory. Moreover we should also add the errors due to the components that are after the beam splitter which are not common to both the control path and the imaging path. We can see from figure 2.1 that components in the optical path can be grouped into two categories, before and after the beam splitter. In fact, only the common path errors in these components are detected by the WFS and consequently are corrected by the feedback loop. However, optical aberration occuring in the non-common path, whether in the control loop or the imaging path, are not measured by the WFS and therefore not corrected by the AO loop. Thus, there is a degradation of the corrected wave front aberration

due to the installation itself. These aberrations, however, are static or very slowly varying (thermal effects). These errors denoted by σ^2_{aberr} could be estimated and corrected by a pre-compensation method as proposed in [Sauvage et al. (2007), Sauvage et al. (2005)].

2.4.6.4 Exogenous error

The exogenous error σ^2_{exo} combines all error sources from the environment that affect the AO system, and perturbate its operation. σ^2_{exo} covers the errors introduced by the propagated mechanical vibrations in the system affecting the wave front measurements or image acquisition. This terms becomes significant and affects the AO performance [Rousset et al. (2003)].

Chapter 3

New Concepts of AO

Contents

2.1 Synopsis 25
2.2 Adaptive Optics Background 26
2.3 Concepts of adaptive optics system 26
2.4 Adaptive Optics Sub-Systems 27
2.4.1 Wave front sensor: Shack-Hartmann 28
2.4.1.1 Description 28
2.4.1.2 Noise measurements 29
2.4.2 Deformable Mirrors 30
2.4.3 Real Time Computer 31
2.4.4 Wave front Reconstruction: An inverse problem 32
2.4.4.1 Direct Problem 32
2.4.4.2 Least Square Solution 32
2.4.4.3 Minimum Mean Square Error (MMSE / LMMSE) . . 33
2.4.5 Inverse problem: Estimation via the DM 34
2.4.6 Error Sources and AO limitations 35
2.4.6.1 Errors due to the turbulence 36
2.4.6.1.1 Scintillation Error 36
2.4.6.1.2 Anisoplanatism Error 36
2.4.6.2 Errors due to the AO system 37
2.4.6.2.1 Wave front measurement errors 37
2.4.6.2.2 DM error source 37
2.4.6.2.3 Temporal errors 37
2.4.6.3 Error due to the system calibration 37
2.4.6.4 Exogenous error 38

The main limitations of an AO system are the anisoplanatism and the sky coverage. To overcome these constraints and the growing needs of astronomers in observing more extended distant objects with a uniform AO correction, it is necessary to develop new AO concepts that compensate the atmospheric turbulence in its volume allowing to observe more objects in a wide field of view and also increasing the sky coverage.
Chapter 2 has presented the possibilities provided by the AO and also highlighted its inherent limitations. This chapter presents the new concepts of AO developed to face these limitations and the needs of astronomers. In section [3.1] we present the Ground Layer AO, and the Multi-Conjugate AO is presented in section [3.2]. In section [3.3] we present the Laser Tomography AO, Multi-Object AO is presented in section 3.4, both latter concepts were the case of study during the thesis.

3.1 Ground Layer Adaptive Optics (GLAO)

Ground Layer Adaptive Optics (GLAO) [Rigaut (2002)] is a new concept of wide FOV AO system, developed to compensate for the ground turbulent layer by using a single DM conjugated to a low altitude. The main objective is to ensure a partial correction but uniform in a large FOV of the order of 2 arcmin to 5 arcmin. GLAO is based on the idea that the lower layer of the atmosphere most often presents the larger amount of turbulence [section 1.1.2 and figure 1.2]. This system uses several wave front sensors coupled to different GS distributed in the FOV, as illustrated in figure 3.1. All the WFSs will measure the contribution of the ground turbulent layer, but also each WFS (coupled to a GS in direction α) will measure the contributions of the higher turbulent layers in the corresponding direction α. In principle, the contributions of the higher-altitude layers can be averaged out by simply averaging the wave fronts measured by all WFSs, as long as the number of WFSs is large [Nicolle et al. (2004)].
It is important to emphasize that, as opposed to the case of MCAO, the goal of GLAO is not to attain a near-diffraction-limited correction but to simply reduce and stabilize the seeing over a wide FoV. This principle of correction is particularly desired for studies requiring photometric measurements of objects of interest over a wide FOV. Furthermore this type of correction can be considered when using an adaptive secondary mirror to provide a first correction of turbulence directly within the telescope [Brusa and del Vecchio (1998)].

3.2 Multi-Conjugate Adaptive Optics (MCAO)

The MultiConjugate Adaptive Optics (MCAO) was the first AO concept studied with wide field of view. Proposed in the early 1975 by Dicke [Dicke (1975)], and developed by Beckers [**?**]. Several deformable mirrors conjugated at different altitudes are required to compensate for the phase perturbations introduced by different turbulent layers [Fusco et al. (1999a)]. MCAO compensation allows to increase the effective isoplanatic patch,

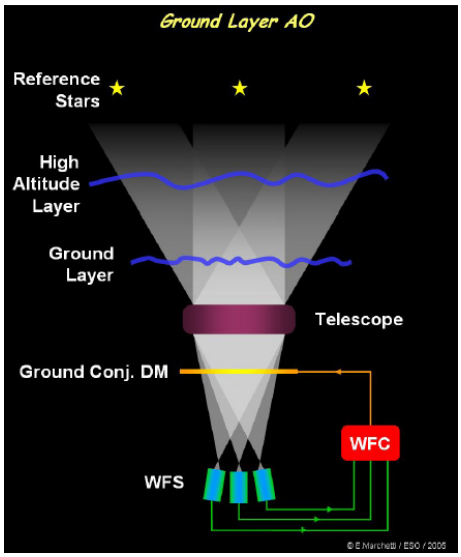


Figure 3.1: The principle of GLAO : in this figure the turbulence is analysed in three sky directions and one DM conjugated to the pupil plane, providing a lower correction than an MCAO system but in a wide FOV (Courtesy ESO)

and therefore, the corrected FOV. MCAO systems also requires to have several WFSs coupled to GSs in different directions α within the FOV of interest in order to probe a larger portion of the turbulent volume. Two wave front sensing strategies have been proposed so far for MCAO, known as Star-Oriented (presented in figure 3.2) and Layer-Oriented [Ragazzoni et al. (2002)]. In SO MCAO larger portion of the turbulent volume can be probed by means of several WFSs each of them coupled to a different GS in the FOV, so that each WFS measures the resultant phase in the telescope pupil integrated along a different line of sight. In LO MCAO there is a WFS detector conjugated to each of the turbulent layers of interest. The deformable mirrors are also conjugated to the same altitudes as the WFS detectors. All the signals are combined from all the stars in the FOV to command a DM associated to a given WFS.

3.3 Laser Tomography Adaptive Optics (LTAO)

A classical AO often suffers from the lack of suitable bright references within the isoplanatic patch from the object of interest. To improve this fundamental AO problem, one needs to resort to multiple Laser Guide Stars (LGS) in different directions. This so-called Laser Tomography Adaptive Optics (LTAO) presented in figure 3.3, probe the whole volume of turbulence above the telescope by using several LGS. Multi LGS are used to solve for the cone effect or the focal anisoplanatism. The correction is then applied over a small FOV by operating a single DM conjugated to the pupil of the telescope, as in classical AO. This system allows correction in a sky zone devoid of suitable bright reference. Therefore, the use of some LGSs allows a best measurement of the full volume of turbulence and realize a tomographic reconstruction unlimited by the cone effect presented in section

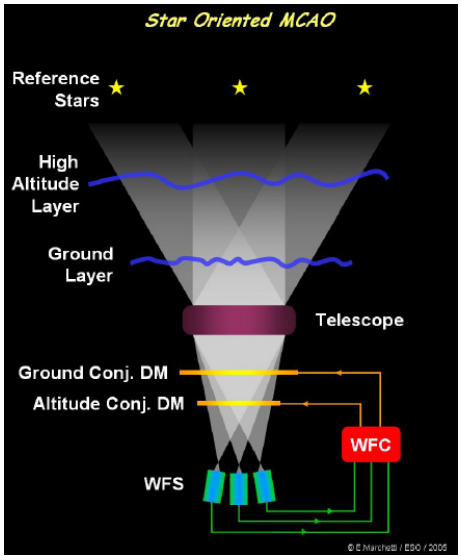


Figure 3.2: The principle of MCAO : in this figure three WFSS probe the volume of turbulence, WFC combines signals from all stars to command a given DM associated to a WFS (Courtesy ESO).

[7.11].

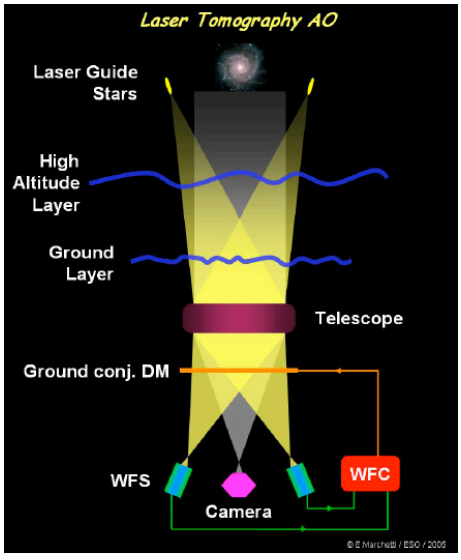


Figure 3.3: The principle of LTAO : in this figure the turbulence is analysed in two sky directions using Laser GS and one DM conjugated to the pupil plane, providing on-axis correction (Courtesy ESO)

3.4 Multi-Object Adaptive Optics (MOAO)

Multi-Object Adaptive Optics (MOAO) is an adaptive optics concept that would allow obtaining spectra of multiple objects at high spatial resolution in a field of view of 5 to 10 arcmin. MOAO has been proposed as an AO concept for current 8m telescope (FALCON) and for the European Extremely Large Telescopes (E-ELT) for the EAGLE instrument [Cuby et al. (2009)], as well as for the Thirty Meter Telescope (TMT) on the study of the Infrared Multiple Object Spectrograph (IRMOS) [Gavel et al. (2006), Eikenberry et al. (2006)] instrument to produce high resolution images of up to 20 objects on a 5 arcmin diameter field.

In a MOAO system, the deformable mirrors operate in an open loop with respect to the wave front sensors. MOAO is the only currently AO that relies upon open loop control. However, open control loop is perhaps the greatest risks to MOAO where the WFS sense the whole wave front error rather than a residual wave front error given by the DM. Open loop introduce requirements on an AO system: the WFS needs to have a high dynamic range, DM hysteresis and non-linearity need to be mitigated. Finally, alignment and calibration become more challenging.

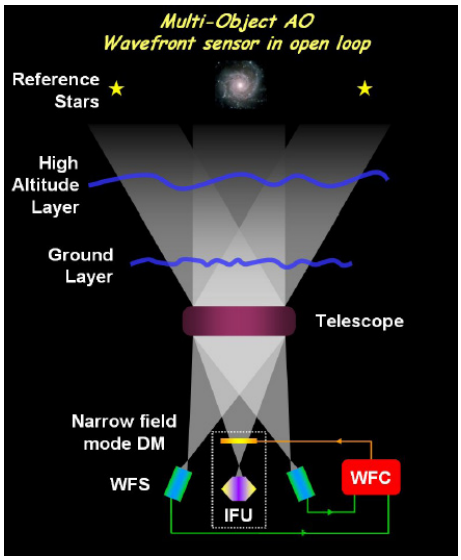


Figure 3.4: The principle of MOAO : in this figure two WFS probe the volume of turbulence, the correction is then provided by a DM in an open loop (Courtesy ESO).

MOAO can be performed by using a miniature AO tomography for each scientific object. It consists typically of three WFSs and a micro-mirror conjugated to the telescope pupil plane. Natural guide stars are used to measure the wave front distortion. A tomographic reconstruction is optimised in an interest sky direction. Such a system would effectively provide a significant performance estimation of the expected ensquared energy in different sky directions over a wide field.

Part II

Simulation Tools for AO systems

Chapter 4

Simulation of Adaptive Optics systems

Contents

3.1 Ground Layer Adaptive Optics (GLAO) 40

3.2 Multi-Conjugate Adaptive Optics (MCAO) 40

3.3 Laser Tomography Adaptive Optics (LTAO) 41

3.4 Multi-Object Adaptive Optics (MOAO) 43

The major part of our simulation studies is made with the E2E-S tool, an in-house IDL-based E2E modelling of the adaptive optics system including atmospheric effects, telescope parameters, AO sub-system, as well as science observations at large field of view. This code is based on a dedicated hardware, a cluster of PC and a dedicated library developed in C. It uses a number of custom functions relative to each model of the AO developed to answer our needs. They can be called all together in order to simulate the whole process of the experiment or to simulate specific parts of the AO system, to study or solve particular issues such as problems relative to LGS. This code takes advantage from the SOY library developped by Ralph Flicker that will be discussed in this chapter [part 5.3.1.2]. In this chapter we present [paragraph 4.2] different approaches for the AO simulation tools, we describe as well the advantages and the limitations of the different existing E2E and analytical models. In part [5], we present the E2E-S, our main simulation tools, and what we can achieve with.

4.1 Simulation needs

4.1.1 Why and how to simulate an AO system

A simulation is an emulation of reality using mathematical models. It is defined as the process of creating a model of a system in order to identify and understand the factors that control the system and/or to predict its future behavior.
More practically, the simulation of an AO system is a powerful and important tool since it allows the researchers to do instrumental studies without having the AO instrument itself, which may be prohibitively costly, time-consuming, or simply impractical to do. Moreover, it guides the AO designers to choose the most fundamental system parameters [Le Louarn (2010)] (such as the number of actuators, sub-apertures, RON, cte). The AO simulations can help the AO users in terms of investigating which AO system is more appropriate to their observation needs.
One more role of the simulation tools is to analyse and predict performance of different algorithms and components.
It is used for identifing bottlenecks in a process or in the AO system. It provides a safe, and relatively cheap (in term of both cost and time), testbed to evaluate the side effects, usually hardware related, like telescope vibrations, and to understand the behavior of the instrument in order to optimize the performance of the system.
AO simulation can be either analytical or numerical. The first one, is a fast estimation of the Point Spread Function (PSF) by deriving the Power Spectral Density (PSD) of the compensated phase from the PSD of the turbulent phase. This is based on transforming the AO linear model into the spacial frequency domain where the correlations and interactions between the most fundamental AO errors are well captured. A numerical simulation tools is based on a repeated random realizations of the atmospheric turbulence and the physical characteristics of each AO sub-system are modeled numerically and represented separately by a block. The simulation tools characteristics and existing codes will be the subject of section [4.2].

4.1.2 Simulation costs

Typically, a single ground layer simulation requires a desktop computer, while the simulation of a MCAO with multiple guide stars and Fresnel propagation requires a supercomputer. The AO systems for an ELT yield to a very high number of actuators (10^4,10^5) [Thiébaut and Tallon (2010)]. This is due to both increasing telescope diameters and new higher-resolution applications on existing systems. Multiprocessor parallelization is therefore required [Ahmadia and Ellerbroek (2003)] where the computation is spread on multiple processors, with the main problem that it can suffer from transferring data at sufficient rate between processors. On the other hand, current AO systems are using VMM reconstructors to convert gradient measurements into an estimated phase. Computing for such a method needs N^2 floating point operations and the cost of the matrix inversion required to prepare the estimator scales as $O(N^3)$. Furthermore, N scales as D^2, D is the telescope diameter. The result of the Vector Matrix Multiplication (VMM) scales

therefore as D^4 and the matrix inversion complexity $O(D^6)$. This complexity implies that certain acceleration of adaptive optics simulation is necessary to categorize the expected performances [Basden et al. (2005)].

4.2 Different approaches for the AO simulation tools

Flying over all existing AO tools we can loosely group them into two categories:

- Models that allow fast exploration of the system's parameters space. That defines an estimate of a given metric in terms of a given parameter using a single formula. Generally this type is called analytical or pseudo-analytical models.

- Detailed physical model, linked with the AO system model. Every single component of the system is represented and simulated as an independent block with an inputs/outputs independent module and connected with the other sub-systems modules. As an example the WFS, which is represented by a separate block from the other AO systems, receives a wave front as input and gives as output the slopes measurements. This type of methods are generally called E2E numerical.

The choice of one or the other type depend upon our need and what we want from the simulation. If we want a general view and understanding of the behavior and limits of the system we may use the analytical code. If we are looking for the physical properties of each element from the scientific object to be observed to the focal plane of the instrument we may use the E2E model. At below, we will give a brief description of the limitations and advantages for the different modeling efforts of AO systems. First of all we start by exploring the analytical models, the different pseudo-analytical models and then the E2E numerical tools.

4.2.1 Analytical Models: Error Budget

4.2.1.1 Description

Controlling the residual wave front deviations is extremely important for improving performance and system design in astronomical AO systems [van Dam et al. (2004),Evans et al. (2006)]. Understanding the contributions of each source of errors to the total amount of the residual rms error is critical to specifying the process tolerance and targeting areas for improving the AO system and inform the design of the future systems. As an example, the performance metric used for IRIS and WIRC instruments was the residual root mean square wave front error [Gilles et al. (2008)]. This process of decomposing the total rms to its component sources is known as error budget analysis. Characterization of the critical dimension AO error budget requires determination of the contribution of all the

AO subsystems. In general it must include an analysis of three different residual wfe: errors in measuring the phase, errors introduced by the DM, and errors caused by temporal variations. This residual WFE computation is based on analytical formulas.

4.2.1.2 Pros and Cons

As mentioned previously, an analytical tool is very fast to get an idea about system performance, especially because it is based on calculation of analytical formula that yield quickly without any iterations. So it allows quickly the AO designer to identify the problem or where the major error comes from and so enhancing the AO system performance. The error budget is an indispensable tool for assuring that project requirements can be and are being met. It presents a simplified allocation and rough performance estimating system, though not a replacement for more detailed systems performance modeling, since some errors cannot be calculated using analytical formulas. More appropriate codes are then required.
Moreover, the major limitation of an error budget tool is that the PSF is not given by an analytical formula, which entails a real problem given the different applications of an AO system where PSF is always required. Another limitation of such a simulation tool is that we loose all correlation between errors produced by the sub-systems.

4.2.2 Pseudo-Analytical Models

In this paragraph we describe the Pseudo-Analytical codes: a fast estimation of the PSF. The idea is to start from the Power Spectral Density (PSD) of the turbulent wave front and derive the power spectral density of the compensated phase by considering all the different errors that affect the AO system and from which the PSF can be easly estimated.

The main methodology of these codes is that they transform a linear system models of AO into the spatial frequency domain where the correlations and interactions between the most fundamental AO errors are well captured. So first of all, these codes assume that the optical system is linear and spacially shift invariant. Therefore, all the mathemathical operators describing wave front propagation, WFS and correction are linear and diagonal with respect to the spatial frequency domain and can be written frequency by frequency. For instance, the wave front reconstruction algorithm is expressed in terms of these operators and it follows that it can be derived and evaluated one Fourrier component at a time. Moreover, this regularized reconstruction algorithm calls for the phase and noise statistics which forces this last to be described linear and shift invariant spacial filters. For that, the phase disturbance and noise measurement statistics are zero-mean random variable with finite second order moments. More precisely, they can be characterized by their PSD.

4.2.2.1 Fourier method

1. Expression of the compensated phase:
   the corrected phase $\phi_c(r)$ is given by:

$$\phi_c(r) = \phi_{tur}(r) - \hat{\phi}(r) + n(r) \tag{4.1}$$

where $\phi_{tur}(r)$ is the turbulent phase, $\hat{\phi}(r)$ is the estimate of the phase obtained by the control system and n(r) is the vector measurement noise.
We assume that the DM is an ideal spatial filter with cutoff frequency $f_c = 1/(2d)$ where d is the actuator pitch. The DM corrects only the phase fluctuations below its cutoff frequency and that corresponds exactly to the sub-aperture size of the wave front sensor. The spatial frequencies above the WFS Nyquist frequency are not sensed and cannot be corrected. As a conclusion we can define the cutoff frequency of the AO system with $f_c = 1/(2d)$.

The turbulent phase $\phi_{tur}(r)$ can be decomposed into a low frequency component $\phi_{\|tur}(r)$, with spatial frequency content up to f_c, and a high frequency component $\phi_{\perp tur}(r)$, with spatial frequency content higher than f_c,

$$\phi_{tur}(r) = \phi_{\|tur}(r) + \phi_{\perp tur}(r) \tag{4.2}$$

The phase shaped by the DM is the result of the estimation of the turbulent phase in the low-frequency space $\hat{\phi}_{\|}(r)$ plus the projection of the estimation of the turbulent phase in the high frequency space onto the low frequency space (aliasing $\hat{\phi}_{\|\perp}(r)$), so that equation 4.1 becomes :

$$\phi_c(r) = [\phi_{\|tur}(r) - \hat{\phi}_{\|}(r)] + \phi_{\perp tur}(r) - \hat{\phi}_{\|\perp}(r) + n(r) \tag{4.3}$$

The first term in 4.3 reffers to the servo-lag error and it is related to the fact that the system can not respond instantaneously to a change in the incoming phase. The reading of the WFS, the reconstruction and the DM update needs some time, creating a time lag between phase measurement and correction. The second term in 4.3 reffers to the fitting error where the high uncorrected frequencies above f_c are transmitted to the output of the system. The third one is the aliasing error which results from the aliasing of the non-sensed high-frequencies in the low frequency domain of the WFS. The last error is the noise error due to the imperfections in the WFS.

2. Expression of the PSD of the compensated phase:
   Taking the Fourrier transform of 4.3 we obtain the PSD of the compensated phase as the sum of the PSD of the different errors shown above.

$$PSD_c = PSD_{fitting} + PSD_{aliasing} + PSD_{servo-lag} + PSD_{noise} \tag{4.4}$$

Each term of the PSD of the compensated phase can be derived and expressed analytically in the Fourrier domain. Once those terms are known and the Optical Transfer function (OTF) is deduced from the structure function given in equation 4.5, the PSD is found by a simple Fourrier transform [Veran et al. (1997)].

$$D_\phi(\rho) = 2 \int\int (1 - \cos(2\pi f \rho)) PSD_c d^2 f \tag{4.5}$$

where ρ is the distance between two points. Normaly the exact calculation of the OTF takes time since it requires for each focal plane angular frequency, a numerical integration over the position in the pupil. Fortunately, a modest approximation has been made in order to reduce the complexity of the calculation of the OTF by the use of the so-called satationary approximation. If the phase was stationnary in the pupil, then its structure function can be written as a function of the separation distance ρ, and consequently the OTF is calculated by a simple evaluation of an analytical expression.

4.2.2.2 Analytical Simulation tools

In this paragraph we care about different approaches developed to efficiently calculate the residual PSD after AO correction. We describe rapidly the basis of the different models, their advantages and limitations refering to papers or proceedings published by the authors.

4.2.2.2.1 PAOLA PAOLA: Performance of Adaptive Optics for Large Apertures [Jolissaint et al. (2006)], is a set of functions and procedures written in IDL for calculating the performance of an AO system. Developed at NRC-HIA, PAOLA is a first order analytical tools for modeling the long-exposure OTF of a telescope with AO. This OTF is multiplied then by the OTF of the telescope to obtain the overall OTF from which the AO long exposure PSF in any direction is easily derived.
PAOLA includes effects due to five main sources of residual phase error, where a residual PSD is written for each of these phase residual components: fitting error, WFS aliasing error, servo-lag, WFS noise and anisoplanatism error. Moreover, it includes different modes such as diffraction limited, seeing limited, classical AO correction, and Ground Layer AO. The WFS is a Shack-Hartmann sensor. The deformable mirror is supposed to be perfect: all aberrations at spatial frequencies below the DM cutoff frequency are filtered out. It

can be conjugated to any height in the atmosphere.
The advantage of such an analytical approach is the huge decrease in computation time (few minutes instead of hours comparing to the E2E codes). It allows the AO users to understand the different properties of the system by a first order analysis and without significant loss of accuracy. It has been developed as a tool for assessing AO performance on a given site and telescope, mainly to do science cases (but not limited to). The drawback is that it is difficult if not impossible to simulate the second order behavior of a real AO system (misalignments, imperfect reconstruction matrix, imperfect mirror influence functions,...). As a consequence, an E2E model is therefore needed to get more and fine details analysis of the system performance.

4.2.2.2.2 CIBOLA CIBOLA (Covariance-Including Basis Option for Linear Analysis), is a code written by Ellerbroek [Ellerbroek (2005)] in MATLAB for relatively rapid modeling of adaptive optics using linear systems methods in the spatial frequency domain. It is an extension of PAOLA for tomographic wave front reconstruction and MCAO. CIBOLA interprets turbulence statistics, performance metrics, wave front propagation, sensing and correction operators in the spatial frequency domain. It allows quick calculations of PSFs of many kinds of AO system (GLAO, MCAO, MOAO, ...). The package CIBOLA was used to verify the ATST HOAO system performance and TMT AO system NFIRAOS performance.
It includes integrated treatment of five fundamental AO error sources: DM fitting error, WFS spatial aliasing, additive WFS measurements noise, anisoplanatism and servo lag. The advantages of CIBOLA is that it captures many interactions and correlations between the error sources, it models the integrated effect of multi-guide-star AO and MCAO, minimum variance, least square, closed loop minimum-variance wave front reconstruction. CIBOLA is a powerful tool for a fast and accurate performance estimate during the initial stages of the developing system requirements. This efficiency takes advantages from neglecting the boundary conditions and aperture edge. Its main limitation is the inability to model LGS constraint. Therefore, LTAO cannot be modeled accurately, aperture edge cannot be evaluated or represented via shift-invariant spatial filters. It neglects AO implementation error sources such as DM hysteresis or DM/WFS mis-registration.

4.2.2.2.3 ONERA Fast-F New IDL-based analytic code for any Wide Field AO system (WFAO) developed by B. Neichel at ONERA [Neichel et al. (2008)], ONERA Fast-F derive the residual PSF for each frequency in the Fourier domain, given a matrix formalism of any WFAO system. The performance is computed for N_{dir} direction of interests by N_{DM} DM conjugated at different altitudes. It is a fast model to explore any AO system performance with cheap computation and allows a fine and accurate modeling tool for the ELT, able to provide the end product PSF. Such a tool includes treatments of many fundamental issues that comes with any WFAO systems such as tomography, number and position of DM, model/ statistical errors, unseen frequencies and projection errors.
Many studies have been done with ONERA Fast-F especially for tomographic systems. It was used to compare the MMSE approach with the Truncated LSE (TLSE), number of

guide stars required for a wide field of view. It derives rules for a robust control when system and atmospheric conditions are not perfectly known.
The main limitation of such a code is the fact that it is limited to NGS with open loop, no temporal behavior and aliasing effect are not considered.

4.2.2.2.4 Arizona Analytic Code Dedicated to GLAO systems, it is another analytic IDL-based tools developed by Tokovinin [Tokovinin (2004)] at the university of Arizona. It extends features of PAOLA for multiple laser guide stars. It includes treatments of DM fitting error, turbulence profile, cone effect, anisoplanatism error, multiple NGS/LGS, sensing global tilt from NGS. The GLAO PSF is calculated from the power spectrum of the residual phase given by the product of the atmospheric phase power spectrum and the Error Transfer Function (ETF). A Von Karman power spectrum is considered and computed at each turbulent layer. The turbulent volume beeing a combination of an arbitrary number of thin turbulent layers, the power spectrum of the residual phase is a sum of the power spectra of all layers.
The main limitation is that the temporal behavior of the AO system is ignored and the WFS measurements noise and aliasing too. It takes advantages of the approximation of neglecting the boundary conditions and the aperture-edge, and tip tilt signal can be derived from one or several guide stars.

4.2.3 End to End Models

In this part we describe E2E Monte Carlo simulations that rely on repeated random sampling . Such a simulation has a random statistics as input and produces many results as output. The main idea is that the physical characteristics of each components of the AO system are modeled numerically and represented separately by a block where the parameters of each sub-system has to be set. All the optical effects are well represented (magnitude, wavelenght, turbulence strength, cte). E2E simulations allow high fidelity modeling of system performance not addressed by traditional statistical metrics. Furthermore, numerical tools are necessary not only as end-to-end modeling but also to study the performance of sub-AO-systems and were primarily used to study physical effects not incorporated into analytic models and to verify the analytic model results for the baseline configurations.
In contrast to 4.2.2.2, long exposures are obtained after many iterations allowing the system to run many times so that the blocks that are randomly represented are statistically well computed. The whole process can be described by generating randomly a turbulent phase screen for each layer representing the atmosphere in question. Those layers are then projected to the wave front sensor module, which calculates a set of measurements in order to estimate the turbulent volume by using an appropriate reconstructor relative to each tool. The reconstructed phase is then projected to the mirror for correction, where many control laws can be used to achieve the AO system performance and accuracy.

4.2.3.1 E2E Simulation tools

Simulation is critically important for the development of any AO system since it enables to well understand the physical behavior of the system, allows the designers to specify the parameters of the AO components, helps to debug the system or even estimate the efficiency of a system on a given instrument. For all those reasons, many tools have been developed in order to provide definitive answers for all the AO needs which do not have the same level in accuracy in the results and so each tool has its own fidelity regarding its main objective. In this paragraph we describe some numerical tools, their advantages and limitations.

4.2.3.1.1 CAOS Originally developed in the framework of the European (FP4) TMR Network on Laser guide stars for 8-meter telescopes, CAOS (Code for Adaptive Optics Systems), IDL-based open source software, permits an end to end numerical modeling of any kind of AO systems. CAOS is now dedicated to optical astronomical studies covering a large scientific area through the Problem Solving Environment (PSE) [Carbillet et al. (2010)]. It is essentially composed of a global graphical programming interface (the CAOS Application Builder) which can load different software packages: MAOS that stands for Multiconjugate Adaptive Optics Simulations developed for multi-reference multireference AO studies purpose, PAOLAC which is a simple CAOS interface for the analytic IDL-code PAOLA, AIRY, image simulation and reconstruction with interferometer capabilities. The CAOS PSE is implemented in many studies such as LBT LINC-NIRVANA instrument, VLT SPHERE using the software package SPHERE [Carbillet et al. (2008)] and many others. The software package CAOS [Carbillet et al. (2005)], and the software pachage NAOS are a sets of modules (See figure 4.1) dedicated for an E2E simulation, it includes a complete atmosphere turbulence model, Shack-Harman and Pyramid as wave front sensors, laser guide stars in the sodium layers with a set of parameters for an upward and downward propagation, image processing module ,tomography and subsequent time filtering, coronagraphy.

The main advantages of CAOS is that it provides an E2E simulation for a classical adaptive optics system, allowing a fast study for all the modules. It permits for any AO user, beginner or professional, to well understand the parameters that manage all the AO modules from the generation of the turbulent volume to the projection and correction by the DM. In the other hand, such a simulator is limited with the number of degrees of freedom, while they increase dramatically with the new generation of telescopes [Chebbo et al. (2010)]. We will show finite studies of this limitation in chapter 5.

4.2.3.1.2 LAOS LAOS (Linear Adaptive Optics Simulator) is a set of MATLAB scripts written by Luc Gilles and Brent Ellerbroek for the Thirty Meter Telescope [Gilles and Ellerbroek (2005)]. It is a full AO Monte Carlo simulation tools used to determine the performance of an AO system from the estimation of the volume of the turbulence to the fitting step that determines the correction to apply in a way that is analogous to how it is corrected by the actual AO system. LAOS provides a linear representation of all AO

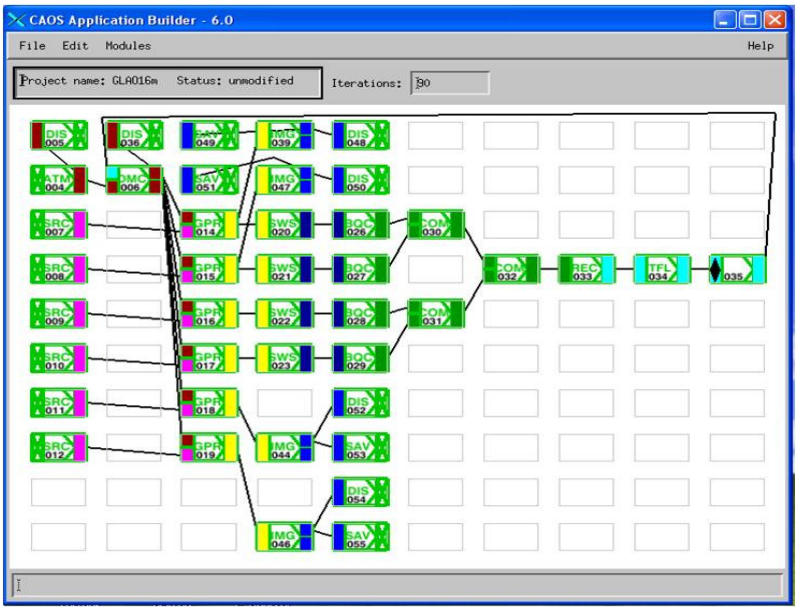


Figure 4.1: Modules of the software package CAOS and the spftware package MAOS used within the CAOS application in order to design a GLAO simulation.

components and phenomena. It uses minimum variance wave front reconstruction, implemented with sparse matrix techniques for efficiency.
The main advantages of LAOS is the possibility of wave front reconstruction from SH WFS measurements using either a Multigrid Preconditioned Conjugate Gradient (MG-PCG) algorithm, or a sparse Cholesky solver presented in section [5.6.2.4,5.6.2.3]. Moreover LAOS provides the capabilities of capturing the effects of wave optics LGS WFS, telescope aberrations and obscurations, DM-to- WFS pupil misregistration and distortion, anisoplanatism. The drawback is that LAOS is bounded by the computational speed and memory, especially when using large iterative loops.

4.2.3.1.3 OCTOPUS OCTOPUS (Optimized Cluster Tool for adaptive Optics Parallel Unlimited Simulations), it is an end-to-end Adaptive Optics simulator of the European Southern Observatory [Le Louarn et al. (2004)]. It is coded using parallelized C and an open source implementation of the MPI (Message Passing Interface), [Pacheco, 1997], running on a super computer. OCTOPUS is designed to simulate the 39 m E-ELT It simulates the atmosphere, the DM, the wave front sensor, the closed-loop control. The simulated sensor samples the incoming wave front and generates the centroids that are used by the code to reconstruct the wave front. The main advantages of OCTOPUS is the flexibility and computing power of C, but coding with MPI gives kind of complexity while coding any linear operation for an AO system. OCTOPUS simulates a perfect linear DM so that hysteresis and actuator imperfections are not modeled, it uses the standard method of wave front reconstruction VMM and the FRactal Iterative Method (FRIM) [Béchet et al. (2006)], limited to SCAO and GLAO.

4.2.3.1.4 ONERA Fast-E ONERA Fast-E IDL-based and developed at ONERA Paris, is a simulator tool for the BOA bench. It is a set of modules or functions representing each elements of an AO or MCAO system, that can then be assembled freely to simulate various systems (OA ... MCAO) with various nature or level of complexity. Those functions can be grouped as:

- Configuration System: includes functions and files to define the system and its constituents.
- Atmospheric turbulence model: can generate and manage atmospheric turbulence
- WFS simulator: simulates and characterizes a wave front sensor
- DM model: deformable mirror and tip/tilt simulator
- Control laws: permit the simulation and analysis of any control law.

4.2.4 Conclusion

Eight simulation tools, analytical and numerical, have been presented above. The analytical tools are based on calculations in Fourier space, usually of the residual PSF, however these tools are limited in their ability to handle LGS issues (cone effect, tip tilt indetermination). The numerical tools are used to simulate AO systems with a high level of accuracy. Advantages and limitations of each simulation code have been presented. A huge effort has gone in developping and optimizing these codes, especially developing new efficient reconstruction algorithms that deals with the high degrees of freedom coming with the ELT, and envolving new hardware like multi core PCs allowing like 48 GBs of RAM capable to deal with very large matrices and to speed the simulation.
At LAM Marseille and in collaboration with ONERA Paris, a new code E2E has been developed during my PhD, dedicated to the ELT and allowing efficient reconstruction based on a sparse techniques that handls rectangular matrices. E2E-S, discussed in the next chapter, call for a set of functions and routines developed in C and run on an octoprocessor machine with 48 GBs of RAM.

Chapter 5

Sparse End To End Simulator

Contents

4.1 Simulation needs 49

4.1.1 Why and how to simulate an AO system 49

4.1.2 Simulation costs 49

4.2 Different approaches for the AO simulation tools 50

4.2.1 Analytical Models: Error Budget 50

4.2.1.1 Description 50

4.2.1.2 Pros and Cons 51

4.2.2 Pseudo-Analytical Models 51

4.2.2.1 Fourier method 52

4.2.2.2 Analytical Simulation tools 53

4.2.2.2.1 PAOLA 53

4.2.2.2.2 CIBOLA 54

4.2.2.2.3 ONERA Fast-F 54

4.2.2.2.4 Arizona Analytic Code 55

4.2.3 End to End Models 55

4.2.3.1 E2E Simulation tools 56

4.2.3.1.1 CAOS 56

4.2.3.1.2 LAOS 56

4.2.3.1.3 OCTOPUS 57

4.2.3.1.4 ONERA Fast-E 58

4.2.4 Conclusion 58

5.1 Introduction

The current generation of telescopes has brought an incredible wealth of knowledge and scientific discoveries about our Universe. Imaging an extrasolar planet, tracking individual stars moving around the supermassive black hole at the centre of the Milky Way are VLTs signatures. These discoveries raise many new questions that future generations of Extremely Large Telescopes (ELTs) could answer. The advent of AO has breathed new life into the smaller telescopes and the VLTs in which it has succeed to correct for the deleterious effects of atmospheric turbulence.

This AO success has prompted planners of the next generation of telescopes, dubbed ELTs to plan for more AO developments. However, ELT needs in term of AO system naturally tends to very high number of actuators (10^4,10^5). This is due to both increasing telescope diameters and new higher-resolution applications on planned for AO systems. On the other hand, current AO systems are using VMM reconstructors to convert gradient measurements into an estimated phase. This computing method implies N^3 operations. The numerical simulation tools of ELT AO system need to deal with the very high number of actuators, and therefore become themselves a subject of study.

In this section we develop and describe an adaptive optics simulation platform developed during my thesis, which can be used to respond to various needs. The first is to simulate an AO system on the largest proposed ELT. This simulator is based on a sparse approach, initiated by R. Flicker. It's a sparse operations and routines that are used together for a specific purpose: efficient wave front reconstruction in adaptive optics simulations [Flicker (2009)].
The paragraph [5.2] presents the bottleneck: problems and needs while simulating an AO systems. We start by describing the sparse matrix technology in paragraph [5.3] (compilation cost, parallelization problem, gain in terms of memory...). A detailed breakdown of the SOY library is then presented in paragraph [5.3.1.2]. In paragraph [5.4] we present the global modular structure of the code. Each modul is described carefully in paragraph [5.5]. We present in paragraph [5.6] the wave front reconstruction strategy with high degrees with high degrees of freedom. In paragraph [5.7] we show some results for simulations and reconstructions done over a usual scientific calculator of 2.1GHZ.

5.2 High number of degrees of freedom : identifying the bottleneck

While the number of degrees of freedom dramatically increases, many solutions have been developed in order to deal with this numerical challenge. Running these simulations requires a large amount of memory and computer power in order to achieve the E2E simulation in a reasonable time. Running such a simulation on personnal computers takes many hours, or even days of computer times.
In this section we care about the running time considerations. Simulation of an AO system needs a fast computer machine and a fast algorithm simulation tool. Our first step consists

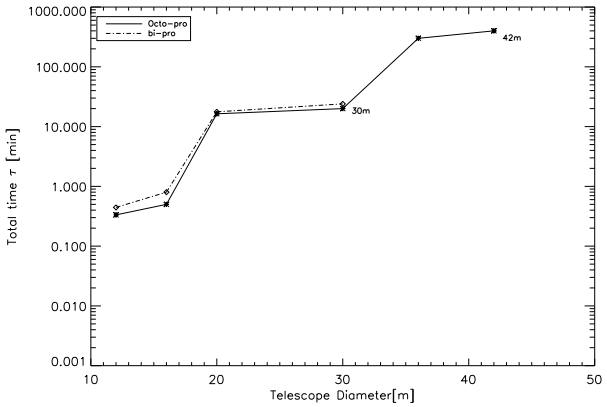


Figure 5.1: Computing CAOS time characterization running on both octo and bi-processor 2.1GHZ, 480 min are required for a telescope of 42m on the octo-processor machine

in validating the capabilities of our computers, octo- and bi-processor PCs, using the E2E CAOS tool. Then we show the increase of computation time when varying the number of iteration of the numerical simulation. We describe then the impact of the number of turbulent layers on the computational time.

1. As described in 4.1.2 the number of degrees of freedom scales linearly with the surface area of the telescope. As D grows large a problem will arise in simulating the system. The first step of our work consists in validating the computing capabilities for ELT simulations using two different computers that exist at LAM.

   - The ppfb machine with 2 processors having 24 Go of RANK.
   - The super computer Loom-vltsw. It has 48 GB RAM DUAL RANK DIMMS 667MHZ FB.

   First of all, using the standard biprocessor computer, we simulated classical adaptive optics with CAOS and we were capable to reach a telescope of 30 m of diameter. The first bottleneck is that the biprocessor computer was not able to make simulations for larger telescopes. Our second step consisted in simulating classical adaptive optics on an octoprocessor computer so that we reached a 42m telescope. In figure 5.4 we present the total time required to achieve an end to end simulation using both bi-processor and octo-processor for the different telescope diameter. For a 42m, 8 hours of simulation are required using the octo-processor machine.

2. As atmospheric turbulence is a random phenomenon, a large number of iterations has to be done to reach statistical behaviour. So it is necessary to examine the computational time in terms of iterations number. In figure 5.2 we show the total simulation time in terms of $N_{iteration}$. Five sky directions and three turbulent layers such that $h_{max} = 17km$ are simulated with the E2E-S described in paragraph 5.1.

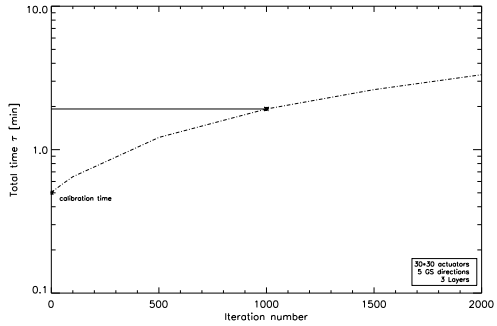


Figure 5.2: Total time in terms of number of iterations.

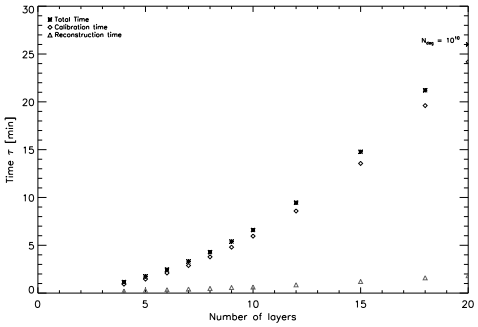


Figure 5.3: Variation of the simulation time with number of layers.

The phase map is represented by 116*116 pixels which correspond to the metapupil size, and 29*29 sub-apertures for each sky directions. It is shown that the simulation time increase in the average of 2.7 minutes for 2000 iterations, i.e. 0.18 sec /iter. where the calibration time T_{cal} is done once at the beginning. So for the parameters listed above we have:

$$T_{tot} = T_{cal} + 2000 * T_{rec} = 3.5min$$

where In figure 5.3 we plot time versus number of layers. We vary the number of layers in each simulation from 4 at different altitudes to 20 layers which correspond to 10^{10} degrees of freedom. The number of guide stars is fixed to 5 with 33*33 sub-apertures in each GS direction and the h_{max} at 26 Km. The phase map is represented by 132*132 pixels.
For the 20 layers case the calibration time is about 26 min which correspond to the time spent to build all sparse matrices (projector, WFS and the control matrices, etc), and the total reconstruction time for 100 iterations is 2 minutes (1.2 sec per iteration).

As a conclusion, the computational time increases with the number of degrees of freedom. Simulating AO for the ELT with the existed tools makes our work more difficult even on the octo-processor machine at LAM. An E2E EAGLE (**E**lt **A**daptive optics for **G**a**l**axy **E**volution) simulations (a flagship instrument of the future E-ELT) has to be run about 3500 times to well simulate 9 turbulent layers. Such an instrument will face computational bottlenecks in dealing with very large matrices using ordinary computers. For those reasons it is obvious to look for smarter technics and algorithms for helping us both simulate in a reasonable time an AO system and bring down the computational load.

5.3 Sparse Matrix Technology Primer

Starting from an informal working definition of the sparse matrix: *'Any matrix with enough zeros that it pays to take advantage of them'*, given by J. H. Wilkinson [Gilbert

et al. (1992)] (Wilkinson seems to have never published this definition in writing). In another word, a matrix can be termed sparse whenever special techniques can be used to take advantage of the large number of zero elements and their locations to reduce both the storage and work required in solving a linear system. There is a benefit to take advantage of the fact that the interaction matrix and the covariance matrix are mostly filled with zero elements. In this paragraph we give a brief summary about the different sparse matrix storage format and particulary the row-wise schemes which is the storage format used in the SOY library.

5.3.1 Sparse matrix storage format

As there is no reason to store and operate on matrices largely filled with zeros, it is often useful to modify the existing algorithms to take advantage from the sparse structure of the matrix, as sparse matrices can be easily compressed, yielding significant savings in memory usage. In figure 5.5 we show the storage gain on the computer while building a full matrix of a given dimension using the row-wise sparse representation. We can note that the computer memory saved is about 4500 GB in sparse format, making possible the ELT simulations where the dimensions of the matrices grow dramatically. There are a number of common storage formats used for sparse matrices, like the sparse matrix format Coordinate Storage (COO), Compressed Sparse Column (CSC), Compressed Sparse Row (CSR), and Block Sparse Row (BSR) compressed. Most of them employ the same basic technique. They store all non-zero elements of the matrix into a linear array and provide auxiliary arrays to describe the locations of the non-zero elements in the original matrix.

5.3.1.1 The sparse row-wise format

The sparse row-wise format [Chang, 1969; 29/ Curtis and Reid, 1971b; 46 /Gustavson, 1972; 112], is one of the most commonly used storage schemes for sparse matrices. The scheme has minimal storage requirements for sparse VMM $A.c$ of a sparse matrix A by a full column c from the right, as well as the row-wise representation of the structure of $(A.c)^T$ which is identical to a column-wise representation of the structure of $A.c$. It can be obtained by transposition of the row-wise structure of $A.c$ so that the transpose of the matrix is multiplied by a full row-vector from the left rA^T . In figure 5.4 we show the VMM computational time for both row-wise sparse format matrix and a full matrix format by a linear vector. For the same matrix dimension represented in either sparse or full format we show in figure 5.5 the gain in terms of the allocated memory on our computer machine.

So that for the same matrix dimensions computer memory saved about 4500 GB while building the matrix using the row-wize format. Among the sparse row-wise representation of a matrix A we can identify the **R**epresentation **C**omplete and **O**rdered (RCO) and the **R**epresentation **C**omplete and **U**nordered (RCU) representation compatible with the nonsymmetric matrix. Complete is said because the entire matrix A is represented and ordered because the elements of each row are stored in the ascending order of their column indices. If the matrix is symetric, computer memory can be saved by storing only the nonzero entries in each row on and above the main diagonal RUO and RUU. In this

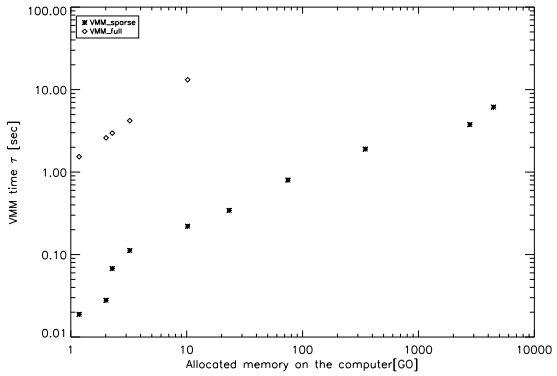


Figure 5.4: Vector Matrix Multiplication (VMM) computing time

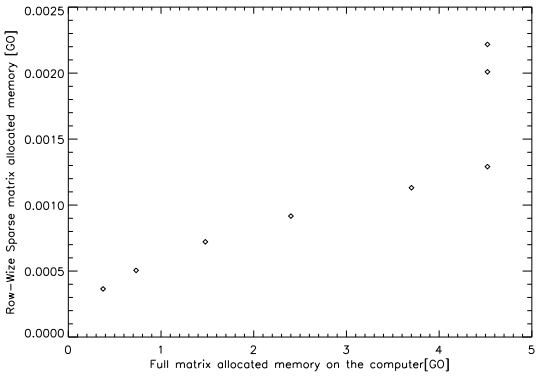


Figure 5.5: Ratio of allocated memory using sparse and full matrices

dissertation we care about the ordered matrix. The sparse row-wise format is presented in appendix A

5.3.1.2 Main Features

Sparse Operations with Yorick/IDL originates from a collection of IDL/C routines that are used together for a specific purpose: efficient wave front reconstruction in adaptive optics simulations [Flicker et al. 2000]. The SOY library employs the format Row-wise Representation Complete and Ordered described above for an arbitrary real matrix - designated RR(C)O and its upper triangular version RR(U)O for a symmetric real matrix. This format is optimized for fast VMM and using such a library allows us to handle memory by indicating the maximum number of rows to accommodate and the maximum number of non-zero elements to store. Moreover, the SOY library allows single and double precision in manipulating sparse matrix and offers some basic matrix algebra as addition, multiplication transpose and other.
IDL supports the sparse row wize representation but unfortunately is limited to square matrices. Some studies and developpement were done by R. Flicker to work around and to handle any non-square matrices but with a penalty paid in storage and CPU cycles. Moreover, the Cholesky decomposition presented in paragraph [5.6.2.3] in IDL does not manage the sparse matrices, while such a decomposition is very important as the conjugate gradient in solving the wave front reconstruction problem. The SOY library presented in this section provides an efficient solution for resolving the non-square matrix generated by a model of the AO system in sparse format, and presents an approach to handle in IDL the Cholesky decomposition with sparse matrices.
In appendix [B] we highlight on the different routines and functions of the SOY library developed in IDL.

5.3.2 Conclusion

In this paragraph we presented the E2E-S library, so-called SOY, based on the Row-wise Representation Complete and Ordered designated RR(C)O and its upper triangular version RR(U)O for a symmetric real matrix. The main advantages of the SOY library is that it supports handling of non-square matrices and the Cholesky decomposition with IDL using the sparse approach. It offers basic sparse matrix algebra and manipulating in single and double precision. We listed the different routines and functions and how to build a sparse matrix in an RCO or/and RUO structure.
The specific purpose of the SOY library is to efficiently perform a wave front reconstruction in adaptive optics simulations. In fact, the main benefit of this library shines in the wavefront reconstruction, where there is no need to explicit calculation of the reconstructor, but to take advantage of the fact that the covariance and interaction matrices are very sparse since there most entries are zeros. Given this significant insuffisance the reconstructor must be built using the row-wise scheme for an efficient computation and storage.
Based on the SOY library and given all the relevant tools, we are going to present the E2E-S developped at LAM Marseille and ONERA Paris, for a specific purpose: *Refined AO simulations* dedicated to the extremely large telescopes.

5.4 E2E-S Global Structure

The E2E-S simulation tool is developed in order to provide a detailed analysis of physical behaviour of an AO system. E2E-S is a concatenation of different blocks representing each sub-AO-system. This simulator is used to quantify the global system performance, and offers a detailed physical study of each sub-AO-system.
Based on SOY library developed above, E2E-S is a set of sparse IDL functions and routines developed at LAM in collaboration with the ONERA team Paris, to simulate the different AO components. These separated functions can be assembled freely to simulate various systems (OA ... MOAO) with various level of complexity and degrees of freedom taking advantages of the sparse row wise format.
E2E-S is developed in order to implement and solve issues generated by the ELT (Cone effect, tip tilt indetermination, fusion data LGS/NGS).The final objective of such a tool is to be able to simulate an ELT instrument. We will apply it to the EAGLE complete case with 9 turbulent layers and 11 analysis directions in 7.5 arcmin. This simulation is developed in chapter 9.

5.4.1 Assumptions of the E2E-s simulation code

Some assumptions are made in this simulator. Thus, the simulation is conducted in discrete time on occurrences of the discrete phase. It therefore neglects the phenomena of integration signal. Another modest approximation is made to the covariance matrix of

DM actuator commands, in order to apply the sparse techniques in the wave front reconstructor with negligible loss of performance. Such an approximation will be described in section 5.6. In addition the elongation of the spot of laser guide stars is neglected.

The whole finalist functions have been developed during this thesis, starting from a base developed by J.-F. Sauvage at ONERA Paris. The work done consists in developing a generator of turbulent wave front, a geometric sparse modelling of the WFS, a mirror sparse modelling. The LGS implementations and the tip/tilt indetermination and the fusion data for LGS/NGS. Those functions can be grouped into five blocks:

- System of configurations: includes functions and files to define the system and its components.
- Turbulent generator: can generate the atmospheric turbulence
- WFS model: simulates a Shack-Hartman wave front sensor with a real physical approach.
- DM model: simulates the influence matrix of the Deformable Mirror. This matrix is the concatenation of the influence functions, which are the phase deformations corresponding to actuator deformation.
- Tomographic recontructor: generate a linear projector for natural guide stars measurements and a hyperbola projector for laser guide stars measurements.

5.5 Description of the different modules

In this section we describe more precisely the content of each of these five functional groups, highlighting the underlying models or assumptions.

5.5.1 Configuration System

The configuration system is an interface that compile all the different functions and the SOY library. It combines all the parameters needed to simulate an AO system:

- The observational parameters such as: seeing, external and internal scales, turbulence profile, number of layers, wind velocity...
- System parameters: telescope characteristics (pupil diameter, FOV, number of layers and sky directions, seeing...)
- Correction system parameters: DM characteristics (number of actuators, influence functions,mechanical coupling...)

- Measurements parameters : number and position of LGS/NGS in the field of view, number of sub-apertures, measurement wavelength, etc.

The calibration of the AO system is also simulated by calling the function calibration_AO.pro that calculate all the different matrices needed for the complete simulation. Finaly, the analysis code in *performance.pro*, where we analyze the residual PSF, Strehl ratio and the ensquared energy.

5.5.2 Atmospheric Turbulence

The turbulent volume is discretised in altitude, in N layers. Each layer is discretised in X and Y in NP pixels. The phenomenon of propagation through the atmosphere is simulated by simply cutting turbulence in the directions of interest, assuming that the amplitude fluctuations of the electromagnetic field are negligible within the pupil, as if the phase turbulent perturbation were occurring so close to the pupil that the amplitude change due to Fresnel propagation is neglected. This is so-called *near-field approximation*.

5.5.2.1 Turbulence Generator

Multi-turbulent-layers is generated using in the form of pixelised phase screens following the Kolmogorov or Von Karman turbulent type see figure 5.6 .

The generation of a Kolmogorov turbulent phase is done by respecting the following steps:

- simulation of a white noise,
- computation of noise Fourier transform,
- modulation with the desired spatial spectrum density,
- inverse Fourier transform,
- taking real part to get rid of the numerical effects.

The turbulent screens are simulated on an array larger than necessary. This allows one to ensure that the large scale effect is correctly accounted for. The size of the screens is determined by the simulations conditions (number of iterations, wind speed, and sampling frequency, field of view, etc.). In addition the outer scale of the turbulence L_0 is well represented in the generation of the screens, the screens are relatively large to reduce this effect. These screens are then scaled in amplitude according to the characteristics of turbulence (parameter r_0) and weighted in the case of a multi-layer by the turbulence profile C_n^2.

The temporal evolution of the turbulence is simply obtained by adding a uniform translation of each layer according to the wind speed and direction for the considered layer. It is based on an assumption of Taylor-type. For each iteration of the loop, the extraction and summation is then carried out to obtain the contribution of the phase in the pupil plane from each layer and from each direction of interest. This operation is realized by a linear/hyperbolic sparse projector. Linear is fixed for the NGS case and hyperbolic projector for the LGS case see section (7.3.2). This projector provides the contribution in the pupil plane coming from the turbulent volume, so we obtain an equivalent of the atmospheric propagation taking into consideration the geometric approximation which assumes small perturbations and neglects the Fresnel propagation.

$$DSP = [0.033(f^2 \times (\frac{2\Pi}{L_0})^2)^{\frac{-11}{3}} \times exp - (\frac{2\pi f \times l_0}{5.91})^2 \times (\frac{r_0}{1.674}\cos\gamma)^{\frac{-5}{3}}] \times (2\pi)^3 \quad (5.1)$$

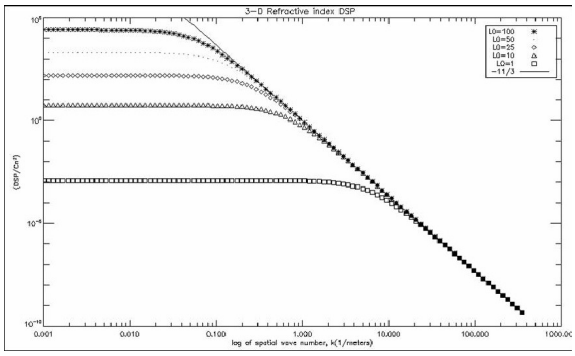


Figure 5.6: Variation of the DSP of the turbulent phase for different outer scale

5.5.3 Wave Front Sensor Sparse-Model

We propose in this section a linear modelisation of the Shack Hartmann WFS, compatible with sparse format. The SH provides a linear zonal measurement of the wave front. Below we present the Fried geometry model and we propose a discrete approach to provide a simple but realistic model of the measurement of a Shack-Hartmann, taking as input a phase map, so-called zonal approach producing as output a set of measure of slopes in x and y.

5.5.3.1 Fried's Geometry

The Fried geometry is frequently used, however, in modeling the behavior of SH sensors. It models the gradients that are generated by SH sensors, which are centered between phase points. This allows one sensor to provide both x- and y-gradient measurements.

See figure 5.7 for an illustration of the Fried geometry, the gradient is modeled as the average of the two nearest first differences.

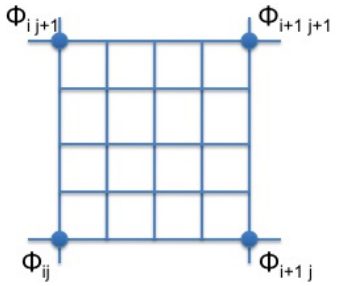


Figure 5.7: Illustration of the Fried geometry

A model of the wave front sensor hat allows one to link the measurement S to the incoming phase ϕ thanks to the following relation:

$$S = \begin{bmatrix} S_x \\ S_y \end{bmatrix} = D\Phi \tag{5.2}$$

The interaction matrix D concatenates the answer of each subaperture of the WFS to the insident phase. In this section and for the sake of simplicity we don't consider the partly illuminated subaperture, all the subaperture are fully illuminated and treated identically. In the Fried geometry the gradient is modelised by the difference between the average of the two phases at the corners of the subaperture:

$$\begin{aligned} S_{ij}^{x} &= [(\phi_{i+1j+1} + \phi_{i+1j}) - (\phi_{ij} + \phi_{ij+1})]/2d \\ S_{ij}^{y} &= [(\phi_{i+1j+1} + \phi_{ij+1}) - (\phi_{ij} + \phi_{i+1j})]/2d \end{aligned} \tag{5.3}$$

Where the ϕ_{ij} are the phase values at the four corners of the subaperture. The matrix D contains four elements per row refering to the phases at the four corners of the subaperture, so the elements of D are either $\pm(2d)^{-1}$ or 0 entailing that D is very sparse see equation 5.4 which correspond to the x- gradient measurements.

$$\left\{ \begin{array}{cccccccccccccccc} -1 & 1 & & & & & -1 & 1 & & & & & & & & \\ & & -1 & 1 & & & & & -1 & 1 & & & & & & \\ & & & & -1 & 1 & & & & & -1 & 1 & & & & \\ & & & & & & & & & & & & -1 & 1 & & \\ & & & & & & & & & & & & & & -1 & 1 \end{array} \right\} \tag{5.4}$$

5.5.3.1.1 Power noise and SNR In this paragraph we investigate the power spectral density of the wave front estimated from the wave front slopes measurements, and the Signal to Noise Ratio (SNR).
As given by [Noll (1978)], the PSD of the residual wave front is given by:

$$PSD_{\phi} = PSD_S / 2\pi^2 f^2 \tag{5.5}$$

Where PSD_s is the PSD of the slopes measured by the SH. Equation 5.5 means that if a white noise is propagated on the slopes measurements the estimation multiply the PSD_s by f^{-2} to obtain a phase spectrum in f^{-2}. That is to say, the lower spatial frequency implies larger error on the estimated phase. We show in figure 5.8 the PSD of the residual wave front using the output measurements given by a SH. It is important to note that the PSD is independent of the number of subaperture.

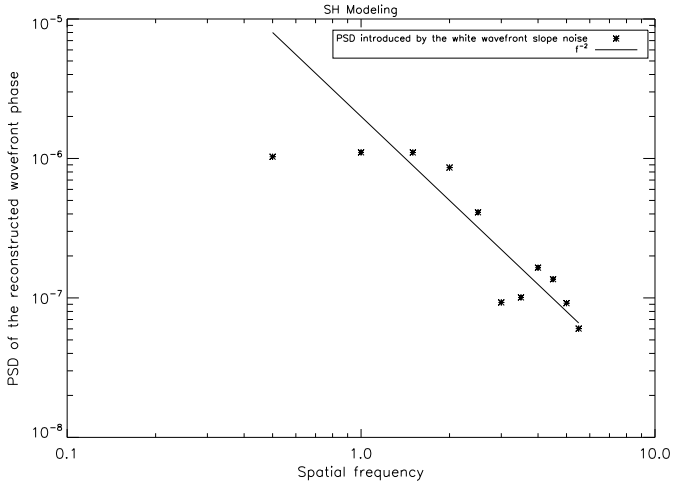


Figure 5.8: Wave front errors resulting from the white wave front slope noise

Signal to Noise Ratio The signal to noise ratio is given by the ratio between the variance of the arrival angle σ^2_{aa} on the Shack-Hartmann subapertures and the noise variance σ^2_b.

$$RSB = \frac{\sigma^2_{aa}}{\sigma^2_b}$$

Once we calculate the measurements S using the Fried's model the σ^2_{aa} is given by:

$$\sigma^2_{aa} = \langle S^2 \rangle$$

5.5.3.2 Realistic Geometry Model of Shack- Hartman WFS

In this paragraph we present a realistic approach of a real SH WFS, it is a generalised case of the Fried geometry presented above.
It is based on the interaction between the sub-aperture matrix and an incident wave front. This is actually a discrete approximation of equations 2.1, connecting the derivative of the phase and the measured slopes in each sub-aperture. These equations can be simplified as:

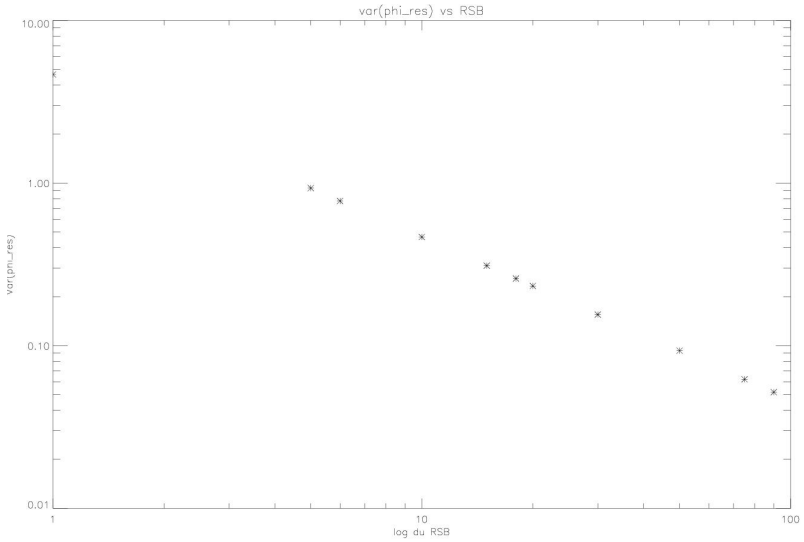


Figure 5.9: variation of the residual wave front error in terms of SNR

$$S_x = \frac{\lambda}{2\pi d_x} < \phi_{xmax} - \phi_{xmin} > \tag{5.6}$$

Where d_x represent the size of the subaperture along x, ϕ_{xmax} and ϕ_{xmin} are the pixelised phase, < > designating the spatial average on the pixels.
The measurements are obtained by averaging over each sub-aperture the differences of the phase located on the edge to the other of the subaperture. In addition the partly illuminated subapertures are managed in this case by modifying equation 5.6 taking into account the surface of the illuminating part of the subaperture. This model requires knowlegde of the WFS structure such as the number of subapertures, number of pixels per subaperture and identifying the illuminated and partly illuminated subapertures.

This discrete approach is used to provide a simple but realistic model of the measurement of a SH, taking as input a grid of phase (zonal approach) and outputting a set of measurements $\begin{bmatrix} S_x \\ S_y \end{bmatrix}$.

5.5.3.2.1 WFS RCO matrix Taking advantages of the SOY library the WFS matrix Ds is built using the RCO row wise format (see figure 5.10). Initialized to zero as shown in the table 5.1, then we concatenate the (2.*Ns_valide2) rows representing the number of activated subaperture for x- and y- gradient measurements. In addition, the partly illuminated matrix are thus treated taking into account the illuminated part of the subaperture.

```
Ds = {rco}
Ds.r = 2.*Ns_valide2
Ds.c = dim_alt_px2
Ds.n = 4.* nb_pix*Ns_valide2
Ds.ix = ptr_new([0,make_array(Ds.r,
/long)])
Ds.jx = ptr_new(lonarr(Ds.n + band-
width))
Ds.xn = ptr_new(make_array(Ds.n+
bandwidth, /float))
Ds.r = 0L
Ds.c = 0L
Ds.n = 0L
```

Table 5.1: RCO format of the WFS matrix initialized to zero colomns, rows and entries, where Ns_valide2 is the total number of valid subaperture, dim_alt_px2 is the square of the phase grid size.

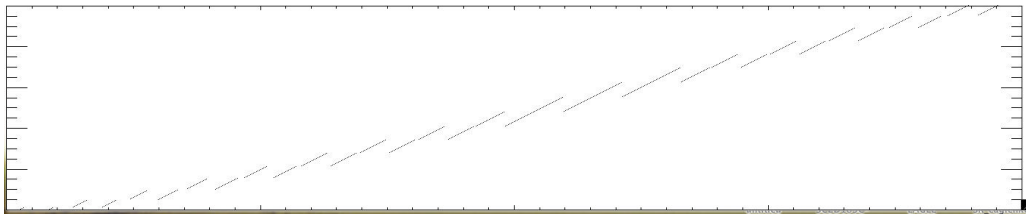


Figure 5.10: Ds is calculated using the realistic WFS geometry model. Zonal representation for a system of 20 *20 subapertures, where 308 are fully or partly illuminated in the pupil

5.5.4 Deformable Mirror Model

The mirrors are considered as linear components with instantaneous response. They are completely characterized by their Influence Functions (IF). That is to say, It is represented by the collection of the phase deformations of each actuator. Each IF corresponding to each activated actuator is presented in the form of a screen phase of n*n pixels.
The study presented in this section is based on a modest approximation of the IFs by the Gaussian function.
In order to verify the DM model and to study the physical aspect of the DM we based first of all on an analytical studies to determine the number of actuators of the DM that minimizes the fitting error after correction by the DM using the Fourier formalism. These results are thus related to the turbulence to be corrected. Then we propose a comparison with a numerical simulation using the E2E-s.
In this section we present first of all the RCO format of the model, then we minimize the number of actuators using the analytical formula and we compare it with the numerical simulation. Then we show the mechanical coupling that minimises the error of the residual phase.

5.5.4.1 DM sparse Model

The IFs are approximated by the double Gaussian model. This model is identical for all the actuators. For the sake of the sparsness of the IFs matrix it is reasonable to make the following assumptions: the IFs are localized, extending no further than the immediate nearest neighboor. We define each IF on a certain number of actuators, this number is described as *Nacinf*: number of influence actuators, beyond *Nacinf* the IF is set to zero. It is possible to adjust the desired mechanical coupling defined as the value of the IF at the nearest neighbour location relative to its maximum value. The dimensions of the DM are also needed such as the number of actuators and number of pixels per actuators.
The RCO influence matrix F is an assemble of vectors defined on a pixelised base with n*n pixels, representing each valid actuators *Nact_valid*. Any of these vectors refers to the phase shaped by the mirror once the actuator in question is activated. The final RCO matrix is [n*n,Nact_valid]. The figure 5.11 represents the double Gaussian IFs profile for a DM of 8*8 actuators with a 45% of mechanical coupling and *Nacinf*= 4. The shown artefact explains the discontinuity on the mirror phase as depicted in figure 5.12 and affects also the high frequencies i.e the fitting error. So it is important to minimize this number without affecting the sparsness of the matrix and we found *Nacinf* = 6, which means that the IFs is set to zero beyond the third actuator as it is shown in figure 5.13 this leap disappeared and the mirror well produces the tip mode.

5.5.4.1.1 Mechanical Coupling Before we start characterizing the DM we study the influence of the mechanical coupling on the residual error given by the mirror in order to minimize the error produced by the model. We build an RCO IFs matrix with n_{act} = 14, *Nacinf* = 6 and 6 pixels per subaperture. The simulation is done on 100 iterations.

In figure 5.15 we present the simulation results, The optimal coupling for representing the turbulence deformation is around 35%.

5.5.4.2 Number of actuators in terms of the fitting error

The first block of the E2E-S code is stochastic by nature, it is then important before doing any numerical or analytical studies, to understand the behavior of the turbulence statistics so that we can be sure that it can be totally represented. The analysis of the turbulent phase gives a primary idea on the performance of the mirror. The stationnarity of the phase in the pupil depends on the value of the external scale L_0 [Heidbreder(1967), Wang et Markey(1978), Conan(1994)], furthermore the variance of the phase on the edges is always greater than on the center of the pupil of the telescope [Costille (2009)]. In our case the tip-tilt are not excluded from the phase implying that the value of the outer scale

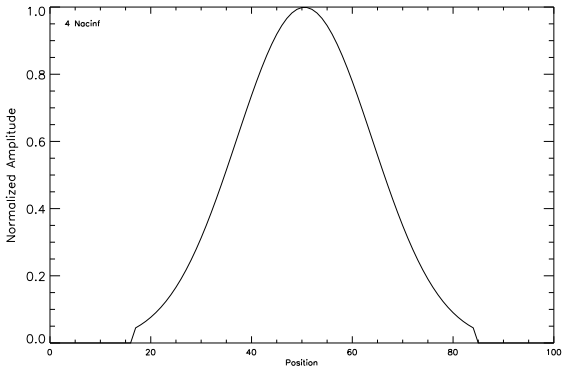


Figure 5.11: The IFs is set to zero beyond the second actuator from the center

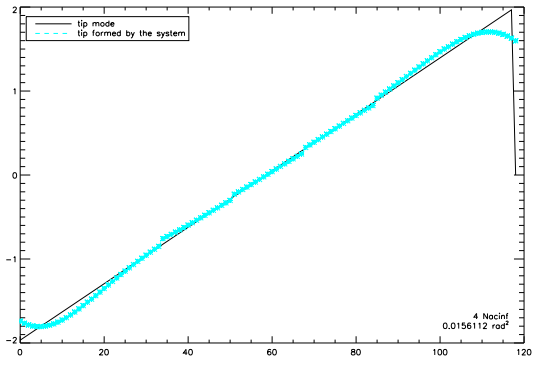


Figure 5.12: Answer of the mirror to a tip mode

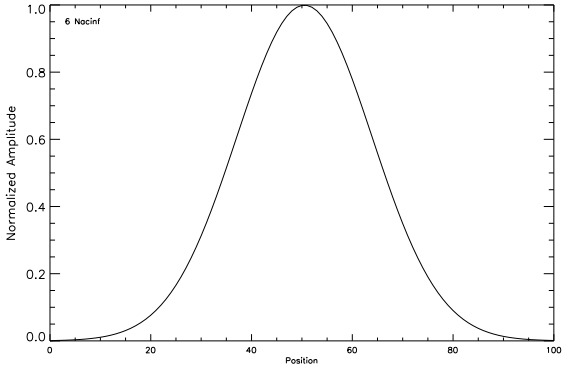


Figure 5.13: The IFs is set to zero beyond the third actuator from the center

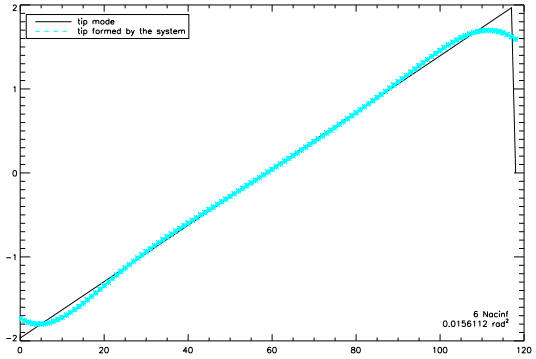


Figure 5.14: Answer of the mirror to a tip mode

has an impact on the DM unless $\frac{L_0}{D} = 1$. In the following we take care of the impact of the outer scale on the turbulent and we try to build a phase screen that scales $2 \times L_0$.

5.5.4.2.1 Analytical analysis It is important at this step to quantify the performance of the modelized mirror, by comparing the fitting error given by the DM after correction to an analytical formula using the formalism of Fourier.
The analytical method provides a simple expression for the fitting error of the DM. We evaluate the influence of the actuators number on the fitting error. We compare it with the numerical simulation.
As part of the Fourier analysis, the DM is considered as a Low-pass perfect filter: it is able to correct the phase fluctuation below its cut-off frequency forming the DM subspace noted by the D domain, as a consequence, the highest spatial frequencies are not corrected by the DM. Based on this principle the fitting variance is given by:

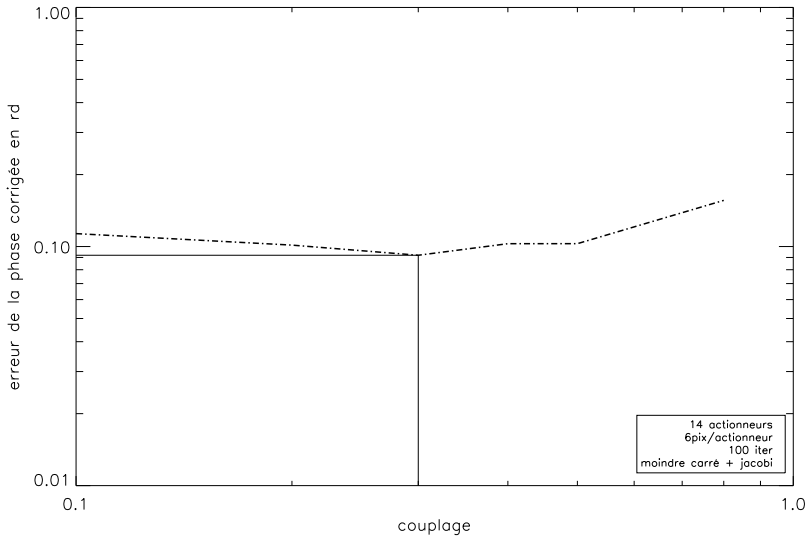


Figure 5.15: Minimisation of the mechanical coupling in terms of the residual phase formed by the DM of 14 linear actuators, using an iterative resolution with Jaccobi preconditionner

$$\sigma^2 = \int\int PSD_{turb}(f)F_D(f)df \tag{5.7}$$

where $F_D(f)$ equals 0 if f is in D, 1 otherwise. $PSD_{turb}$is the spatial power spectral density of the turbulent phase, since the low frequencies are corrected one can neglect the effect of finite outer-scale and take with a good approximation the Kolmogorov spectrum, hence:

$$PSD_{turb}(f) = \frac{0.023}{r_0^{5/3}}|f|^{-11/3} \tag{5.8}$$

It is necessary to define properly the domain D for a given geometry of the actuators. D is related to the value of the space between actuators so-called pitch: the smaller this value the larger is the frequency domain covered by the DM. Assuming a square grid of actuators with a given pitch, and based on Shannon theorem one can consider that D is in this case a square area of the Fourier domain delimiting the region: -fc < fx < fc ; -fc < fy < fc with fc=1/(2.pitch). The numerical integration of the expression 5.7 is then given by [Rigaut et al. (1998)]:

$$\sigma^2_{fitting} = 0.232(\frac{pitch}{r_0})^{5/3} \tag{5.9}$$

This analytical expression allows us to understand the performance of the mirror, and gives us a previous idea about what we can expect from the mirror. However, the Fourier analysis presents some limitations, it does not account for edge effects related to finite aperture and central occultation. It does not account either for any specific IF shape and hence the coupling between the actuators, which could induce an uncorrected residual at low frequencies. For all those reasons we present a numerical fine analysis and we compare it with the Fourier formalism.

5.5.4.2.2 Numerical analysis In this paragraph we present the numerical simulation done in order to minimize the fitting error in terms of number of actuators on the DM. We consider a classical AO system for a telescope of 8m of diameter. This AO system is used to correct an atmospheric turbulence of $r_0 = 0.11m$ at 500nm and $L_0 = 25m$. The pupil is presented by 256 pixels. So we build in RCO format the IFs matrix with mechanical coupling fixed to 45% and *Nacinf* to 6, and an RCO linear on-axis projector. For the reconstruction we use an iterative method based on a conjugate gradient with a Jaccobi preconditioner, this methods is described carefully in section 5.6 .
Now we care about the number of actuators of a DM to correct the atmospheric turbulence of $r_0 = 0.11m$ at 500nm. We calculated the fitting error for different number of actuators. We studied the case where the number of actuator is 17, 33 and 65, the pitch presented in equation 5.9, vary at the same time so that the pupil is always presented by 256 pixels. We calculate the fitting error by using the analytical expression 5.9 and using the simulator E2E-S with the simulation presented above.

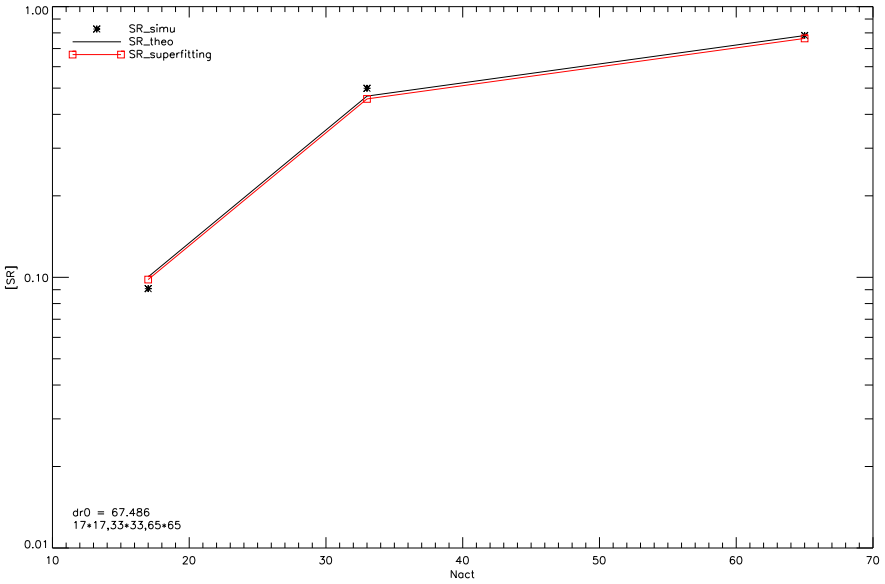


Figure 5.16: Comparision of the fitting error in terms of the number of actuators presented on the DM using the Fourier formalism or a numerical simulation with E2E-S, where the mechanical coupling is fixed to 45%.

5.6 Sparse Wave Front Reconstruction

We care about developing an E2E sparse code dedicated to the future and extremely large telescopes, wide field of view tomography has to be well managed using the sparse row wise representation. In this section we establish the equations describing the wide FOV tomography comprising n_{GS} (number of GS or WFS number), n^l (number of turbulent layers) and the turbulence propagation toward the pupil telescope. This model is a generalisation of any AO system, it may thereafter be applied to any AO system such as classical AO , LTAO , MOAO , MCAO...

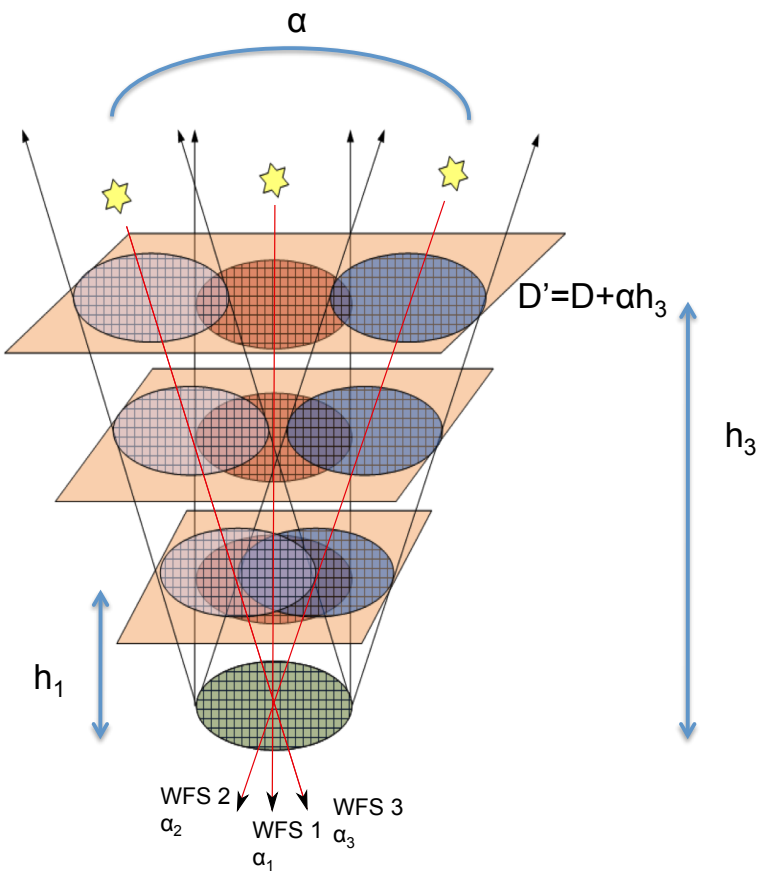


Figure 5.17: Principle of an AO wide field of view system of a diameter D, using 3 turbulent layers and $n_{GS} = 3$

This chapter is dedicated to the tomography for a generalized AO systems. The LGS issues are not considered in this chapter and the concepts are developed given the analysis of a plane propagation of wave front.
It is important to note that the tomography study for a natural guide star case can be easily transmitted to the laser guide stars by taking into consideration the geometrical aspect of the spherical wave front. The LGS case is the subject of part [III] of this dissertation.
In this section we add to the model, the multi WFS measurement. In this case and given

the slopes measurements of the phase by a SH WFS, we inverse the problem in order to turn back to the turbulent volume and reconstruct the atmosphere modelized by the thin turbulent layers.
In this section we don't care about the correction by DM, assuming that the turbulent phase is composed of a discrete sum of thin turbulent layers located at different heights [Roddier (1981)]. We explicit the propagation equation from the turbulent layers to the pupil plane of the telescope of diameter D.
We considered a turbulent volume modelised by as a series of n^l turbulent layers statistically independent, each layer is positioned by its altitude from the pupil by h_l, and characterized by a turbulent phase φ_h^{tur} defined on a metapupil of diametre $D_{meta} = D + \alpha h$, where D_{meta} is the diameter of the footprint limited by the FOV α. The definition of the footprint is applicable for a small α, which is typically the case in the AO systems. D_{meta} can be explained as the footprint of the pupil at different altitude for two guide stars separated by α as it is shown in figure 5.17.

For a given turbulent profile, the atmosphere is presented as the sum of different thin layers statistically independent. Assuming the near-field approximation, the phase recognized by the telescope pupil plane in a given sky direction α_i is given as the sum of the contributions of the phase from all the layers:

$$\varphi_{\alpha_i}^{tur}(r) = \sum_{l=1}^{n_l} \varphi_l^{tur}(r + \alpha_i h_l) \tag{5.10}$$

where r is the coordinate of the phase in the grid at the altitude h_l and n_l is the total number of turbulent layers.

This phase $\varphi_{\alpha_i}^{tur}(r)$ is then analysed by a SH WFS for the different sky directions, and a vector of slopes is then provided as an output by the WFS sub-system. An inverse problem has to be resolved in order to go up back and reconstruct the atmosphere.
Next we assume that the phase measured by the SH is the result of all the contribution of the layers in the pupil of the telescope
The phase measured by SH for a given sky direction in the pupil of the telescope can then be written as:

$$\varphi_{\alpha_i}^{m}(r) = \sum_{l=1}^{n_l} \varphi_l^{tur}(r + \alpha_i h_l) + n_i \tag{5.11}$$

where n(i) is the vector of noise propagated on the sub-aperture of the WFS.
In our approach the turbulent phase in the volume denoted by ϕ^{tur} is represented by the concatenation of different grids of turbulence (zonal approach) for all the layers:

$$\phi^{tur} = \begin{pmatrix} \varphi^{tur}_{h_1} \\ \varphi^{tur}_{h_2} \\ \vdots \\ \varphi^{tur}_{h_n} \end{pmatrix} \tag{5.12}$$

For the sake of simplicity, we can rewrite 5.11 in a matrix form.

$$\phi^{m}_{\alpha} = P^{h}_{s,\alpha}\phi^{tur} + n \tag{5.13}$$

Where $P^{h}_{s,\alpha}$ is a linear operator relative to the propagation in the analysis direction α. In the next paragraph we are going to explicit the sparse projector P_s (the s is set to say sparse), for the case of natural guide stars, and it will be generalized for the laser guide stars case in chapter 7.

5.6.1 Propagation $P^{h}_{s,\alpha}$

$P^{h}_{s,\alpha}$ is the projector that performs the phase propagation from a support of a D diameter at a layer h and add in the pupil of the telescope all the contribution coming from all the layers for the same sky direction α_i. This projector is based on a bilinear interpolation providing a non integer pixel lag as it is shown in figure 5.18.

$P^{h}_{s,\alpha}$ is the concatenation of the different projectors P^{l}_{s,α_i}. All the blocks are formed by 4 diagonals at different positions regarding the position of the support in the metapupil grid of diameter D to be selected and allowing the bilinear interpolation. Each block is of $N^2 \times N^2$ where N^2 is the dimension of the grid at the highest layer h_l so $P^{l}_{s,\alpha}$ is a rectangular sparse matrix of $N^2 n_l \times N^2 n_\alpha$. Each block is build using the RCO scheme, only the nonzero entries on the 4 diagonals are stored.
So equation 9.4 can then be written as:

$$\begin{pmatrix} \varphi^{\alpha_1}_{pup} \\ \vdots \\ \varphi^{\alpha_i}_{pup} \\ \\ \vdots \\ \varphi^{n_\alpha}_{pup} \end{pmatrix} = \begin{pmatrix} P^{h_1}_{\alpha_1} & \cdots & P^{n_l}_{\alpha_1} \\ & \ddots & \\ P^{h_l}_{\alpha_i} & \cdots & P^{n_l}_{\alpha_i} \\ \vdots & & \vdots \\ P^{h_1}_{n_\alpha} & \cdots & P^{n_l}_{n_\alpha} \end{pmatrix} \begin{pmatrix} \varphi^{tur}_{h_1} \\ \varphi^{tur}_{h_2} \\ \vdots \\ \varphi^{tur}_{h_n} \end{pmatrix} + \begin{pmatrix} n_{\alpha_1} \\ \vdots \\ n^{\alpha_i} \\ \\ \vdots \\ n_{n_\alpha} \end{pmatrix} \tag{5.14}$$

The projector $P^{l}_{s,\alpha}$ can be seen as the interaction matrix, given the turbulence in the volume we obtain the measurements at the pupil of the telescope. In order to simplify the notation of the projector, we are going to use P_s instead of $P^{l}_{s,\alpha}$.

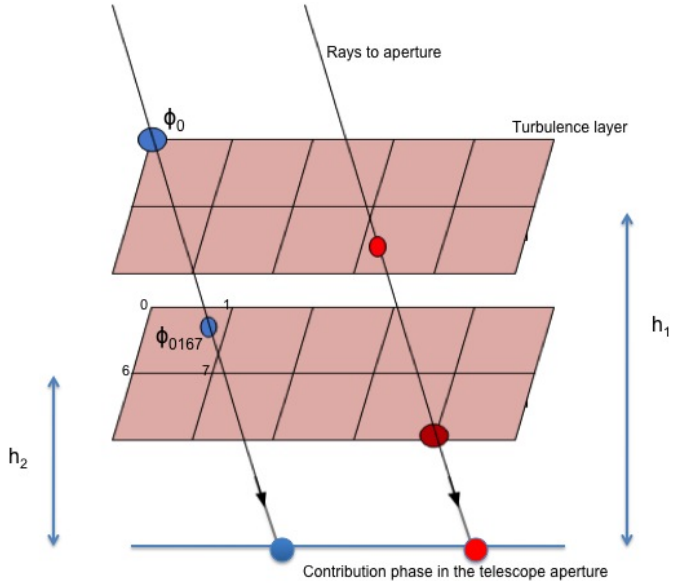


Figure 5.18: Projector matrix model. 2 layers are presented, rays traced from the guide stars (GS) through the phase screens to obtain the total contribution in the telescope aperture plane. The blue phase in the telescope aperture is then the sum of φ_0 and φ_{0167}, this last is obtained by a bilinear interpolation given $\varphi_{0,1,6and7}$

5.6.2 Maximum *A Posteriori* estimator

The phase statistics results from a stochastics independent process, caused by atmospheric turbulence. The statistics of the phase in the pupil is assumed to be Gaussian, centered. In addition, the noise propagation through the SH measurement process is linear with the phase . Therefore, it can be demonstrated that the MMSE and LMMSE solutions seen in paragraph 2.4.4.3 are equivalent to the Maximum *A Posteriori* (MAP) [Van Trees Harry. L. (1968), Demoment (1989), Conan et al. (1998)]. Hence, we look to the most probable phase in each turbulent layer given the phase measurements obtained in the different sky directions $\phi^m_{\alpha_i}(r)$ in the pupil of the telescope. From Bayes theorem of conditional probabilities we have:

$$P(\varphi_l|\phi^m_{\alpha_i}(r)) = \frac{P(\phi^m_{\alpha_i}(r)|\varphi_l)}{P(\phi^m_{\alpha_i}(r))}.P(\varphi_l) \tag{5.15}$$

where $P(\phi^m_{\alpha_i}(r)) = 1$ since it is the phase measured by the SH and $P(\varphi_l)$ is the so-called Bayesian *a priori*, that regularises the problem and helps the inversion as it contains the *a priori* information on the unknowns referring here to the phase on each turbulent layers.

$$P(\varphi_l) \propto \prod_{l=1}^{n_l} exp(-\frac{1}{2}\varphi_l^T C^{-1}_{kol,l}\varphi_l) \tag{5.16}$$

where $C_{kol,l}$ is the covariance matrix of the phase for each turbulent layer. We suppose that the phase follows the statistics of Von Karman or Kolmogorov. For each turbulent layer this matrix is defined in terms of $r_{0,l}$ (Fried's parameter) of the considered l layer. Assuming that the WFS subaperture noise is a gaussian statistics with zero mean and standard deviation $\sigma_{n,i}$, and the noise is uncorrelated between the subapertures, $< n_i n_j >= \delta_{ij}\sigma^2$, the likelihood term can be evaluated as:

$$P(\phi^m_{\alpha_i}(r)|\varphi_l) \propto exp(-\frac{1}{2}\frac{||n||^2}{\sigma_i^2}) \tag{5.17}$$

The MAP estimator consists of maximizing the *a posteriori* probability $P(\varphi_l|\phi^m_{\alpha_i}(r))$ which is equivalent to minimizing the negative of its logarithm:

$$\hat{\varphi}_l = \underset{\phi}{\text{argmax}}\, P(\varphi_l|\phi^m_{\alpha_i}(r)) \tag{5.18}$$

$$= \underset{\phi}{\text{argmin}}(-ln(P(\varphi_l|\phi^m_{\alpha_i}(r)))) \tag{5.19}$$

to minimize the criteria:

$$J(\varphi_l) = \frac{||n||^2}{\sigma^2} + \sum_{l=1}^{l=n_l} \varphi_l^T C^{-1}_{kol,l}\varphi_l \tag{5.20}$$

$$= \sum_{i=1}^{i=N_{mes}} n^T C^{-1}_{n,i} n + \sum_{j=1}^{j=n_l} \varphi_l^T C^{-1}_{kol,l}\varphi_l \tag{5.21}$$

By injecting equation 9.4 in 5.21, we can rewrite it using the matrix format:

$$J(\phi) = [\phi^m_\alpha - P_s\phi^{tur}]^T C_n^{-1}[\phi^m_\alpha - P_s\phi^{tur}] + \phi^T C^{-1}_{kol}\phi \tag{5.22}$$

Minimizing equation 5.22 the estimated phase in the layers can then be written as [Fusco et al. (1999b)]:

$$\hat{\phi}^{tur} = (P_s^T C_n^{-1} P_s + C^{-1}_{kol})^{-1} P_s^T C_n^{-1} \phi^m_\alpha \tag{5.23}$$

The phase covariance matrix, which will be detailed later since it is used in the E2E-S, can be seen as a regularisation term. It allows the problem to be inverted, moreover it is important to note here that C_{kol} offers the discrimination of the phase at each layer by providing the *a priori* knowledge of the turbulence strength at each layers given by the profile models C_n^2.

5.6.2.1 Sparse Noise covariance matrix C_n

As far as the noise in the different sub-aperture are not correlated, the noise covariance matrix will be a $m \times m$ diagonal matrix with σ_m^2 is the value of the diagonal. Assuming that the noise is uniform on all the sub-apertures, we have the same noise propagated on the full and partly illuminated sub-aperture. For that the inverse of the noise covariance matrix is then the noise variance times the identity matrix: $C_n^{-1} = \sigma_m^{-2} I$.
Equation 9.6 may be simplified to

$$\hat{\phi^{tur}} = (P_s^T P_s + \sigma_m^2 C_{kol}^{-1})^{-1} P_s^T \phi_\alpha^m \tag{5.24}$$

5.6.2.2 Turbulence Covariance matrix C_ϕ

Assuming a Kolmogorov turbulence spectrum or a Von Karman turbulence spectrum, the phase covariance matrix C_{kol} is nonsparse and of full rank, and hence its inverse C_{kol}^{-1} is ill conditioned. E2E-S is developed to be sparse, implementing a sparse direct solver is well needed. However some modest approximation must be made to render it sparse and to proceed by using the sparse techniques providing by the numerical sparse code.
We adopt the approximation derived by [Ellerbroek (2002)], according to the author:

$$C_{kol}^{-1} \approx \gamma \nabla^4 \tag{5.25}$$

where γ is a constant, ∇^2 is the Laplace curvature operator. The approximation lies in adopting an integer-exponent power law for the turbulence power spectrum so that the Kolmogorov turbulence power spectrum is tweaked into the form $PSD_{kol} \propto k^{-11/3} \approx k^{-4}$, where k is the radial component of the spatial frequency. This yields to approximate C_{kol}^{-1} in the case of a discrete turbulence layer as:

$$C_{kol}^{-1} \approx C^T C \approx \gamma \nabla^4 \tag{5.26}$$

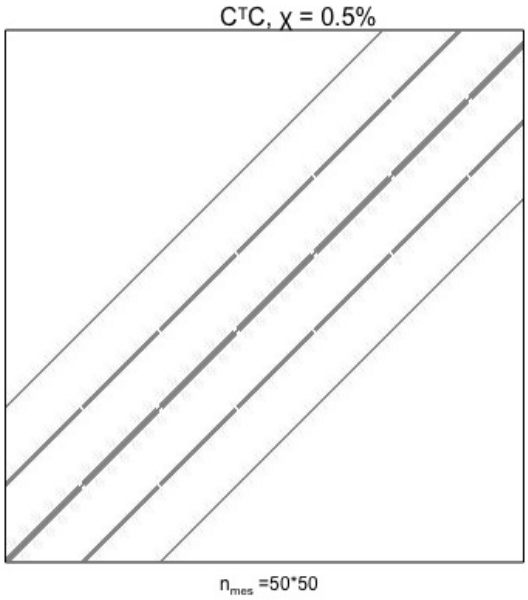


Figure 5.19: A sparse approximation of C_{kol}^{-1} represented for a grid of 50×50 in the pupil of the telescope, the matrix is 0.5 % filled.

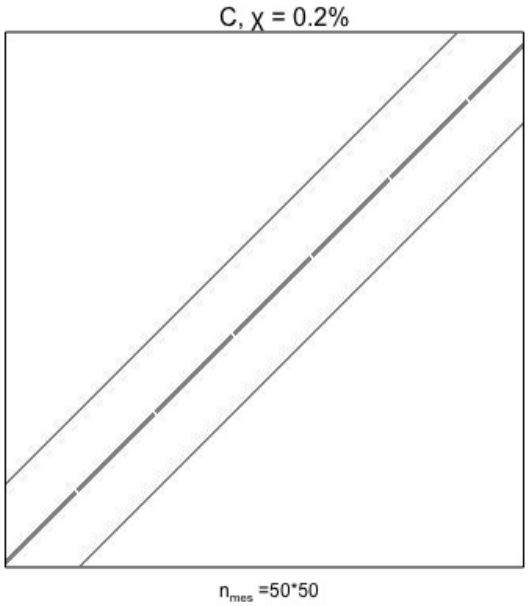


Figure 5.20: The laplacian operator ∇^2 represented in sparse RCO scheme attains a sparseness of 0.2%.

where C is proportional to a discrete approximation of the Laplace operator ∇^2. A second order accurate finite-difference given by Taylor approximation can be used to approximate the two-dimensional Laplace ∇^2 in OxOy by:

$$\nabla^2\varphi(x,y) = \frac{\partial^2\varphi}{\partial x^2} + \frac{\partial^2\varphi}{\partial y^2}$$

5.6.2.3 Cholesky factorization

Given a symmetric matrix A, for any vector x, if the product x^TAx is positive then it exists a lower triangular matrix L so that the Cholesky Decomposition of A is given by :

$$A = LL^T \tag{5.27}$$

The full-rank linear system $Ax = b$ can be computed by successive forward and back substitutions to solve the triangular systems

$$Ly = b \tag{5.28}$$

$$L^T = y \tag{5.29}$$

Both sytems lower and upper triangular respectively, can be solved sequentially by forward- and back-substitution, which can be carried out efficiently if the matrix L is sparse.
In E2E-S the Cholesky decomposition is used solving the operator of reconstruction given in equation 9.8, where:

$$\begin{gathered} A = P_s^T P_s + \sigma_m^2 C_{kol}^{-1} \\ b = P_s^T \phi_\alpha^m \\ x = \hat{\phi^{tur}} \end{gathered}$$

If A is sparse, then during the factorization, some entries that are initially zero in the upper triangle of A may become nonzero entries in L. These newly created nonzero entries of L are known as *fill*-in. The amount of *fill*-in generated can be decreased by carefully reordering the rows and columns of A prior to factorization, otherwise the *fill*-in may increase the cost memory and the computational time which might render the method unattractive. *Nested dissection ordering* is a method due to Alan George (1973), which aims to minimize the *fill*-in during Cholesky decomposition, for curious readers you can find more details in the context of adaptive optics in [Cochran (1986)].
The Cholesky algorithm only computes the lower triangular factor, which roughly have the number of operations and the amount of memory required. Only the lower triangular part of matrix A needs to be computed and assembled in the memory.

5.6.2.4 Conjugate Gradient

Conjugate gradient [CG] is the most popular iterative method for solving large linear $m \times n$ systems of the form $Ax = b$, where x is an unknown vector, b is a known vector and A is a known square, symmetric, positive-definite matrix. Such a method seems to be particulary suitable with our sparse systems.
The basic idea is to define a quadratic function to be minimized of the vector $x\, f(\mathrm{x})$ with the form

$$f(x) = \frac{1}{2} x^T A x - b^T x + c \tag{5.30}$$

The gradient of $f(\mathrm{x})$ is then given by

$$f'(x) = \frac{1}{2}A^T x + \frac{1}{2}Ax - b \tag{5.31}$$

Or A is symmetric positive-definite matrix, 5.31 reduces to

$$\nabla f(x) = Ax - b \tag{5.32}$$

So $Ax = b$ can be solved by finding an x that minimizes f(x). More information about the CG can be found in [Shewchuk (1994)].

5.6.2.4.1 Preconditioning The CG method works well with the sparse matrix that is well conditioned. Suppose that the matrix A is ill-conditioned, it may be useful to apply a preconditioner M to the linear system so that $M^{-1}A$ has less condition number.

$$M^{-1}Ax = M^{-1}b \tag{5.33}$$

which has the same solution as $Ax = b$ but may be easier to solve, The optimal preconditioner would be the inverse of A, i.e $M^{-1}A \approx I$. Such implementation requires an additional VMM of the form $Mz_i = r_i$ at each CG iteration, entailing more computational time cost, thus if we are looking for a gain by applying a preconditioner it is obvious to require that $Mz_i = r_i$ is solved within the $O(N_{CG})$ operations
Many preconditioners with different strengths and applications have been developed, we site the Jacobi Preconditioner [Kelly C. T (1995)], known as the Diagonal Preconditioner, derived from the Jacobi Iterative Method. It applies the inverse of the diagonal entries of A to both sides of the equation, with the hope of reducing the condition number. If matrix A were diagonally dominant, the inverse of its diagonal may be a good approximation to the inverse of A itself.
The complete preconditioned conjugate gradient (PCG) algorithm is given as follow

$$\alpha_i = \frac{r_i^T M^{-1} r_i}{d_i^T A d_i} \tag{5.34}$$

$$r_{(i+1)} = r_i + \alpha_i A d_{(i)} \tag{5.35}$$

$$\beta_{(i+1)} = \frac{r_{(i+1)}^T M^{-1} r_{(i+1)}}{r_i^T M^{-1} r_i} \tag{5.36}$$

$$d_{(i+1)} = M^{-1} r_{(i+1)} + \beta_{(i+1)} d_i \tag{5.37}$$

x_0	;initial guess for the solution
$r_0 = b - Ax_0$	;initial residual
$d_0 = r_0$	;initial search direction
begin iterations until the residual is below a definit tolerence level	
$\alpha_i = \frac{r_i^T M^{-1} r_i}{d_i^T A d_i}$	;optimal step size
$Mzi + 1 = r_{(i+1)}$	;Jacobi preconditioner
$d_{(i+1)} = z_{i+1}\beta_{(i+1)}d_i$	;updating search direction
$x_{i+1} = x_i + \alpha_i d_i$	
$r_{(i+1)} = r_i + \alpha_i A d_{(i)}$	;updating residual
$RMS(r_{i+1}) < threshold$	; Indicator to terminate the reccursion
end iterations	

Table 5.2: Preconditioned conjugate gradient solver for a symmetric positive definite sparse linear system, with Jacobi preconditioner M. This algorithm is implemented straight out of Numerical Recipes, with the matrix-vector multiplications carried out sparsely by the ruoxv(a,v) function. Note that when M is identity, PCG reduces to CG

- The number of iteration needed to reach the threshold directly impacts on the computational cost of E2E simulator.

- Ralph Flicker [Flicker (2003)] showed that the quality of WF reconstruction is not very sensitive to the threshold level. Even with a threshold variation on a range of 10^7 of increase, the PCD iterations number decrease by a factor of 100 without a significant loss of AO performance. In our case we found that $47 \times 10^{-}7$ provide an optimal WF reconstruction.

5.6.3 Conclusion

In this section we presented a sparse tomography model based on a sparse rectangular projector build using the efficient RCO sheme. It transmits the contribution in the pupil of the telescope of the turbulent phase from all the layers and for all the sky directions. This phase is then measured by the SH model. We show then the MAP reconstructor in a sparse format using a modest approximation for the inversion of the phase covariance matrix C_ϕ^{-1} playing the role of the regularization term. The MAP recontructor is then solved by an iterative method, the conjugate gradient where we ensure a fast convergence with the Jaccobi preconditioner PCG. Setting a zero initial vector and a relatively low tolerance of 10^{-5}, the PCG scales as $O(n^{3/2})$.

5.7 Validation of the code on an AO system

This section is dedicated to the first validation of the different modules developed in the previous section. We present first of all a simulation in a simplified framework combining the wavefront generator and the DM module, then we propose simulations for a classical AO system. And finally we show the efficiency of the code in terms of number of degrees of freedom comparing it with the CAOS numerical tool.

5.7.1 First simulation: Turbulence Case study

We propose a simulation case study, in order to verify the operation of the turbulent generator and the DM module. This case study can be decomposed into four parts:

- A configuration module combining the compilation of the SOY library and all the other functions calling by simulation. It contains the parameters characterizing the system and needed for the case study.
- Turbulence generator: we simulate one phase screen respecting the von Karman DSP, of 4096×4096 pixels. This phase screen is then scaled in order to meet the desired turbulence characteristics (D/r_0, L_0, altitude, speed of the wind, and for sure the turbulence profile Cn^2, etc)
- Calibration, consists in building the DM sparse influence functions f_S in the RCO format so that $\phi^{corr} = F_s u$ where u are the voltages to be applied to the mirror in order to generate the DM corrected phase ϕ^{corr}. So an inverse problem has to be solved: $u = (F_s^T F_s)^{-1} F_s^T \phi^{tur}$, where $(F_s^T F_s)^{-1} F_s^T$ is the projector of the phase to the DM.
  Using the RUOPCG routines described in table 5.2 there is no need to calculate the inverse of $(F_s^T F_s)$ otherwise, we calculate $F_s^T F_s$ to be applied to the voltage unknown to iterate the linear equation: $F_s^T F_s u = F_s^T \phi^{tur}$. Figure 5.21 show the matrix $(F_s^T F_s)$ obtained given the influence function Fs. This matrix represents the covariance matrix of the influence sparse functions.
- Over 4000 iterations we translate at each cycle the turbulent phase by a factor of vt where v is the wind speed and t is given by the inverse of the sampling frequency. We cut then a grid having the same number of pixels as the influence function to obtain the ϕ^{tur} using then to calculate the vector of voltage u by resolving the linear model given above, u is then applied to the mirror to generate the ϕ^{DM}.
  Table 5.3 summarizes the conditions of the turbulence for our simulation case for a VLT telescope type represented by 119×119 pixels at the pupil.
  The figure 5.22 represents the variance of the Zernike modes simulated and analytical, over 4000 iterations.

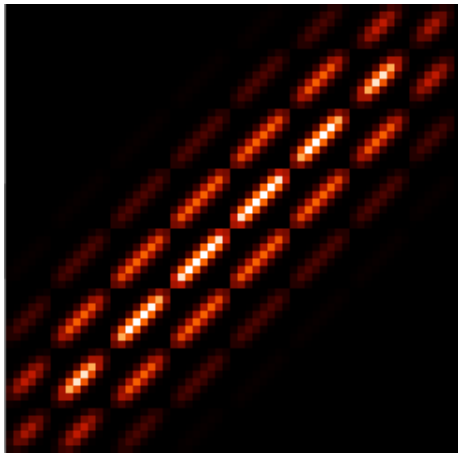


Figure 5.21: Covariance matrix $F_s^T F_s$ of the sparse influence functions (8×8 actuators). Each row or column of the matrix corresponds to an actuator of the mirror.

Altitude of the turbulent layer (m)	0
C_n^2 (%)	100
Wind speed (m/s)	28
Sampling frequency(Hz)	500
D/r_0	7
L_0 (m)	100

Table 5.3: Turbulence conditions for the considered study case

The WFS is supposed to be perfect so just the fitting error is taken into consideration. Over 4000 cycles we find a residual DM error of $\sigma^2_{fitting_{simu}} = 0.257rd^2$ which is close to the analytical *fitting* error [equation 5.9] given by $\sigma^2_{fitting} = 0.232rd^2$ since the pitch or the space between actuators is equal to r_0 in our simulation case. In figure 5.23 we present the PSD of the turbulent phase, generated by the mirror and the residual phase.

5.7.1.1 Efficiency of the E2E-S

The final purpose of developing this sparse numerical tool is to simulate the EAGLE multi-object spectrograph, a flagship instrument of the future E-ELT. As it is shown in chapter [5.3] the RCO format storage allows us saving memory and provide a fast VMM comparing to the full matrices operations. It is important now to make a comparison test for the same simulation using the new developed E2E-S and the CAOS numerical code described in [4.2.3.1.1]. We are looking to the computational load and the efficiency in bringing it down and we don't care in this test about the ultimate AO performance. For that, we are going to increase the number of subapertures and calculate the calibration time and the reconstruction time that correspond to each simulation case using both CAOS and E2E-S.

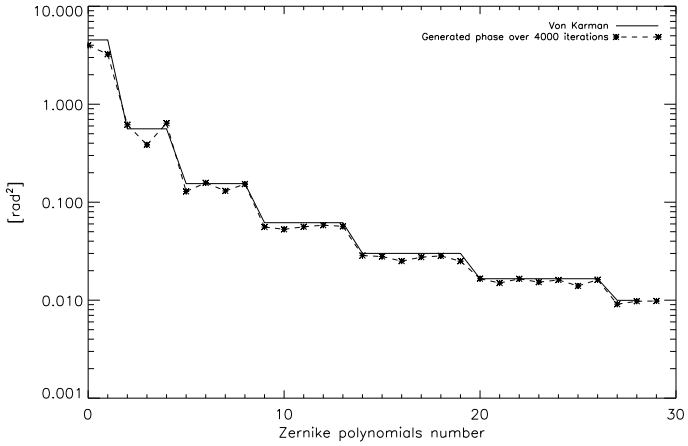


Figure 5.22: Variance of the Zernike modes simulated and analytical, over 4000 iterations for the given parameters: $L_0 = 100m, D/r_0 = 7$.

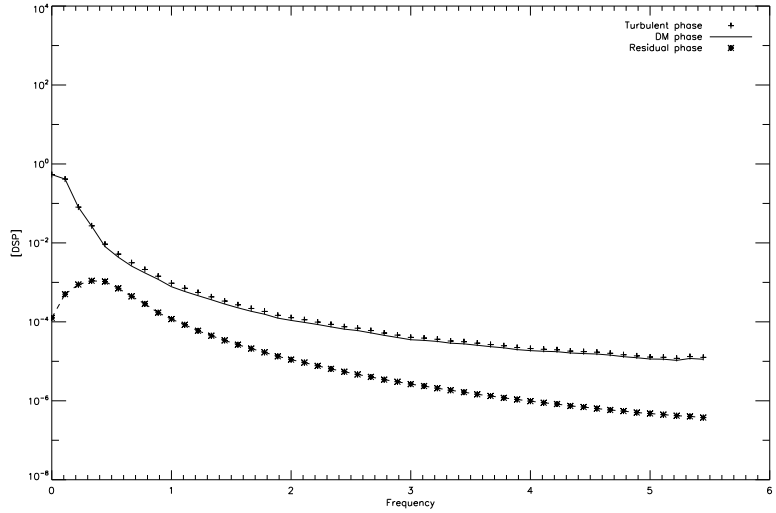


Figure 5.23: PSD of the turbulent phase, generated by the mirror and the residual phase, The x-axis is on f/pitch.

We consider a simple AO case:

- 1 layer
- 1 GS direction
- 6 pixels per subap
- N iterations = 100

In figure 5.24 we show in black the computational time needed to achieve the E2E simulation using the E2E-S, this computational is the sum of the calibration and simulation

time:

- Calibration time: which corresponds to the calculus of all the matrices needed to execute the simulation such as the DM influence functions Fs, WFS matrix, projector matrix Ps, phase covariance matrix and the control matrix. These matrices are computed once for all.
- Simulation time: corresponds to the time ellapsed for E2Es to estimate one realisation of wave front. Using our sparse code we were able to generate and build matrices using the RCO storage for 201×201 subapertures system in about 3 hours and a half, and 8.9 minutes for the simulation time.

The fluctuation in the time needed by the simulation, is because of the phase generator based on the FFT function. The running time is related to the decomposition of the generated phase dimension into its prime factor, more this decomposition is short less is the time spent on the generation.

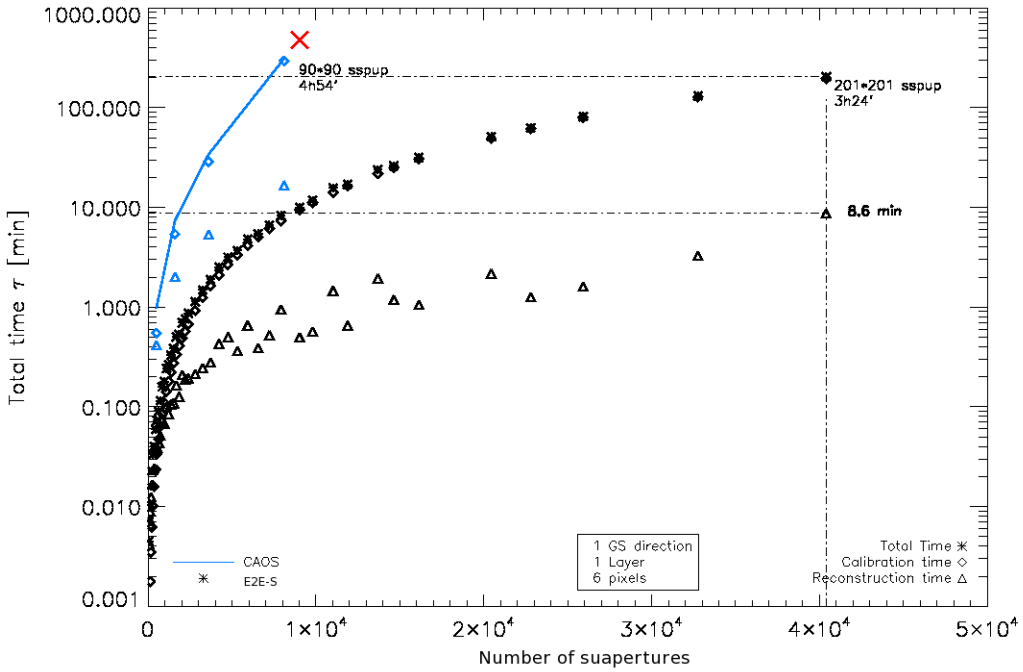


Figure 5.24: Computational time in terms of the number of subaperture for a simple AO case running over 100 cycles, we plot for comparison in blue line the time needed by CAOS to achieve the simulation calibration and iterations.

This test shows the speed of the E2E-S code comparing to CAOS. We are about 20 times faster for such a simulation case. Moreover, this code is dedicated for the E-ELT and so for the high degrees of freedom in the range of $[10^4, 10^5]$. This case of study

shows the capabilities of the E2E-S in handling matrices of big dimension, where we save memory while using the RCO storage format.
While in CAOS and using full real matrices, systems having more that 90×90 subapertures for on-axis correction cannot be simulated using such a numerical code.

Chapter 6

Conclusion

This part was dedicated to the AO simulation tools. In chapter [4.2] we field over all the existing codes analytical and numerical for simulating an AO system. The increase in the number of degrees of freedom (scales as the square of the telescopeś diameter) makes the existing codes useless or even not useful, as regards in practically the inversion and the matrix calculus. This is due to the calibration time, becoming hard to handle with the actual AO dimensions. We introduced in chapter [5] a new code based on an iterative resolution of the linear model with high degrees of freedom (using the sparse matrix). Where we show the gain in terms of memory and computational time while using the RCO scheme.

The implementation of the turbulence generator and the different AO sub-systems was presented and discussed in section [5.5], and therefore, the error budget while simulating an AO system with the developped modules such as the fitting and the aliasing errors. The iterative inversion of the linear model was then described in section [5.6], some modest approximation has been made for the phase covariance matrix.
Moreover, we propose some numerical validation of the developped E2E-S represented by different blocks refering the AO-sub-system in order to illustrate the operation of the different modules or bloks. A numerical E2E simulation is then proposed in order to validate the speed and the efficiency of the code in terms of the computational time, where we presented a comparison with the CAOS tool.
Our E2E-s sparse simulation tool is now fully validated. This tool will be used to perform simulation for EAGLE system in the following chapters.

Part III

Challenges of AO with Tomography

Chapter 7

LASER Guide Stars

7.1 Introduction

All new concepts of wide field Adaptive Optics for the next generation AO of Extremely Large Telescope (ELT) have in common that they require à priori knowledge of three dimensional turbulence volume, that for the study of the atmospheric tomography is quite necessary to well optimize the new problems coming with this new evolution. Moreover, the potential application of AO, both for imaging and for laser energy transfer, suffer from the lack of suitable reference sources. In an AO system we care about the data beacon measured by a wave front sensor in order to compensate for the effect of turbulence. This measured path must be in the isoplanatic patch [Fried (1982)] as the observed object, so that the system performance can still be nearly equal to the diffraction limited-value. Unfortunatly, a few objects of scientific interest are surrounded by bright stars to function as reference sources. To overcome the sky coverage limitations Laser Guide Stars (LGS) will be required in any desired direction to act as a high-order wave front reference.
The first studies of methods that did not rely on a natural source for measuring atmospheric distortion, were devised at Itek by *R. A. Hutchin*, starting from the *'ray method'* in 1978, where the Laser pulses are fired from multiple subapertures of the telescope, to the idea of creating an artificial source in the atmosphere in 1981 [Hardy and Thompson (2000)]. In the same time, the same idea was published by [Foy and Labeyrie (1985)] using the concept of pulsed laser backscatter from a region of the atmosphere. An experiment was achieved by [Thompson and Gardner (1987)] at the Mauna Kea observatory based on both Rayleigh scatter and resonant scatter from the sodium layer.

7.1.1 Outline of problems

Unfortunately their are additional error sources that must be taken into account with laser beacons. When using LGS as a source of reference instead of a natural reference source the following factors occurs:

1. The LGS is in random motion because of the atmospheric turbulence, providing tip and tilt indermination. In addition, the fluctuation of the sodium layer induce doubt of where the LGS is focalised and the system does not know where to assign the focus correction.

2. The cone effect also called Focus Anisoplanatism (FA) must be considered, since the source is formed within the earth's atmosphere and so the beam sample a cone-shaped volume of the turbulence in the optical path of the telescope. But fortunately the phase estimation error provided by the cone effect may be solved by using multiple laser guide stars, as proposed in [Tallon and Foy (1990), Welsh and Gardner (1991)].

3. Spot elongation: The sodium layer expands in the atmosphere between 80 and 100 km. It has a finite thickness ranging between 10 km and 20 km. Given this fact, the laser guide star is elongated along the thickness of the sodium layer. When measuring the laser guide star elongated by the WFS of type Shack-Hartmann a sub-aperture, located off-axis with respect to the laser projection axis, sees the extended light source elongated (see figure 7.1). Since every subaperture looks at the laser spot from a different angle, the elongation in each subaperture is different. This effect is a function of the radial distance of the sub-aperture from the telescope center and becomes maximized for a sub-aperture close to the edge of the telescope. In this dissertation we don't care about the elongation spot, and we just consider the tip,tilt, and defocus indetermination and the focal anisoplanatism.

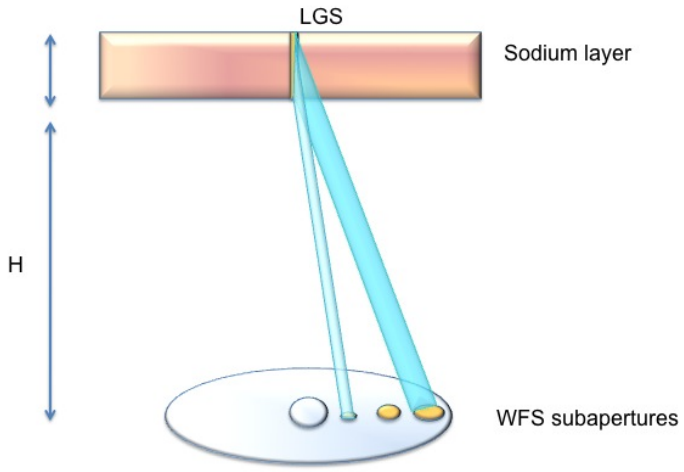


Figure 7.1: Spot elongation: nonsymmetrical elongation at the WFS subaperture, each sees the LGS from different angle, at the edge of the telescope pupil the elongation is maximum.

7.1.2 Types of LGS

The creation of an LGS in the atmosphere using a laser beacon relies on photon scattering processes that occur when a photon of the incident radiation field is annihilated while a

photon of scattered radiation is created. The processes of interest for AO are the Rayleigh scattering within the atmosphere and the Sodium scattering from the mesospheric sodium layer at 90 km. The physical principles of Laser scattering are not treated in this dissertation, further information can be found in [Hardy (1998), Humphreys et al. (1991), Viard (2001)]. Only a brief summery of the two common ways of creating reference sources, Rayleigh and Sodium scattering, will be given in the next two paragraphs. Although this work considers a resonance scattering in the mesospheric sodium layer at 90 Km.

7.1.2.1 Sodium resonance

Sodium LGSs are created by projecting a laser, which is tuned to the D_2 line of the sodium atom (589 nm), into the atmosphere. The laser light excites the sodium, and a 589 nm light is re-emitted. The laser generating sodium beacons must be tuned to the sodium 589 nm line, with specific pulse shape, spectral content, making current sodium lasers complex and expensive.
There are a few important issues with sodium LGSs. First the flux returned from a sodium beacon depends on many factors: the sodium density at 90 km varies from summer to winter, the best flux can be obtained from a sodium LGS is when the saturation occurs within the layer. Further techniques can be followed to increase the return flux from the sodium layer, such as matching the Doppler broadned linewidth of sodium at the LGS focal altitude, and controlling the output polarisation state of the laser.

7.1.2.2 Rayleigh scattering

Rayleigh LGS is formed when radiation is scattered from atoms or molecules with no change in frequency, such a scatter is also called elastic scattering process. The Rayleigh scattering cross section that characterise the efficiency of a scattering process, varies with wavelength as λ^{-4} so using lasers at shorter wavelengths helps to increase the efficiency of the Rayleigh LGS. A pulsed laser to generate a Rayleigh LGS is used to reduce the light pollution effects in the LGS-WFS. This type of LGS is used in many AO systems [Rutten et al. (2006),Rutten et al. (2006), Myers (2010)]. These systems also need a fast shutter to isolate the high altitude portion of the focused laser beam to make it appear star-like to the wavefront sensor.
However, low-altitude Rayleigh scattering can provide much more backscattered signal to an AO system. The higher altitude of the mesospheric sodium layer reduces the beam divergence of backscattered radiation and makes the light source more starlike; this factor makes sodium scattering the preferred method of producing an artificial beacon.

In this part we focus our study on the Tip, Tilt and deFocus (TTF) indetermination. We propose in paragraph [7.2] a new strategy for well managing these three modes, then we introduce in part [7.11] the extentions added to E2E-S in order to handle LGS simulations. We propose a global study based on the configuration of LGS in the field of view to obtain the best performance of an LTAO system, we compare the performance of an

LTAO system using LGS and NGS measurements for different configuration of GS.
In part 8 we propose a new concept of coupling between LGS and NGS in the entire process of tomographic reconstruction. Split tomography and integrated tomography are then compared, fusion data for Low Order and High Order with and without TTF are also presented.

7.2 *Tip, Tilt and Defocus* Indetermination

The random motion of the LGS because of the atmospheric turbulence, provides that the tilt in the outgoing path differs from the tilt on the incoming path as depicted in figure 7.2. Therefore, a laser beacon projected from the ground can not be used as a reference to measure the position of a scientific object. The LGS position uncertainty or the so-called tip tilt determination still remain a fundamental problem for adaptive optics system using a laser beacon as source of measurements as was discussed by [Rigaut and Gendron (1992)].

Moreover, the sodium layer is not static but ever changing [O'Sullivan et al. (2000)]. The mean altitude fluctuates, as well as the thickness and the sodium atom density vertical profile. The variation of the mean altitude of the sodium layer will affect the knowledge of where the LGS is focalized inducing a focus error that cannot be distinguished from optical turbulence and can lead to loss of AO performance.
In this section our goal is the atmospheric tomography given the LGS measurements. For all those reasons, it is necessary to remove the tip, tilt and defocus to the spherical wave front measurements.
In this section we are going to present a new strategy of filtering tip, tilt and defocus from the measurements vector data of a spherical wave front distortion. First of all, we tried to solve the tip and tilt indetermination by setting the mean slope to zero in paragraph [7.2.1.1]. This first method was not satisfactory, so we propose in paragraph [7.2.1.2] a new method for excluding the tip, tilt and defocus, that consists in finding a transformation matrix M to an orthogonal space that exclude the tip, tilt and defocus.

7.2.1 Investigation methods for *tip, tilt and defocus* modes filtering

We are looking for a measurements vector filtering out Tip, Tilt and deFocus (TTF), so we are going to modify the slopes to remove the overall TTF components.
We assume that the wave front sensor described in paragraph [5.5.3.2] provides linear slopes measurements of the spherical wave front distortion, represented by the data model:

$$S = D_s\phi + n \tag{7.1}$$

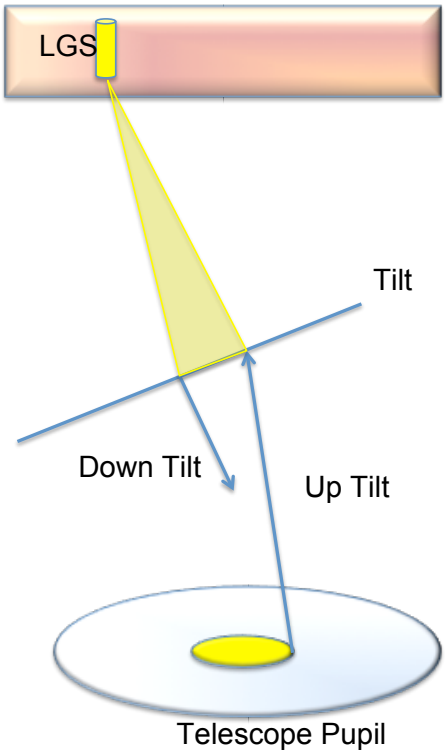


Figure 7.2: Outgoing laser beacon is refracted by the tilt of the atmosphere and the incoming beam is refracted in the oposite direction to the outgoing laser beam.

where, S is the data vector provided by the sensor, ϕ is a vector of the sampled wave front values, D_s is the answer of the wave front sensor to the incident spherical distortion and n is the vector of noise and the model error. We assume a SH WFS case with a realistic geometry model of fully and partially illiminated subapertures. The vector noise for instance and for sake of simplicity is not considered.

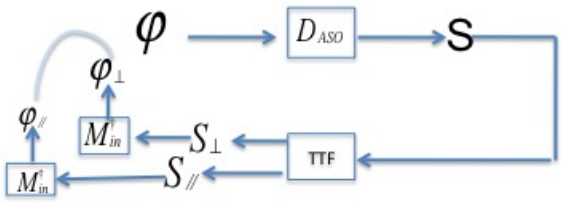


Figure 7.3: Model scheme review the procedure to be used given the slopes vector S and finding the space parallel and orthogonal to the tip, tilt and defocus

Figure 7.3 shows the procedure to be used in order to find the slopes vector out of TTF S_{OTTF} which is obtained by finding a transformation matrix to the orthogonal space $S_{//}$ and then reconstructing the high order wave front distortion using an appropriate reconstructor to be determined.
The vector slopes S_{OTTF} that excludes the TTF components can be written as:

$$S_{OTTF} = S - \alpha S_{TIP} - \beta S_{TILT} - \gamma S_F \tag{7.2}$$

where $\alpha S_{TIP}, \beta S_{TILT}$ and γS_F are the measurements to the contribution of TTF in the spherical incident wave front.
The estimate of the wave front given the WFS measurements is an inverse problem, which must be resolved using an iterative method with the proper conditioner. The approach commonly implemented in OA consists in taking as a direct model the operation that linked the measurements vector to deformations of the mirror, without passing explicitly by the phase phase. These relationships are grouped within an interaction matrix. The matrix D_s, which represents the influence of phase on the measurements, therefore it is never explicitly computed. This operations avoid the complexity on inverting the ill-conditioned WFS matrix. The interaction matrix $D_s F_s$ is obtained by applying voltages on the actuators and recording the individual measurements derived therefrom. The model is then given by:

$$S = D_s F_s u + n \tag{7.3}$$

This direct model linking the measurements to the voltages allows us to work on WFS space, a measurable and controllable space. (Readers can find more details about those space in [Correia (2010)]. The voltages can then be obtained by minimizing the following criteria

$$argmin||M_{in}u - S||^2 \tag{7.4}$$

where $M_{in}$is the interaction matrix defined above. As described in 5.6, there is no need to explicite the generalized inverse of the interaction matrix, i.e. the control matrix M_c is not explicitly calculated. However the PCG is used to iterate the model, thus the voltages are given by:

$$u = M_c S \tag{7.5}$$

Finaly the restored phase is given by:

$$\hat{\varphi} = F_s u \tag{7.6}$$

As shown in figure 7.3 we should seperate the measurement slopes space into orthogonal and parallel to the TTF modes so that the data vector can then be written as:

$$S = S_{//} + S_{\perp} \tag{7.7}$$

From equation 1.25 the phase can be decomposed onto phase out of TTF given by $\varphi_{\perp}$ and the tip, tilt and defocus contributions so we can evaluate the phase as:

$$\phi = \varphi_{\perp} + \alpha Z_2 + \beta Z_3 + \gamma Z_4 \tag{7.8}$$

The measurements out of TTF is the projection of S to $S_{\perp}$ which is given by:

$$S_{\perp} = D_{s\perp}(\varphi_{\perp} + \alpha Z_2 + \beta Z_3 + \gamma Z_4) = D_{\perp}\varphi_{\perp} = D_{s\perp}\varphi \tag{7.9}$$

$$D_{\perp} = (ID - MM^{\dagger})D_s \tag{7.10}$$

Where M is the transformation matrix in question to the orthogonal space which excludes TTF. So the restored orthogonal phase is then given by:

$$\hat{\varphi}_{\perp} = F_s u_{\perp} = M_c(ID - MM^{\dagger})D_s\varphi \tag{7.11}$$

Next we are going to discuss all the possible ways to find the matrix M.

7.2.1.1 First solution: Substraction of average slopes

The first solution for filtering tip and tilt is to substract to the slopes data its averages i.e to find a new data measurements S_{oTT} filtered out tip and tilt given by: $S_{hTT} = S - \bar{S}$. Then $MM^{\dagger}$ can be defined as the matrix that calculates the mean of the slopes vector, so that we can write:

$$MM^{\dagger} = \frac{1}{n}\begin{bmatrix} 1 & \cdots & 1 \\ \vdots & 1 & \vdots \\ 1 & \cdots & 1 \end{bmatrix} \tag{7.12}$$

Equation 7.9 evalulates to:

$$S_{OTT} = (ID - \frac{1}{n}\begin{bmatrix} 1 & \cdots & 1 \\ \vdots & 1 & \vdots \\ 1 & \cdots & 1 \end{bmatrix})S \tag{7.13}$$

Unfortunately, setting the mean slope to zero will not remove the overall tip/tilt components. In fact, this procedure will move the modes tip and tilt but it will also affects the other modes having contribution to the mean slopes. In another word we filter the first two modes but we recreate new modes that have the same answer on the WFS as the tip and tilt coming from the higher orders.
Figure 7.4 shows the unsatisfied result once we substitute the average of the slopes to the total data vector, where we show that this method did not filter out the total contribution of the tip and tilt in the spherical distortion.

As it is shown above the method of the mean slopes will not be the optimal solution for an estimated phase excluded from TTF. Now we are going to adress the second *solution* in finding the transformation matrix M to the orthogonal space .

7.2.1.2 Second solution: M contains the WFS answer to the *tip and tilt and defocus*

Theoretically the Zernike polynomials are orthogonal $<Z_i, Z_j>$ =0, where Z_i and Z_j are the modes of Zernike. We show above that their is no bijection between phase and slopes in terms of orthogonality of these polynomes, in another word assuming that the different Zernikes modes are orthogonal does not entails that the slopes of these modes or the answers of the WFS to these modes are orthogonal too. Given that we are going to propose that M should contain the answer of the WFS to the modes to be filtered, Tip and Tilt and Defocus in our case and equation 7.9 may be simplified to

$$\begin{aligned} S_{OTT} &= (ID - MM^{\dagger})S \\ S_{OTT} &= (ID - [S_{Tip}S_{Tilt}S_F][S_{Tip}S_{Tilt}S_F]^{\dagger})S \end{aligned} \tag{7.14}$$

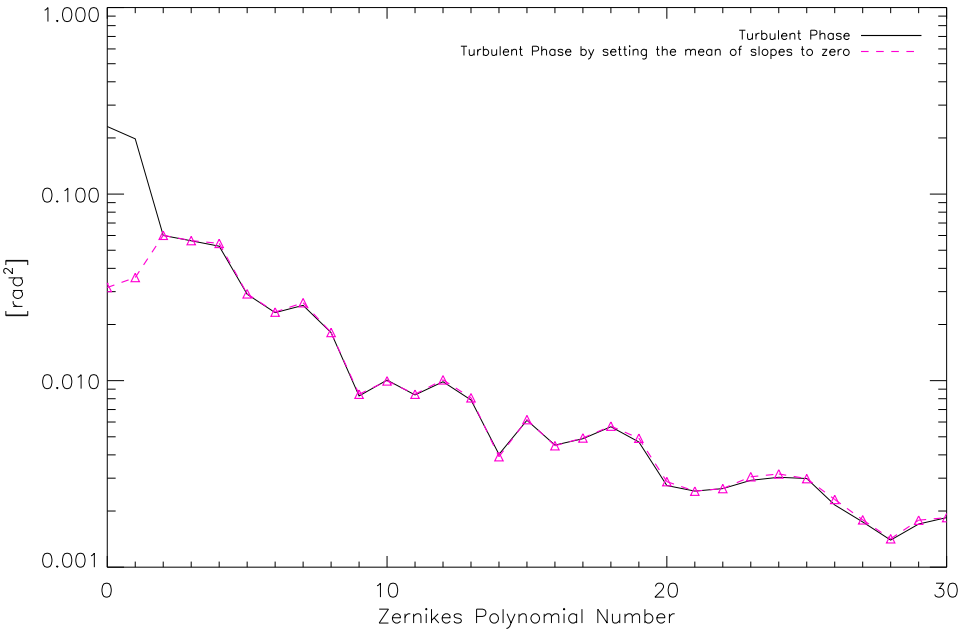


Figure 7.4: Projection of the turbulent phase onto the Zernike basis(solid line), the filtered phase (green triangles)

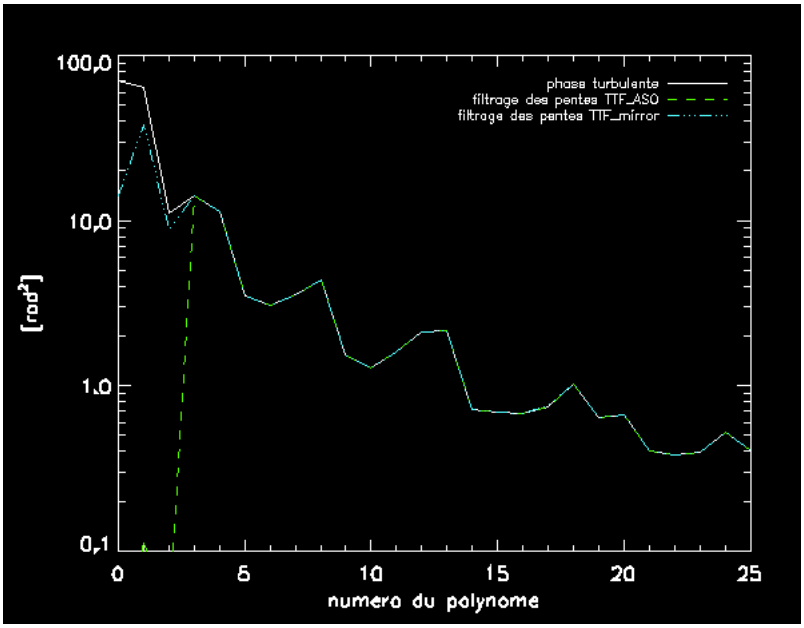


Figure 7.5: Comparison between a reconstructor used in our simulation(blue line) and the reconstructor via the WFS(green line), in the case where $M^{\dagger}$ is the generalized inverse of M

In figure 7.5 we show the unsatisfied result of solution 2 (the green line). The restored phase represented by the blue line contains always a significant part of the tip and tilt and defocus. Moreover it is shown that error on the focus mode didn't even decrease.
Trying to find out the source of the problem, we consider a SH sensor with the Fried's geometry, and we require that the D_s is well conditioned in this case. So no need to change the basis and the restored phase is done using the generalized inverse of the WFS matrix, which is simply inversible in this case. Given those assumptions the restored phase in equation 7.11 is modified to

$$\hat{\varphi}_{\perp} = D_{s\perp}^{\dagger}\varphi = (ID - MM^{\dagger})D_s\varphi \tag{7.15}$$

Equation 7.15 allows us to restore the phase excluded from the tip and tilt and defocus directly from the WFS basis as it is shown in figure 7.5.
Unfortunatly this is not a realistic case, so we can not consider it as a successful solution. Another sufficient solution has to be found.

7.2.1.3 Third solution: M contains the WFS answer to all the modes generated by the system

In this paragraph we propose that the transformation matrix M should always contain the answer of the WFS to tip and tilt and defocus, but the key exists in the generalised inverse of M, we propose in this solution 3 that the inversion should take into consideration all the modes generated by the DM. Therefore, the three lines of $M^{\dagger}$ are then excluded from $M_{system}^{\dagger}$ which contains the answer of the WFS to all the modes generated by the system: $M_{system}^{\dagger} = [S_{TIP}S_{TILT}S_F \cdots S_{nmode}]^{\dagger}$.
S_{nmode} is the slope of the n_{th} mode created by the DM, so we propose to take advantage from the Karhunen-Loëve basis, that transforms the phase into finite orthogonal functions, following this assumption $MM^{\dagger}$ is then given by:

$$MM^{\dagger} = [S_{TIP}S_{TILT}S_F][S_{TIP}S_{TILT}S_F]^{\dagger} \tag{7.16}$$

Figure 7.6 shows the result of this solution, where we project the filtered phase using the solution 3 onto the Karhunen-Loëve basis.

7.2.2 Conclusion

In this section we discussed the indetermination of tip, tilt and the first quadratic mode defocus. We presented that this major problem coming with the LGS AO systems is directly related to the creation of the laser beam in the Sodium layer. Different solutions

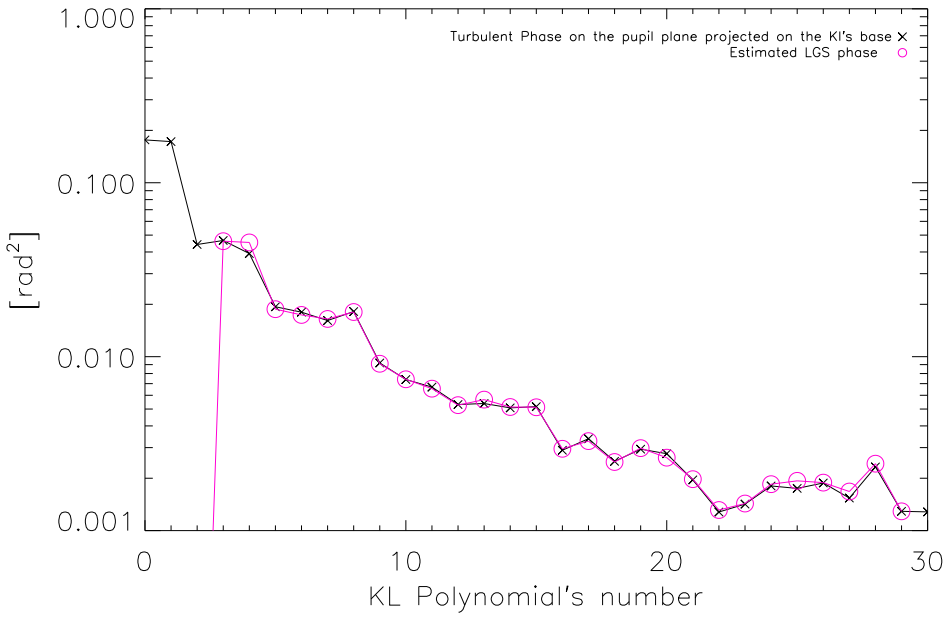


Figure 7.6: Projection of the filtered phase onto the KL basis

and suggestions have been investigated, setting the mean slopes to zero does not filter the total contribution of the TTF. We proposed then the solution 3 for filtering the TTF from the vector data measurements, by finding a transformation matrix to an orthogonal basis that excludes the TTF. We demonstrated that the property of orthogonality of the Zernike modes can not be considered at the WFS basis, so that there is a correlation between the slopes data, and the WFS could have the same answer for different modes. The main idea consists in modifying the model of data to a model that excludes the TTF, we proposed a new model in section [7.9] that is not sensitive to the TTF modes, this latter takes into considerations all the modes generated by the DM while inverting the transformation matrix M.

7.3 Cone Effect issues

One of the most stringent limitation af an AO system for astronomy is the low sky coverage defined as the probability of finding sufficient bright NGSs within the isoplanatic patch of the science target [Rigaut et al. (2000),Hubin and Noethe (1993)]. Laser guide stars techniques is proposed as a quite solution for this problem, making the adaptive optics available for the majority of astronomical observing tasks. However, LGSs suffer from the focal anisoplanatism, where the Laser beacon rays only probe a cone volume above the telescope of finite aperture, leaving behind increasing areas of unmeasured turbulence at higher altitudes. Thus, to overcome this problem multiple LGSs are then

required for a volumic tomography [Beckers (1988)]. This is done by measuring the integrated wavefront through the atmosphere from multiple probes, by using a new sparse projector P_s^{LGS}. This latter adds the contribution of all the LGS footprints through the phase screens that represents the different layers at the pupil of the telescope.
In this section we describe the cone effect problem. We present in section [7.3.2] the new projector module added to the E2E-S for an LGS simulation case, we demonstrate that this projector is no more linear but it is a hyperbolic projector, we show then the simulation parameters for the cone effect in the frame of the MUSE instrument in section [7.3.3].

7.3.1 Description of the problem

Laser guide stars are created within the sodium layer which is at a finite distance above the pupil of the telescope, therefore the wave front distortion emited by the LGS is no more plane like the case of a stellar object, but it is a spherical wave front. Using an artificial GS to estimate the tomographic distortion we suppose that the scientific objet undergoes the same atmospheric turbulence as the GS. Nevertheless, the spherical wave does not cross exactly the same areas of atmospheric distortions as the plane wave front does, in fact, the volume lit by a NGS is a cylinder while the volume lit by the LGS inscribed between the source and the telescope pupil is a cone: this is the focal anisoplanatism or the so-called cone effect.

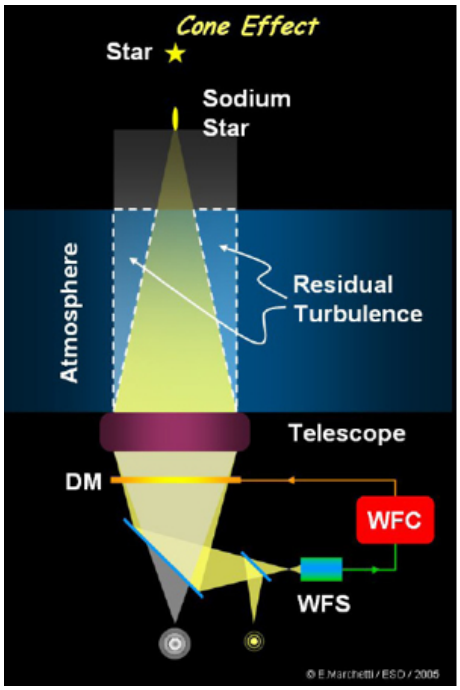


Figure 7.7: Propagation from the Laser spot at a finite distance and from a celestial object. As it is seen the volume lit by the LGS is different from the volume lit by a natural guide star which is represented by a cylinder (Courtesy ESO).

This difference between the spherical and plane wave front distortion is characterized by d_0 representing an aperture diameter-sized quantity that measures the magnitude of the effect of focus anisoplanatism, its given by [Tyler (1994)]:

$$d_0 = \lambda^{6/5} cos^{3/5}(\psi)[\int dh C_n^2(h) F(h/H)]^{-3/5}$$

$F(h/H)$ is a combination of hypergeometric functions. The cone effect illustrated in Figure 7.7 is a major problem for the adaptive optics system using LGS and must be treated carefully and in details.
The error due to the cone effect increases with the telescope diameter D, the more the telescope diameter, the more the cone effect error. Several approaches have been regarded to evaluate the cone effect [Sasiela (1994), Tyler (1994)]. To overcome this effect it is necessary to use several lasers GS in order to cover with the conical beams the whole cylinder of a natural GS. Next section we are going to present this approach and analyze the optimal position of the LGS in the field of view.
In this part we present a new module added to the E2E-S for the LGS simulation case which is presented by a new projector that takes into consideration the LGS footprint in each layer and add all the contributions at the pupil of the telescope. Furthermore, we demonstrate that this projector is no more linear but it is a hyperbolic projector. The simulation parameters for the cone effect in the frame of the MUSE instrument will be introduced in section [7.3.3.1].

7.3.2 LGS hyperbolic projector

The projector module developed in section 5.6.1 is dedicated to the use of natural guide stars as references for tomographic analysis. To overcome the isoplanatic angle limitation, laser probes are then required to be created in the same isoplanatic patch as the scientific object, providing a spherical wave front distortion to be measured and analyzed by the WFS module. As a consequence, a new propagation technique has to be studied and developed for the use of lasers GS.
Scheme 7.8 figures out the representation of the sparse projector, as it is shown the LGS footprint in the turbulent layer decreases while the altitude of the layer increases. For a given turbulent layer at an altitude h, the diameter of the LGS pupil is given by :

$$pup_{LGS} = D_{pix} \frac{H - h}{H} \tag{7.17}$$

where, D_{pix} is the telescope diameter, H is the altitude at which the LGS is created, the sodium layer in our case.

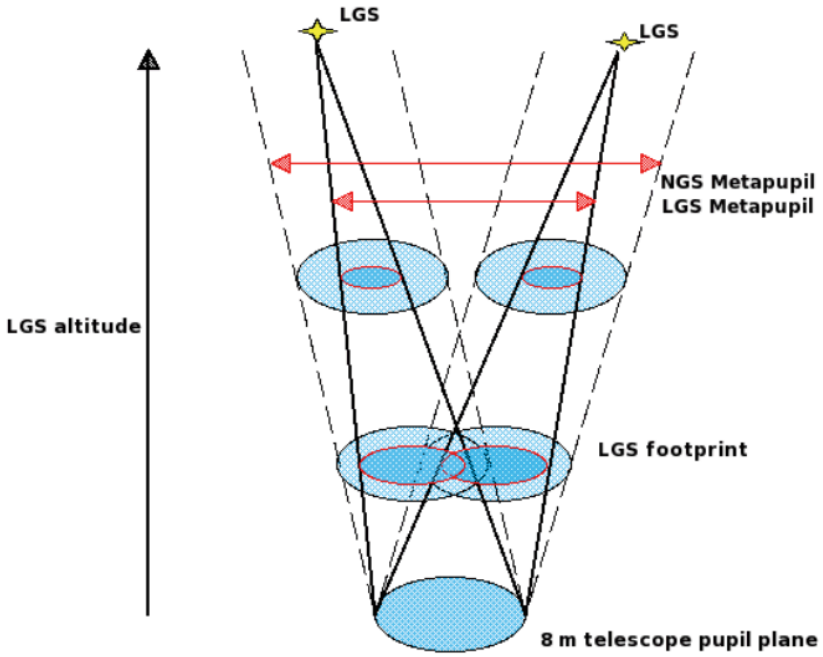


Figure 7.8: Principle of tomography using Laser Guide Star. The covered area of the atmosphere decreases with the layer's altitude. We present the NGS/LGS footprint.

LGS measurements consist in several computational steps that perform operations on two types of grids: atmospheric grid and aperture plane grid. All the grids are supposed to be square.
For the sake of the bilinear interpolation, the atmospheric grid has the same dimensions for all turbulent layers, scaled as *metapupil* grid of the highest altitude. From each grid we care about the LGS footprint squeezed with range according to the cone compression factor $rp_{zoom} = \frac{pup_{LGS}}{D_{pix}}$. Our method consists in adding all the footprint contributions from all the layers at the aperture plane, the same as P_s the natural guide star projector represented in paragraph 5.6.1 which consists in cutting all the NGS footprints in a given sky direction and adding them all at the telescope pupil plane. For the LGS case, one additional point that has to be considered is modifying the atmospheric grids and resizing the mesh size in the ratio of $rp_{expand} = \frac{D_{pix}}{pup_{LGS}}$, so that each LGS footprint pup_{LGS} is uncompressed and sampled as D_{pix} contains only the turbulence information seen by the initial LGS footprint but resampled.
We build for this purpose a sparse operator based on a bilinear interpolation: this operator resizes each atmospheric grid with its relative rp_{expand}, cut the uncompressed LGS footprint, computes wavefront values at the intercepts of rays traced through phase screens to the telescope aperture plane.

Figure 7.9 represents the projector techniques. As it is shown, while we resize the atmospheric grid each LGS footprint moves away from the pupil center of an angular po-

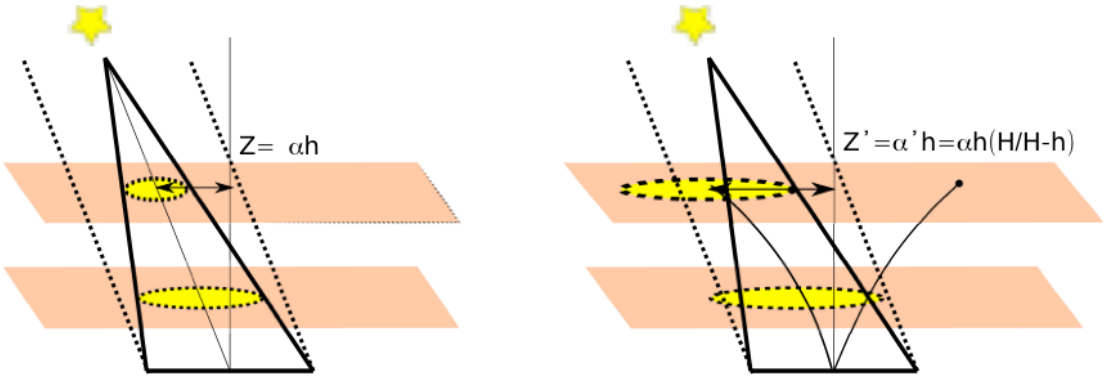


Figure 7.9: Principle of the hyperbolic projector. Each turbulent layer is rescaled to the inverse of the cone compression factor, providing a non linear displacement of the center of each LGS footprint evaluated as $\alpha_{expand} = \alpha \times \frac{H}{H-h}$ relative to each layer altitude.

sition of $\alpha_{expand} = \alpha \times \frac{H}{H-h}$, where α is the angular position of the center of the LGS footprint. The center of the new LGS resizing pupil at a given altitude h is at Z(h) away from the center of the telescope pupil plane:

$$\begin{aligned} Z(h) &= \alpha h \frac{H}{H-h} \\ Z(h) &= -\alpha h - \frac{\alpha H^2}{h-H} \\ Y(h) &= \frac{K}{X} \end{aligned} \tag{7.18}$$

where K = $-\alpha H^2$, X = h-H, $Y = Z + \alpha H$. Equation 7.18 demonstrates that the LGS projector has a hyperbolic form that capture the moved new LGS pupil at $Z(h) = \alpha h \frac{H}{H-h}$, and add all the contributions from the layers of the LGS moved footprint to the aperture plane.
This projector P_{EL} is then build as a rectangular matrix in a sparse format formed by $n_\alpha \times n_l$ blocks, where n_α represents the number of sky analysis directions which correspond to the number of LGSs and n_l is the number of turbulent layers considered for modelling the atmosphere.

7.3.3 Simulation of the cone effect

In this section we care about the reconstruction tomography in terms of the number of LGS. We propose a global study based on the configuration of LGS in the field of view

Altitude of the turbulent layers [m]	205.97	5177.36	13892.3
C_n^2 [%]	0.67	0.265	0.065

Table 7.1: Turbulence parameters of the MUSE simulation case.

to obtain the best performance of an LTAO system. We compare the performance of an LTAO system using LGS and NGS measurements for different configuration of GSs. This study is made in the frame of the instrument MUSE for the VLT. MUSE, the Multi-Unit Spectroscopic Explorer, is an AO-assisted Integral Field Spectrograph, built as a second generation instrument for the VLT [Henault et al. (2003), Bacon et al. (2004),Hubin et al. (2004), Arsenault et al. (2008)]. The two general purposes of this instrument are: large-field characterization of high redshift galaxies and high spatial/spectral resolution spectroscopy of nearby extended objects.
We present in paragraph [7.3.3.1] the simulation parameters of the cone effect, we then describe and analyze the simulation results in paragraph [7.3.3.2], finally we present simulation results of the effective LGS diameter in paragraph [7.3.3.3].

7.3.3.1 Characteristics of the numerical simulation

We present in this part the parameters of the numerical simulation of the cone effect and the different LGS configuration in the FOV. We simulate an 8m VLT telescope in the turbulent conditions given in table 7.1 which is similar to the Paranal's conditions. The atmosphere is represented by three turbulent thin layers. The turbulence strength is of $D/r_0 = 38$ at 633 nm. The telescope pupil plane is represented by 256 pixels.

For the WFS measurements we use sodium guide stars at a fixed altitude of 90km, the only limitation that we consider here is the cone effect, we don't consider the elongation of the WFS spot. We summarize the numerical simulation by the following points

1. Simulation of the turbulence: working on an open loop simulation without considering the temporal aspect, we randomly generate a turbulent phase with a Kolmogorov PSD. The generated turbulent grid have all the same dimensions *dim_alt_px* relative to each position of the LGS in the FOV, and which correspond to the highest *metapupil*. The contribution of LGS footprints are then resampled with the convenient rp_{expand}, added and projected to the pupil plane of the telescope via the P_{LGS} described in paragraph [7.3.2]. The hyperbolic projector is the concatenation of 12 blocks relative to 3 layers $\times$ 4 sky directions.

2. Wave Front Sensor: we suppose that the WFSs are perfect. We don't add for the moment any noise on the measurements. The measurements of the system for a given sky direction α_i is directly the phase results from the contributions of the LGS footprint at the telescope pupil plane.

3. Estimated phase in the layers, volumic reconstruction: the reconstructor used in this simulation is the same presented in section [5.6], based on an iterative resolution of the linear model, the estimated phase at the different layers is given by: $\hat{\Phi}^l = R_{ltao}\Phi^{\alpha}_{pup}$
   Assuming that noise is not correlated between sub-apertures, we can write:

$$R_{ltao} = (P^T_{EL}P_{EL} + \sigma^2\gamma C^{-1}_{\varphi})^{-1}P^T_{EL} \tag{7.19}$$

   For the Kolmogorov turbulence spectrum, the covariance matrix and so its inverse will be none sparse and of full-rank. So to calculate C_{φ} we adopt the approximation proposed by [Ellerbroek (2002)] presented in equation 5.26.
   This approximation was based on the fact that $\frac{-11}{3}\approx$-4 $\Rightarrow k^{(-11/3)}\approx k^{(-4)}$, where k is the radial component of the spatial frequency. The linear model is iteratively resolved using the sparse routine RUOPCG (preconditioned conjugate-gradient solver for a symmetric positive definite sparse linear system with Jaccobi preconditionner) presented in paragraph [5.6.2.4].

4. Imaging system: the DM is conjugated to the pupil plane with 3405 valid actuators, 45% of mechanical coupling. The DM is represented by Gaussian influence functions F_s, actuators at 1 pitch away from the pupil of the telescope are activated for a best DM phase.
   The phase projected at the telescope pupil from the LGS is $\Phi^{\alpha}_{pup} = F_s u$, where u are the voltages to be applied to the mirror in order to generate the DM phase ϕ^{DM}. So an inverse problem has to be solved

$$u = (F^T_s F_s)^{-1}F^T_s\Phi^{\alpha}_{pup}, \tag{7.20}$$

   where $(F^T_s F_s)^{-1}F^T_s$ is the projector of the phase to the DM.
   Using the RUOPCG routine described in table 5.2, we calculate $F^T_s F_s$ to be applied to the voltage unknown to iterate the linear equation: $F^T_s F_s u = F^T_s.\Phi^{\alpha}_{pup}$

Now we present here the RCO matrix relative to the uncompression of the mesh turbulent layers M_{expand} formed by n layer blocks to be applied to the turbulent phase vector $\phi^{L^{tur}_n}$ containing all the values of the wave front through the atmosphere.

$$M_{expand} = \begin{pmatrix} L_1 & \cdots & 0 \\ \vdots & \ddots & \vdots \\ 0 & \cdots & L_n \end{pmatrix} \tag{7.21}$$

The resulted phase from the LGS measurements at the pupil plane is then given by:

$$\Phi^{\alpha}_{pup} = P_{EL} M_{expand} \phi^{L^{tur}_n}$$

$$\begin{pmatrix} \vdots \\ \Phi^{\alpha}_{pup} \\ \vdots \end{pmatrix} = \begin{pmatrix} P^{L_1}_1 & \cdots & P^1_{L_n} \\ \ddots & & \\ \vdots & & \vdots \\ P^{\alpha}_l & \cdots & P^{\alpha}_l \end{pmatrix} \begin{pmatrix} L_1 & \cdots & 0 \\ \vdots & \ddots & \vdots \\ 0 & \cdots & L_n \end{pmatrix} \begin{pmatrix} \vdots \\ \phi^{L_n}_{tur} \\ \vdots \end{pmatrix} \tag{7.22}$$

The aim of this section is to verify the LGS measurements module, so we are going to examine the influence of the cone effect on the performance in terms of the Strehl ratio. To achieve this test study we vary the position of the LGS in a FOV of variable diameters 6" ,10" , 22" ,30", 40" and 60". The direction of interest correspond to the center of the FOV. Then we study the impact of the number of GSs on the AO system performance.

7.3.3.2 MUSE-Case simulation results

The purpose of my PhD is to develop an E2E-S simulator dedicated to the extremely large telescopes and providing a fine simulation for the next generation instrument. To accomplish our objective we need to verify that the LGS modules assemble the expand matrix and the propagation matrix. Hence, we use the simulation parameters of the MUSE case developed in [Costille (2009)].

7.3.3.2.1 Cone effect behavior for an LTAO case In this paragraph we are going to study the performance at the center of the FOV of an LTAO systems using 4 LGS placed on a circle of a variable radius. The considered configuration is presented in figure 7.10. The performance are obtained in terms of the Strehl ratio at the center of each FOV considered. From the simulation results we visualize the optimal configuration of the LGS that gives the highest performance at the center of the FOV. Using 4 LGSs the optimal position is the 22" which correspond to the position where the 4 conical beams cover the whole cylinder of a natural GS. We present for comparison the results obtained for these different cases using NGS.

In figure 7.11 we show the impact of the positions of 4 LGSs placed on a circle of variable radius on the performance obtained at the center of the field for an LTAO case. The NGS case is plot for comparison. This graph highlights the limitations once using LGS as source of measurements: for FOV below 22" the performance is degraded because of the cone effect and above 22" the performance is degraded again because of the anisoplanatism.

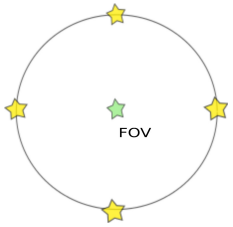


Figure 7.10: 4 LGS configuration case for the MUSE simulation case

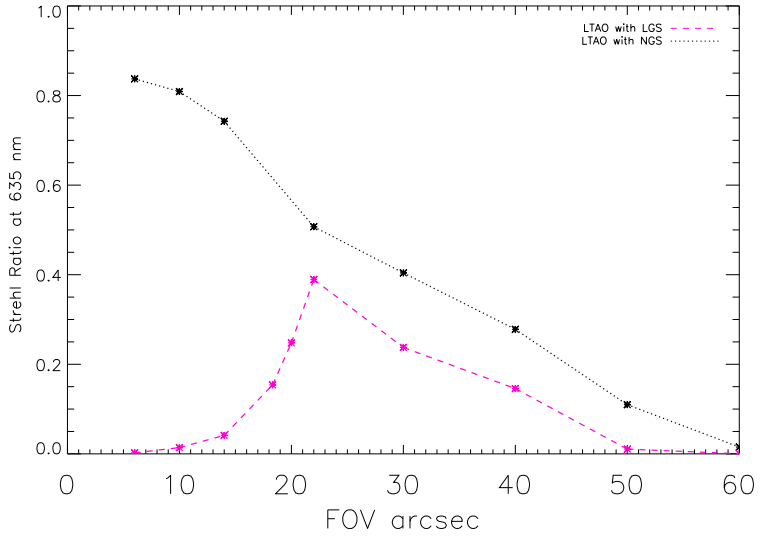


Figure 7.11: Strehl ratio at the center of the field given the measurements from LGS at different positions in the field, for comparison we plot the NGS case measurements. LTAO case is considered.

The optimal position is obtained as observed in the graph once the LGS are placed on a circle of diameter 22" which corresponds to a cylinder of diameter marginally higher than an on-axis pupil cylinder of radius $\frac{D}{H}$ = 18".32, where D is the telescope diameter. For a better explanation we represent in figure 7.12 the case of 4 LGSs placed on a the on-axis pupil cylinder of *radius* = 18".32. The cross section presented shows the metapupil of the LGSs at the highest altitude and shows the unmeasured turbulent zone represented by the unseen region, verifiying that the optimal LGSs position is obtained for a position pretty far from the field center.

7.3.3.2.2 Impact of the number of LGSs on the cone effect Now we analyse the impact of the number of LGSs on the cone effect to correct the cylinder of a natural GS placed at the center of the FOV. Three cases are then considered, we show the performance for 4, 6 and 8 LGSs placed on a circle of a variable diameter: 6", 10" , 22" , 30", 40" and 60". NGS performance is also plotted for comparison (see figure 7.16 , 7.15). We

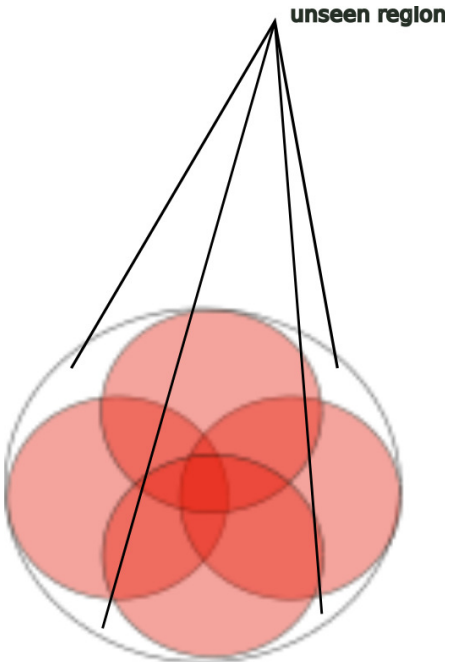


Figure 7.12: Highest LGS *metapupil* given 4 LGSs placed on the on-axis pupil cylinder, the unseen turbulence zone affect the optimal LGSs position

observe for 6 LGSs case's a pretty higher resolution for the cone effect in terms of SR above 22". However, below 22" the attenuation still exists where the volumic turbulence is recover but not completely. In the case of 8 LGSs the performance are thus much more better. We observe that the cone effect is resolved above 22", we are just limited by the anisoplanatism error which is very well decreased since the volumic turbulence is more recovered. The cone effect is then reduced with the number of LGSs, more the number of LGSs is considered higher the performance is, and the anisoplanatism error is reduced.
In figure 7.17 we observe a degradation of the performance for the three configuration while the LGSs are placed inside the NGS cylinder because of the cone effect. For the FOV higher than 22" the cone effect is slightly better with 6 Laser GSs case's, and is resolved while using the 8 Laser GSs.

7.3.3.3 Effective diameter of Laser Guide Star

The mean square residual wave front distortion E^2, which results when the turbulence-induced wave front distortion associated with a spherical wave $\phi_s(r)$ is used as an estimate of the turbulence-induced wave-front distortion associated with plane wave $\phi(r)$ is given by:

$$E^2 = \int drW(r/R) < [\phi(r) - \phi_s(r)]^2 > / \int drW(r/R) \tag{7.23}$$

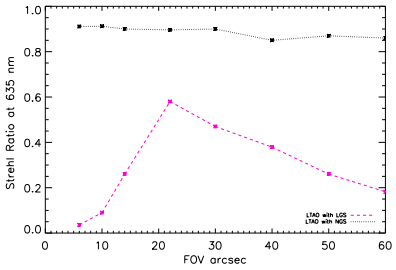


Figure 7.13: Strehl ratio at the center of the field of view for 6 guide stars placed on a circle of variable diameter, NGS performance is plotted for comparison

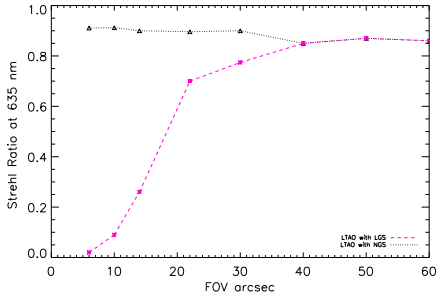


Figure 7.14: Strehl ratio at the center of the field of view for 8 guide stars placed on a circle of variable diameter

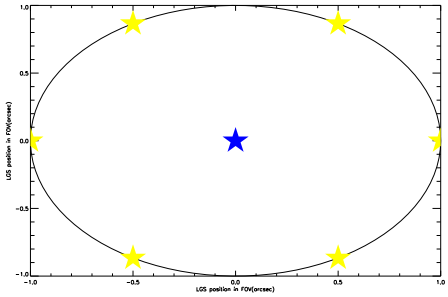


Figure 7.15: 6 LGS configuration in the FOV for the LTAO performance study at the center of the field

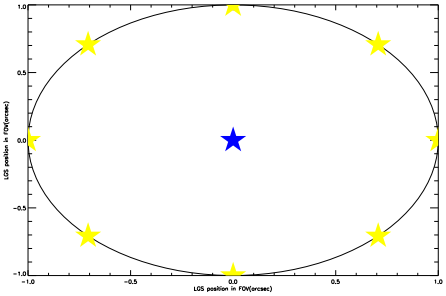


Figure 7.16: 8 LGS configuration in the FOV for the LTAO performance study at the center of the field.

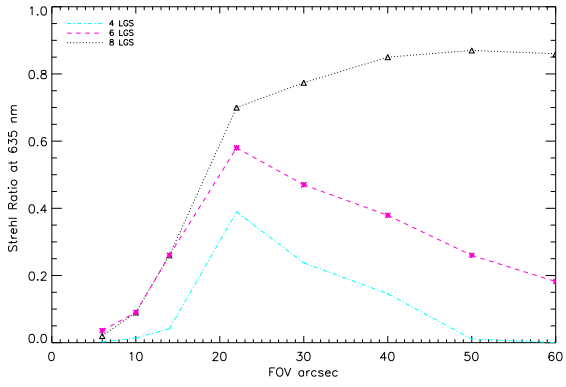


Figure 7.17: LGS performance at the center of the FOV, using 4, 6 and 8 LGSs as measurement sources, for a different configuration of Laser GSs in the field-of-view.

where R is the telescope radius, W(r/R) is the pupil function equal to 1 if r < R, and zero otherwise. $\phi(r)$ and $\phi_s(r)$ are the plane and spherical wave front distortion respectively. The angle brackets denotes an ensemble average with respect to the turbulence statistics. Tyler found in [Tyler (1994)] that E^2can be estimated for 1 LGS as following :

$$E^2 = (D/d_0)^{5/3} \tag{7.24}$$

d_0 is an aperture diameter-sized quantity that measures the magnitude of the effect of focus anisoplanatism, the value of d_0 depends on the vertical distribution of the optical strength of turbulence, the optical wavelength at which the imaging system is operating, the zenith angle and the backscatter altitude. Its given by

$$d_0 = \lambda^{6/5} cos^{3/5}(\psi)[\int dh C_n^2(h) F(h/H)]^{-3/5} \tag{7.25}$$

where $F(h/H)$ is a combination of hypergeometric functions of the LGS altitude and the turbulent layer altitude, D is the telescope diameter, ψ the zenithal angle of the LGS.

7.3.3.4 Calculus and validation of the focal anisoplanatism

In this paragraph we propose to calculate the error resulting when the spherical wave front distortion is used as an estimate of the plane wave and to compare the numerical results to the analytical obtained with equation 7.24, as a function of the variation of the wavelenght and then by variating the LGS altitudes.

7.3.3.4.1 Variation of the LGS altitude We present in this paragraph a comparison between numerical and analytical results for the cone effect error in function of the LGS altitude. We generate randomly 1500 phase screens with a Kolmogorov PSD, 8m telescope is considered represented by 256 pixels at the pupil plane, the strenght of the turbulence corresponds to $D/r0 = 67.5$ at 500 nm, one turbulent layer is simulated at 13792m. We consider different altitude of the Laser source, and we calculate the mean square residual error wave front distortion given the analytical expression and the simulation results. Figure 7.18 shows the impact of the LGS altitude on an AO system performance using an LGS as source of measurements.

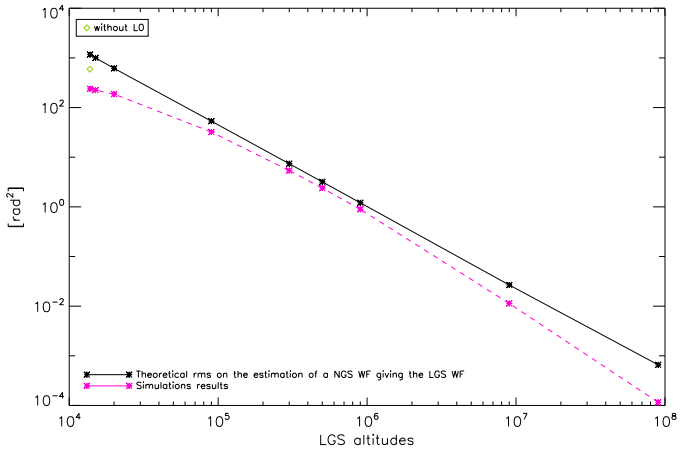


Figure 7.18: Analytical and numerical comparison using Tyler equation and the E2E-S, one layer is simulated with D/r0=67.5 at 500nm.

Altitude of the turbulent layer's [m]	2500	10000
C_n^2 [%]	0.7	0.3

Table 7.2: Turbulence parameters

7.3.3.4.2 Variation of the wavelength We propose here to compare the analytical value to the simulation results obtained as a function of the wavelength, then we show the impact of the number of LGS in limiting the focal anisoplanatism error.
We simulate an 8m VLT telescope represented by 256 pixels in the turbulent conditions given in table 7.2, 1500 phase screens are generated randomly using the *turbulence generator* module of the E2E-S.

1 Laser Guide Star: In figure 7.19 one LGS is considered as spherical source measurements. Good seeing (r_0 = 0.25m) and median seeing (r_0 = 0.16m) conditions are then presented. The numerical simulation gives reasonnable estimation of the error variance. It is important to note that the cone effect is too strong under median seeing, therefore, visible wavelength are not reachable on an 8 meter telescope using classical AO system and 1 LGS. Some results are given in table 7.3 for comparison.

Wavelength [nm]	500	800	1000	1650
Theor d_0[m]	3.85	6.43	8.56	15.96
Simu d_0[m]	3.88	6.82	8.92	16.26

Table 7.3: Theoretical and numerical comparison of the cone effect using 1 LGS, 8 meter telescope is simulated under good seeing (r_0 = 0.25m).

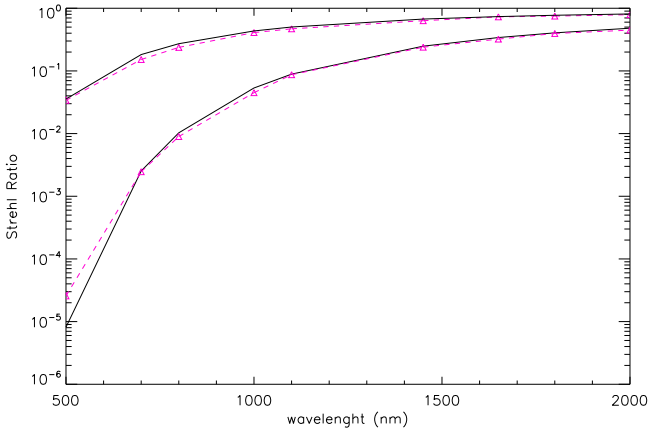


Figure 7.19: SR performance obtained at different wavelength under a good seeing (upper line) and median seeing conditions, compared to the theoretical one obtained with the analytical formula of Tyler.

4 Laser Guide Stars: In order to achieve the limitation of the cone effect, multi-LGSs must be investigated, here we present the gain obtained once using 4 LGSs compared with 1 LGS. First of all, it is important to place the 4LGSs on the circle providing the optimal performance, as it was shown in 7.3.3.2.1, the sources must be on a circle of diameter 22".
In figure 7.20 we plot the SR obtained with 4 LGS under good seeing conditions, the 1 LGS case in presented for comparison. The residual variance with 4 LGS is 7 times smaller than with one LGS. The cone effect is slightly resolved with 4LGS in the visible and under good seeing conditions where the SR increase to 0.62 instead of 0.034 using 1 Laser GS.

7.3.4 Conclusion

In this section we presented the E2E-S LGS projector block P_{EL}, a sparse operator that computes wavefront values at the intercept of rays traced through phase screens to the pupil plane of the telescope. We demonstrated that this LGS projector is hyperbolic, allowing the expand of the LGS mesh size with range according to the cone compression factor. In order to validate this projector we showed some simulation results for a MUSE-like case and we show the cone effect on the performance at the center of the FOV for different positions of the Laser GSs on a circle of a variable diameter. For a better performance of an LTAO system, Laser GSs must be placed on a circle of a 22" diameter and above. Of course using NGSs as a source of measurements allows much higher performance even above 22", because of the focal anisoplanatism, so that the residual error is much higher for the LGS case since the volumic turbulence is less recovered. We calculated the cone effect and we compared the results with the analytical formula.

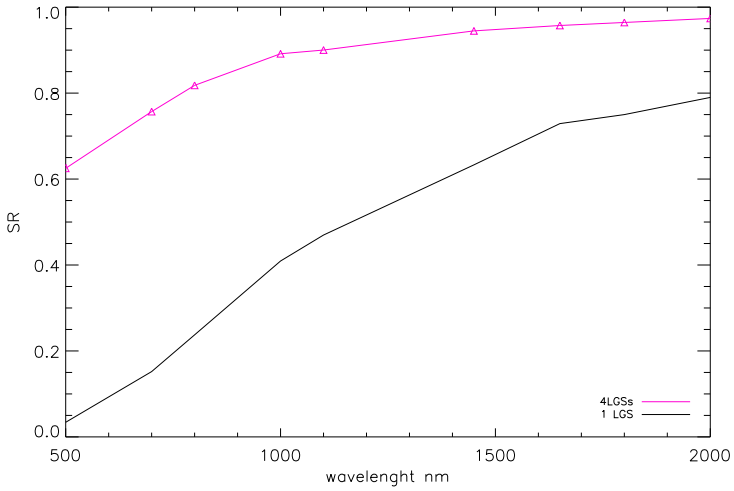


Figure 7.20: SR performance evaluated in functions of the wavelength, one LGS is considered as source of measurements compared to 4 LGSs (upper line), where the cone effect is limited.

Chapter 8

Merging Natural and Laser Guide Stars Data

Contents

7.1 Introduction 97

7.1.1 Outline of problems 97

7.1.2 Types of LGS 98

7.1.2.1 Sodium resonance 99

7.1.2.2 Rayleigh scattering 99

7.2 *Tip, Tilt and Defocus* Indetermination 100

7.2.1 Investigation methods for *tip, tilt and defocus* modes filtering . . 100

7.2.1.1 First solution: Substraction of average slopes 103

7.2.1.2 Second solution: M contains the WFS answer to the *tip and tilt and defocus* 104

7.2.1.3 Third solution: M contains the WFS answer to all the modes generated by the system 106

7.2.2 Conclusion 106

7.3 Cone Effect issues 107

7.3.1 Description of the problem 108

7.3.2 LGS hyperbolic projector 109

7.3.3 Simulation of the cone effect 111

7.3.3.1 Characteristics of the numerical simulation 112

7.3.3.2 MUSE-Case simulation results 114

7.3.3.2.1 Cone effect behavior for an LTAO case . . . 114

7.3.3.2.2 Impact of the number of LGSs on the cone effect 115

7.3.3.3 Effective diameter of Laser Guide Star 116

7.3.3.4 Calculus and validation of the focal anisoplanatism . 118

7.3.3.4.1 Variation of the LGS altitude 118
7.3.3.4.2 Variation of the wavelength 119
7.3.4 Conclusion 120

AO systems suffer from the limited availability of sufficient and bright NGS. However, current and next generation telescopes incorporate LGS AO systems to increase the very limited sky coverage [Wizinowich et al. (2006),Neichel et al. (2010), Diolaiti et al. (2008)]. These latter have two major inherent difficulties: focal anisoplanatism and tilt indetermination. In the previous section we show that multi LGS can be used to overcome the cone effect, In this paragraph we care about the tilt indetermination and Tilt Anisoplanatism (TA). Tip/tilt modes cannot be exactly known by the LGS measurements because of the uncertainty of the source positions. Therefore, Low Order natural guide stars (LO-NGS) wavefront sensors are needed to obtain the global motion of the LGS. Moreover multiple high order LGS tomography (multi-HO-LGS) looses all information about the quadratic modes (one focus and two astigmatisms) [Flicker and Rigaut (2002)]. In this dissertation we limit our study to the TTF indetermination . This chapter is dedicated to the Laser tomography system where the estimation is performed from the fusion data HO LGS measurements and the LO NGS measurements. Therefore, we recall to the filtering concepts proposed in the previous chapter to excludes the TTF modes from the vector data of the LGS measurements. Integrated and split tomography are proposed [Gilles and Ellerbroek (2010)] as two solutions for the volumic reconstruction given the HO/LO data. We investigate both method performance in terms of the residual error evaluated at the center of the FOV. The simulation parameters are presented in paragraph [8.2.1]. Results are evaluated in paragraph [8.2.2]. We then investigate the integrated tomography in paragraph 8.2.

8.1 Split Tomography

Proposed in [Wizinowich et al. (2006)], generalized by [*L.Gilles and L. Elerbroek 2008*], split tomography illustrated in figure 8.1, consists in separating the LGS, NGS control loops driven independently by the LGS, NGS measurements. The latter control loop uses the noise-weighted least square reconstructor to estimate the LO tip, tilt and TA, the former control loop is driven by an iterative resolution of the minimum variance estimator applied to the LGS measurements. Only the LGS participates to the volume reconstruction, the TT and TA are then projected to the output of the DM fitting step. This architecture has been generalized for the MCAO case [Gilles and Ellerbroek (2010)], where the TT and TA estimated modes are applied to the conjugated DM at different altitudes.
Split tomography is knows as the optimal solution in terms of the computational complexity and loads. The tomography reconstructor is reduced to the LGS tomography. The NGS does not participate in the resolution of the iterative methods allowing less iterations and complexity at the RTC level.

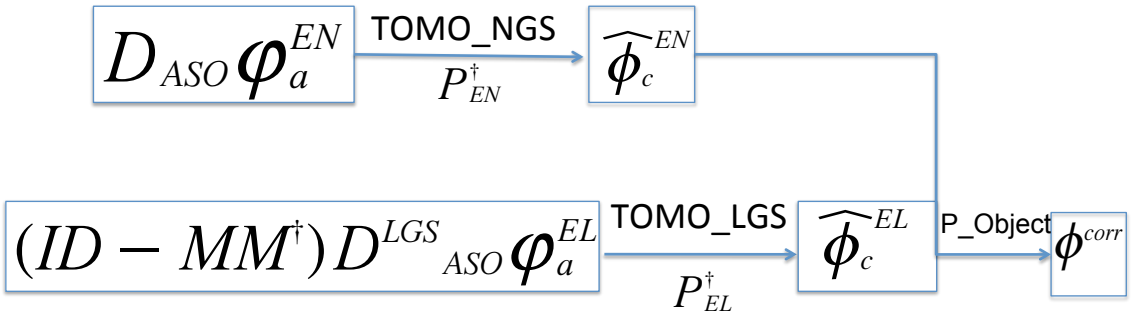


Figure 8.1: Split tomography architecture

8.2 Integrated Tomography

In this paragraph we present the integrated tomography, all the NGS and the LGS participate in the reconstruction step. We estimate the phase at the pupil plane from the LO vector slopes measured by NGS-WFSs, and from the HO vector slopes measured by the LGS-WFSs. Both estimated phases are then concatenated in a simple vector Φ^{α}_{LO-HO}, α is the LGS and NGS sky directions. The measured WFS vector Φ^{α}_{LO-HO} at the pupil plane, is applied to the *TOMO* block to reconstruct the whole volumic atmosphere. The integrated architecture tomography is illustrated in figure 8.2.

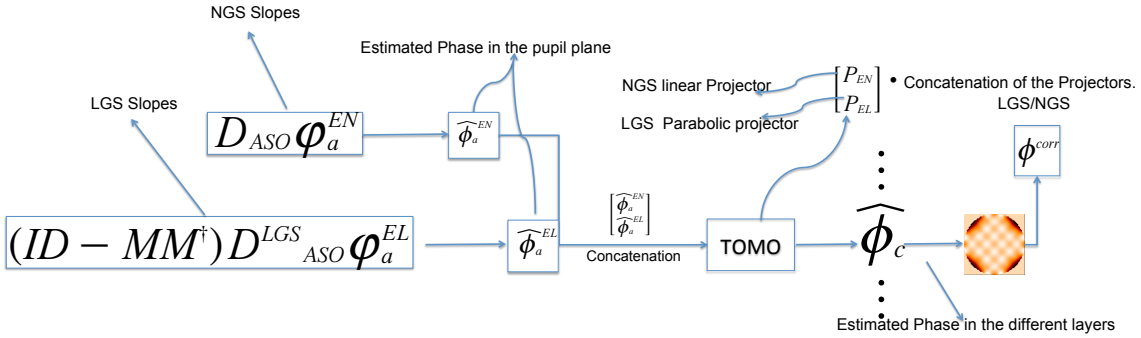


Figure 8.2: Integrated tomography architecture. The TOMO block is built given the concatenation of both hyperbola-LGS and linear-NGS projectors.

8.2.1 Characteristics of the numerical simulation

We present in this part the parameters of the numerical simulation for the fusion data HO/LO given the LGS/NGS WFS measurements. We simulate an 8 m VLT telescope. The atmosphere is represented by one turbulent thin layer. The turbulence strength is of $D/r_0 = 14$ at 633 nm. The telescope pupil plane is represented by 256 pixels.
For the LGS WFS measurements we use the sodium guide stars at a fixed altitude of 90 km, the only limitation that we consider here are the cone effect and the TTF indetermination, we don't consider the elongation of the WFS spot. We summarize the numerical

simulation by the following points

1. Simulation of the LGS/NGS phase screens: working on an open loop simulation without considering the temporal aspect, we randomly generate a turbulent phase with a Kolmogorov DSP. The generated turbulent grid have all the same dimension *dim_alt_px* relative to the largest FOV. The contribution of HO-LGSs footprints are resampled with the convenient rp_{expand} presented in section 7.3.3.1 , added and projected to the pupil plane of the telescope via the sparse hyperbolic projector P_{LGS} described in paragraph 7.3.2. The LO-NGS contributions are projected using the sparse linear NGS projector presented in section 5.6.1. The LGS and NGS projectors are then concatenated in one block to estimate the atmosphere.

2. Wave Front Sensor: we consider a realistic geometry Model of SH-WFS presented in paragraph 5.5.3.2, the full and partial illuminated subapertures are then treated. 64×64 subapertures are considered, with 3212 subapertures are fully and partially illuminated. We don't add for the moment any noise on the measurements.

3. Imaging system: the DM is conjugated to the pupil plane with 3405 valid actuators and 45% of mechanical coupling. Represented by the Gaussian IF F_s, actuators at 1 pitch away from the pupil of the telescope are activated for a best fitting DM phase. The direct model presented in equation 7.3, allows us to find the voltages to be applied to the DM. Thus, the estimated phase $\hat{\varphi}_{HO/LO}$ given the slopes measurements is given by:

$$\hat{\varphi}_{LO} = F_s u_{LO} \hat{\varphi}_{HO} = F_s u_{HO} \tag{8.1}$$

So that Φ^{α}_{LO-HO} is a simple vector given by:

$$\Phi^{\alpha}_{LO-HO} = \begin{bmatrix} \hat{\varphi}_{LO} \\ \hat{\varphi}_{HO} \end{bmatrix} \tag{8.2}$$

4. Tomography:

   - Integrated tomography: we consider two test cases: fusion data given the HO/LO spherical distortion. And fusion data given HO spherical distortion and LO plane distortion measurements. The estimated vector phase in the first case is the concatenation of the measuring HO/LO phase of the spherical wavefront distortions. The latter consists in concatenating in a unique vector the estimated phase given the NGS-LO and the LGS-HO. In both cases we are going to use the new concept proposed in paragraph [7.2.1.2], to separate the slopes space into orthogonal and parallel to the LO modes. From equation 7.9

and using the properties of KL basis we calculate the transformation matrix M to the orthogonal space that excludes the TTF modes. In this study case, $M^{\dagger}$ contains the answer of the WFS to the 3405 modes generated by the DM.
We concatenate the projectors used to estimate the phase vector in one block, and based on a iterative resolution of the linear model, the estimated phase at the different layers is given by: $\hat{\Phi}^{l} = R_{ltao}\Phi^{\alpha}_{LO-HO}$ Assuming that the noise is not correlated between sub-apertur, we can write:

$$R_{ltao} = (P^T P + \sigma^2 \gamma C_{\varphi}^{-1})^{-1} P^T \tag{8.3}$$

Where P is the concatenation of two projectors.

$$P = \begin{bmatrix} P_{LO} \\ P_{HO} \end{bmatrix} \tag{8.4}$$

The linear model is iteratively resolved using the sparse routine RUOPCG solver for a symmetric positive definite sparse linear system with Jaccobi preconditionner presented in paragraph 5.6.2.4.

- Split tomography: In a seperate control loop, we estimate the atmosphere from the LGS and NGS measurements separately. The control loops are managed one by one to estimate the whole volume. This method does not consider correlations between HO and LO modes.

8.2.2 Results and Conclusion

8.2.2.1 Fusion data: HO/LO Spherical distortion

We analyse the split and integrated tomography given the HO and the LO spherical distortion measurements. Two LGSs are considered. Placed on a circle of a variable diameter as depicted in figure 8.3.

The performance for both methods is obtained at the center of the FOV in terms of the mean square residual wave front error, calculated from the spherical estimated wave front distortion to estimate the plane wave front distortion. Figure 8.4 represents the comparison simulation test for split and integrated tomography.

Integrated tomography achieves a slightly better performance than the split tomography, in terms of the mean square residual error on the tomographic reconstruction. The graph illustrate this difference between both reconstructor. This is caused by the lost of informations on the LGS/NGS correlation wave fronts. A focus mode for example, at a given altitude is recognized by the WFS as a TT for a given sky direction, so that if we

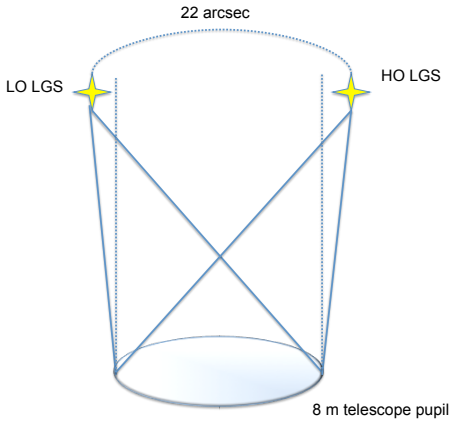


Figure 8.3: Sketch of two LGSs placed on a cercle of 22 arcsec.

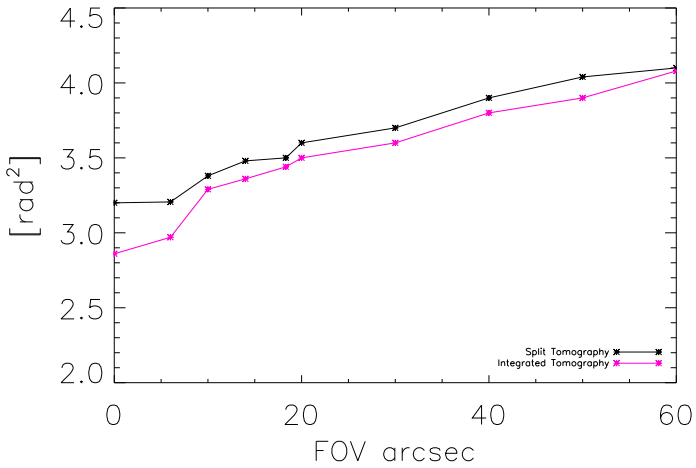


Figure 8.4: Mean square residual error, obtained at the center of the FOV for split and integrated methods.

measure the TT from an LGS at another sky direction we lost the right information on the TT coming from the defocus at the altitude. This method does not provide correlations between LGS/NGS modes, we lost informations on the HO modes coming from the contributions of the layers at the altitudes.
More the number of NGS is, more the split tomography becomes advantageous in terms of reconstruction. The high orders losted while seperating the LGS / NGS loop in the split tomography, is covered and reconstructed by the multi-NGS. Unfortunately this is not allways accessible to find enough NGSs in the same isoplanatic patch as the science target.
However, integrated tomography faces computational bottlenecks in the dealing with the very large concatenated reconstruction matrix. So that, split tomography allows a separate calculus of the linear and hyperbolic reconstructors, allowing less computational complexity and loads at the RTC level. Therefore, if we are dealing with a small num-

ber of LGS where the calculus loads is quite acceptable, integrated tomography could provide better performances. But, using a large number of GSs, split tomography is the best option for the reconstruction tomography in terms of the reconstruction time and the computationl loads.

From the analytical formula [equation 7.24], we find the mean square residual wave front error at the center of the FOV $E^2 = 2.17rd^2$, and the effective diameter of the LGS is $d_0 = 5.01m$. Figure 8.5 represents the projection on the KL basis of the reconstructed phase given the HO spherical distortion in green, and the reconstructed phase given the LO LGS mesurements in pink, black plot represents the fusion data HO/LO laser guide stars, it's very important to show that we are capable to reconstruct the whole phase consisting from the tip, tilt and defocus as LO and the phase excluded from these latter as HO. Moreover, from the reconstructed HO phase we show the efficiency of the method proposed in paragraph [7.2].

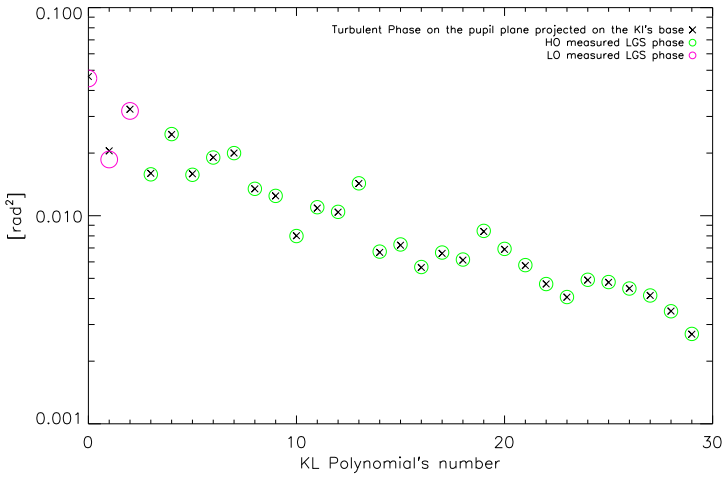


Figure 8.5: Reconstruction given the HO LGS measurements and the LO LGS measurements

8.2.2.2 Calculus of the focal anisoplanatism using the fusion data

In figure 8.6 one laser guide star is considered as a spherical source, we measure the HO and the LO separately, we concatenate both, and we reconstruct the phase using the fusion data block proposed above. Good seeing (r_0= 0.25m) condition is presented. The numerical simulation gives reasonable estimation of the error variance. Thus, this simulation can be compared with the case simulated in paragraph [7.3.3.4.2], where we estimate the phase given the whole spherical distortion.

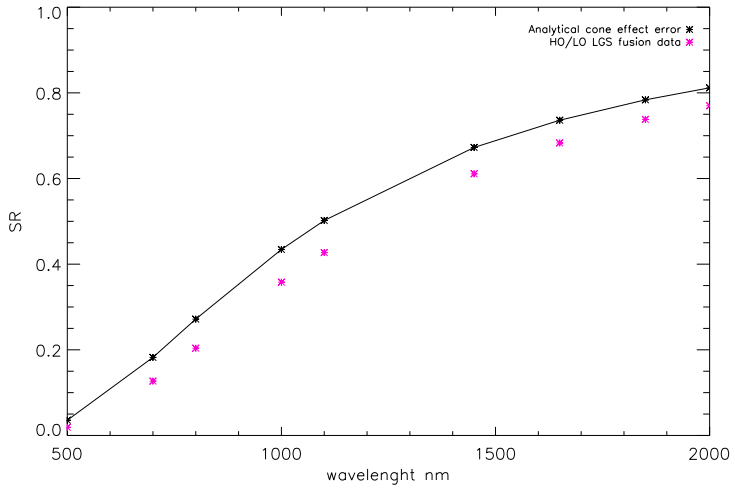


Figure 8.6: SR performance obtained at different wave length under a good seeing (upper line) compared to the theoretical one obtained with the analytical formula of Tyler using the fusion data HO/LO spherical distortion.

8.3 Conclusion

We presented in this part the fusion data HO-LGS and LO-NGS, using the integrated and the split tomography. The LGS data are treated as proposed in paragraph [7.2] the slopes are modified by aplying the transformation matrix M presented in paragraph [7.2.1.2], so that we obtained the slopes out of tip, tilt and defocus. This filtered vector data provide then the HO LGS wavefront distortion. In the other hand, given the set of measuremens of the NGS, we estimate the phase measured by the WFS. The split and the integrated tomography are then applied to reconstruct the whole atmosphere, we found a slightly better performance while using the integrated tomography, in terms of the mean square residual error at the center of the FOV. However, the split tomography presents an efficiency in the computational load. Using 4 HO-LGS and 3 LO-NG in the same conditions presented in section [8.2.1], split tomography is 7 times faster then the integrated tomography.

Chapter 9

Simulation of an E-ELT instrument: EAGLE

Contents

8.1 Split Tomography 124

8.2 Integrated Tomography 125

8.2.1 Characteristics of the numerical simulation 125

8.2.2 Results and Conclusion 127

8.2.2.1 Fusion data: HO/LO Spherical distortion 127

8.2.2.2 Calculus of the focal anisoplanatism using the fusion data 129

8.3 Conclusion 130

The study of the evolution of high-redshift galaxies, tracking down earth-like planets, stars, detection and characterisation of first-light galaxies and also stellar archeology [Evans et al. (2010b), Puech et al. (2010)], probing the nature of dark matter and dark energy [McCarthy (2006)]. All these sciences areas will be tackled with the new generation of telescopes. The European Extremely Large Telescope E-ELT is being built by the European Southern Observatory. Eight instrument conceptual studies (phase A) have been launched. ELT Adaptive Optics for Galaxy Evolution [Cuby et al. (2009)], a near IR multi object spectrograph with deployable Integral Field Units (IFUs).
This part is dedicated to the numerical simulation of the EAGLE instrument, two cases are then presented an EAGLE-like case and a full EAGLE E2E-S case. We present the EAGLE instrument science cases and the required AO system in section [9.1] . In paragraph [9.2] we describe the E2E-S simulation. We start an EAGLE-like simulation with a 42m telescope using 11 NGS in a wide field of view 7.5 arcmin. We considered 9 turbulent thin layers and 83×83 sub-apertures per WFSs. We then present the full EAGLE case simulation using the LGS module, so that 6 LGSs placed on a circle of 7.5 arcmin of diameter 83×83 sub-apertures per WFSs , and 5 LGSs is required inside the field of view with 64×64 sub-apertures per WFSs. For both cases pure open loop is considered, M_4 is not considered in this dissertation.

9.1 Description of the EAGLE Instrument

EAGLE is a French-UK partnership Phase A study of a multi-Integral Fiel Unit(IFU) for the E-ELT, operating at near-infrared (NIR) wavelenghts. This type of instrument is common to all ELT projects assisted with a high-order AO system in order to improve spatial resolution and taking advantage of the large FOV. The EAGLE instrument is required to achieve many scientific objectives such as study the physics of high red shift galaxies, detect and characterize the first-light galaxies at high redshifts, understand the properties of the distant galaxies, resolve stellar content dynamics and mass function. EAGLE science concepts has been developped to tackle all these requirements. An overview of the principal EAGLE science cases can be found in [Evans et al. (2010a),Cuby et al. (2009)]. The aim of EAGLE is to reach near-IR spectroscopy of a large numbers of objects across a wide field of view of diameter > 5' to build-up representative and unbiased samples of, for example, hundreds of high-redshift galaxies. Its science case calls for spatial resolution of 75mas with respect to the seeing, no requirements to improve diffraction-limited performance. The major performance of EAGLE is the Ensquared Energy (EE) which set to be at least 30% EE in a square element of $75 \times 75 mas^2$ in H band ($1.6 \mu m$). The wavelenght coverage extends from 0.8 to 2.4 μm. The science (IFU) sub-field is set to 1.65" × 1.65". EAGLE will employ multi-object adaptive optics (MOAO), to provide significantly improved image quality for selected target fields within the focal plane with one DM in each IFU optical train. There is no need for a full correction of the entire FOV but rather only correction of the turbulence in the specific direction of the target in a small IFU sub-field of 1.65" × 1.65" see figure (9.1) . Nevertheless, the science targets are too faint, so that the correction to be applied on the DM is then computed from a set of guide stars distributed if the whole FOV.

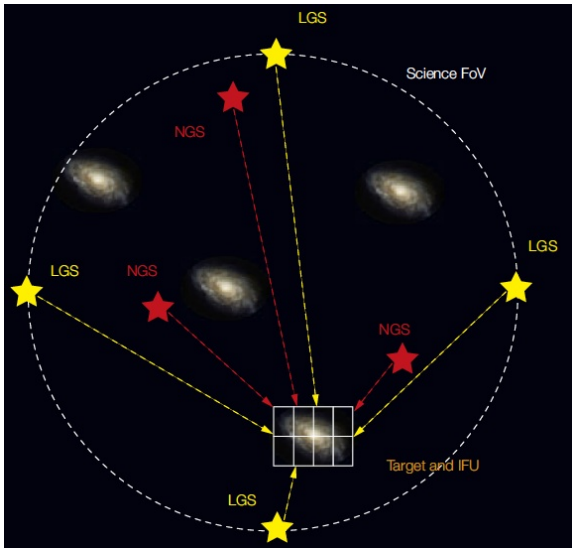


Figure 9.1: MOAO configuration using a combination of LGS and NGS to map the atmospheric turbulence. One DM is dedicated to each IFU.

The whole FOV turbulence is estimated using the LGS and NGS WFS measurements. The correction needed at a given position in the small field of view is then derived by a

simple projection and is performed by a local science DM controlled in open loop providing high correction quality. In addition EAGLE instrument takes advantages from E-ELT concepts by controlling in closed loop two mirrors associated to the telescope: M_4 and M_5. There is therefore a mixed open and closed loop multiobject adaptive optics (MOAO) system. The reconstructed wavefront is then applied to the in-telescope DM M_4 operating in closed loop (which all of the wavefront sensors will see) to correct for the low-order wavefront error terms and the science field DM correct the high-order terms of its associated science field. LO modes such as tip, tilt and defocus, have a little impact on the EAGLE performance in terms of the EE, so in order to improve a significant performance high order aberrations have to be corrected, requiring HO DM and sufficient reconstruction.

To achieve the EAGLE needs, 6 LGSs for tomography placed on a circle of 7.5 arcmin of diameter shall be implemented. The HO WFS of 84×84 sub-apertures per WFS will be completed by a set of NGS WFS.
Up to 6 NGS WFS of 64×64 is then required to be placed incide the FOV. The number of NGS was analysed in terms of the sky coverage, so that for a randomly selected sub-field there is 80% chance to find five or more NGS with magnitude R < 17 inside an FOV of 7 arcmin of diameter. The volumic turbulence is represented by 9 layers between 0 and 16.5 km.
In this part we present two E2E-S EAGLE simulations. In paragraph 9.2 we present a simulation of an EAGLE-like instrument using only natural guide stars, performance is analysed in terms of SR .

9.2 EAGLE-like simulations

In this section we describe the EAGLE-like simulation, we present the characteristics of the E2E-S simulation and the results obtained for different targets in a 7.5 arcmin FOV.

9.2.1 Description and characterisation of the E2E-S EAGLE-like simulation

We simulate a 42m ELT telescope without segmentation and zero occultation. We don't consider any dynamic error.

1. **Turbulence parameters**:
   - seeing = 1" @ 0.5 nm
   - L_0 = 25 m
   - Turbulence conditions are given in table 9.1:
2. **Systems of correction** One micro-DM of 84×84 sub-apertures per science target directions, 14 correction directions randomly distributed in the FOV of 7.5 arcmin.

Layer's number	1	2	3	4	5	6	7	8	9
Altitude of the turbulent layer's [m]	47	140	281	562	1125	2250	4500	9000	18000
C_n^2 [%]	53.6	2.5	4.3	11.3	9.6	2.9	5.8	4.2	5.8
Velocity speed [m/s]	15	13	13	9	9	15	25	40	21

Table 9.1: Turbulence parameters of the EAGLE-like simulation case.

All the micro-DM are conjugated to the pupil plane, we don't consider any displacement. The temporal frequency response > 2000 Hz and the stroke is supposed to be infinite.

3. **System of measurement** 6 LGS focalized at infinity, distributed on a circle of 7.5 arcmin of diameter as illustrated in figure 9.2. 4 NGSs distributed inside the FOV. Each sky direction is analysed by a WFS of 84×84 sub-apertures at 589 nm.

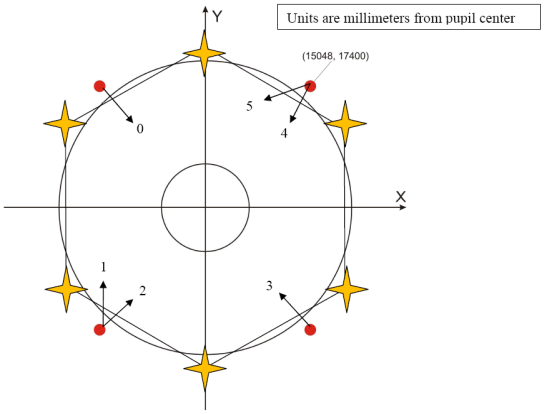


Figure 9.2: EAGLE simplified edge launching geometry. 6 LGSs launched from 4 launching telescopes located 2m outside the pupil.

4. **RTC and control loop** The controlled system is in open loop, we use the sparse reconstructor proposed in section [5.6] to reconstruct the whole volume in the 7.5 arcmin FOV. There is no fusion data LGS/NGS.

9.2.2 EAGLE-like Results and conclusion

The simulation ran for 4 days over 3500 iterations. The turbulent phase is projected using the linear sparse projector, to the WFSs from the ten sky directions. The LGS and NGS are treated equally, so we have the same projector for both GSs. The RTC receives pixel data from the ten GSs (LGSs and NGSs) WFSs. Using the sparse reconstructor we reconstruct the turbulence volume as well as the vector for each science field direction which has to be corrected by the science DM.
All the matrices have to be calculated in the calibration part such as the sparse linear projector of $[10 \times 9 \times 964^4]$ dimension, the phase covariance matrix and the very load

reconstructor matrix. This latter tooks about 1 month of calculation.

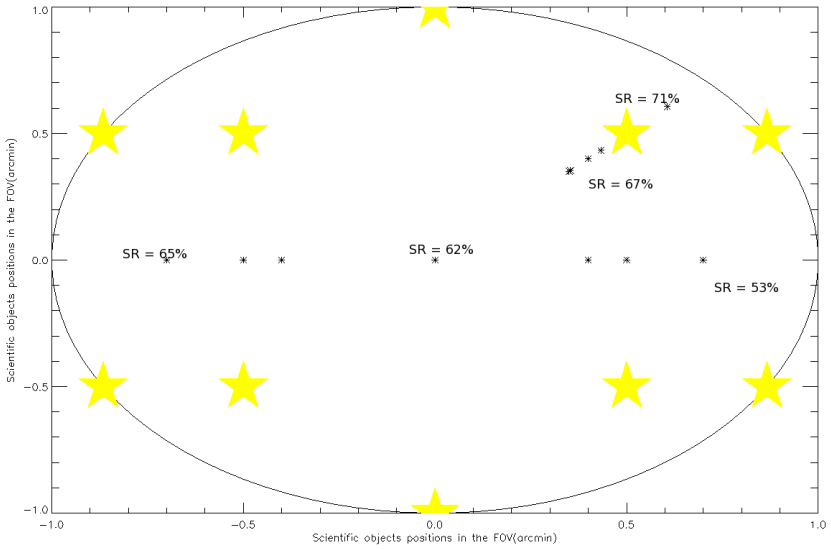


Figure 9.3: SR EAGLE-like simulation, calculated at 5 sky directions inside the 7.5 arcmin FOV. The correction is done by a DM conjugated to the pupil plane. We show the ten GSs used as source of measurements in yellow, and in dark the 14 scientific targets.

We limit our study performance to the SR presented in figure 9.3. The PSF of the residual error for one direction is also presented in figure 9.4. The performances are analysed over 3500 iterations for the 14 sky directions of correction.
Assuming a bright guide stars conditions and no temporal error, the error budget for the EAGLE-like simulation can be approximated to

$$\sigma^2_{res} \simeq \sigma^2_{scint} + \sigma^2_{tomo} + \sigma^2_{alias} + \sigma^2_{fit} + \sigma^2_{calib} \tag{9.1}$$

Where σ^2_{tomo} is the error due to the reconstruction of the atmosphere represented by 9 layers. σ^2_{calib} corresponds to the set of errors related to the interaction matrix and the implementation of the control law. σ^2_{scint} is the cause of the variation of the wave front amplitude in the telescope pupil plane received from the star. $\sigma^2_{alias}, \sigma^2_{fit}$ are the WFS and the DM errors.
At H band we can estimate the mean square residual error from the analytical formula of the fitting error, and so an estimation of the SR. The SR resulted from the simulation at the different science target directions is quite acceptable comparing to the analytical formula. This simulation represents many advantages in terms of the computional loads, providing the E2E-S efficiency and capability in simulating an E2E AO system for the ELT. The full EAGLE simuation comprising HO-LGS and LO-NGS GSs, is pending, and the linear sparse projector used in the EAGLE-like simulation of 7.10^{13} elements, is seperated to a

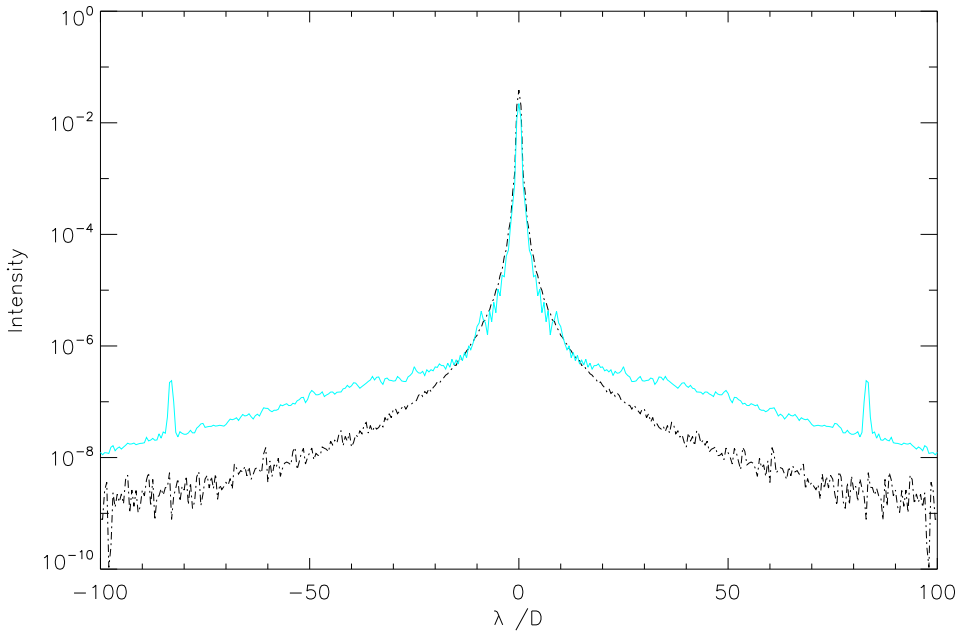


Figure 9.4: PSF profile for compensated turbulence of the EAGLE-LIKE simulation (blue line). The dark line shows the diffraction-limited PSF profile.

LO linear projector and a HO hyperbolic projector. Moreover, assuming the split tomography, we can take advantage of its optimal solution in terms of the computational loads and costs. We avoide by using the split tomography to build a reconstructor sparse matrix for 10 GSs .

Conclusion

The thesis presented in this manuscript is dedicated to **Refined Adaptive Optics simulation with wide field of view for the ELT**. The development of a new code for simulating an adaptive optics system with high degrees of freedom and the validation of this latter have been the main topic in this thesis. In particular, we have been concentrated on the tomographic reconstruction and the correction of the atmospheric turbulence and its use for physical simulation and prediction of wide field AO systems behavior.

We have summarized all the existing analytical and numerical tools for simulating AO instruments. We studied the performance using the CAOS simulator and the evaluation of the computational cost as a function of the number of degrees of freedom (number of simulated layers, subapertures and number of iterations). We then identified the bottleneck in a process or in the AO systems simulations. In fact, current AO systems are using VMM reconstructors to convert gradient measurements into an estimated phase. Such a computing for such a method needs N^2 floating point operations and the cost of the matrix inversion required to prepare the estimator scales as $O(N^3)$. Furthermore, N scales as D^2, with D the telescope diameter, so the result of the VMM scales as D^4 and the matrix inversion is of complexity $O(D^6)$. This complexity requires optimization before good performance can be achieved so a certain simulation of adaptive optic system is necessary to categorize the expected performance. We propose as a solution a new simulator code dedicated to the ELT which allows a management of the high degrees of freedom, based on an iterative resolution of the linear model $y = A * x$ with high degrees of freedom using the sparse matrices properties.
The E2E-S tool is an in-house IDL-based E2E modelling of the adaptive optics system including atmospheric effects, telescope parameters, AO sub-system, as well as science observations at large field of view. This simulator is based on a sparse library with Yorick/IDL originates from a collection of IDL/C routines that are used together for a specific purpose: efficient wave front reconstruction in adaptive optics simulations.
We present a new sparse tomographic projector using the efficient RCO scheme, allowing the projection of the turbulent phase at the pupil of the telescope from all the layers and for all the sky directions. This phase is then measured by a new sparse realistic Geometry Model of Shack- Hartman WFS. We show then the MAP reconstructor in a sparse format using a modest approximation for the inversion of the phase covariance matrix C_ϕ^{-1} playing the role of the regularization term that helps the inversion to take place. The MAP recontructor is then solved by an iterative method, the conjugate gradient where we assure a fast convergence with the Jaccobi preconditioner PCG.
Concerning the Laser Guide Star issues: the cone effect, the fluctuation of the sodium

layer and the fusion data given the LGS and the NGS measurements are presented. We investigated, as well as new techniques for filtering tip, tilt and defocus from the measurements vector data of a spherical wave front distortion. The idea consists in modifiying the data model to a model that excludes the TTF modes. We proposed in finding a transformation matrix M to an orthogonal space that exclude the modes in question. The key is based in taking into considerations all the modes generated by the DM while inverting the transformation matrix M. A new hyperbolic projector dedicated to the LGS reference sources based on the sparse approach is also presented. It's an operator that computes wavefront values at the intercept of rays traced through phase screens to the pupil plane of the telescope. We demonstrate that this LGS projector is hyperbolic, allowing the expand of the LGS mesh size with range according to the cone compression factor. The work is then verified using a MUSE-like case where we show the cone effect on the performance at the center of the FOV for different positions of the Laser GSs on a circle of a variable diameter. For a better performance of an LTAO system, Laser GSs must be placed on a circle of 22 arcsec diameter and above.
The fusion data LGS/NGS was also treated and analyzed by using the integrated tomography. The estimation was performed from the fusion data HO/LO, the latter was required to measure the tip, tilt and defocus filtered from the former, i.e. from the LGS measurements. The LGS/NGS measurements are concatenated in a single vector and one reconstructor was applied to estimate the volumic tomography. Many simulations and tests are then evaluated in order to validate the new module *fusion data NGS/LGS* added to the E2E-S simulator code. And finaly we present an EAGLE-like E2E simulation using the E2E-S tool.

Perspective

The work presented in this manuscript allows us to study any AO system on small or large telescopes, providing a new complete code for a fine AO simulation. The developed E2E tool is very essential for a fine simulation of an AO system with wide field of view. In fact, the new intruments of the phase A studies of the E-ELT requires new strategies and simulator codes for a fast and E2E simulations, in order to understand the behavior of the instrument and identify the bottleneck.
We develop the structure of an E2E simulator based on sparse routines and formed by different blocks refered each to an AO sub-system which was all analyzed and performed using many simulation cases presented in this dissertation. However, for the second part of this manuscript relative to the E2E-S, it is still necessary to make some optimisation of these routines especially the RUPCG or the reconstructor operator. It is important to paralelize this operator for a fast estimation of the inverse problem.
Concerning the third part, it would also be usefull to extend the studies that include laser guide stars, since all AO instruments for wide field of view under developement or integration call for the use of LGS in order to increase the sky coverage. The use of these laser GS raises new problems and complicate the AO systems. In this dissertation, we are interested in the theoretical consideration of the LGS but we didn't consider in particular the problems related to the elongation of the spot while analysing the spherical distortion with the WFS, which has an impact on the measurement noise.
Moreover, for the new generation of AO systems on an ELT, concepts themselves will become more complex: mirrors covering all the field of view associated to dedicated mirrors inside the scientific instrument itself will have to be coupled with split or integrated tomography schemes, differential pupil or/and field rotations will have to be considered, etc.
Finaly we proposed a complete E2E tool dedicated for the ELT, allowing the study of any AO system (such as MOAO, MCAO or LTAO), providing for instance a safe, and relatively very cheap (in term of both cost and time) testbed to evaluate the side effects, usually hardware related, like telescope vibration; and to understand the behavior of the instrument in order to optimize the performance of the system.
It might finally be noticed that AO systems are integrated into telescopes with other instruments such as camera or coronagraph...
It will therefore be important in a near future to extend the work presented here in order to simulate in the same E2E simulation the telescope, the AO system and the instrument (camera, coronagraph...). Only such a simulation tool will give access to a complete and full understanding of the behaviour of the future ELTs instruments.

Simulation fine d'Optique Adaptative grand champ pour les E-ELT

Introduction á l'Optique Adaptative

L'Optique Adaptative (OA) est une technique utilisée pour compenser en temps réel les aberrations créées lorsque la lumière se propage dans un milieu non homogène. Actuellement ses applications les plus importantes se trouvent en astronomie, dans le domaine militaire, et de plus en plus dans le domaine médicale.
La figure 2.1 propose une description générale d'un système d'OA. Ce dernier nécessite ainsi trois éléments clés:

- Un Analyseur de Surface d'Onde (ASO) qui mesure les déformations du front d'onde incident;
- Un Miroir Déformable (MD) qui compense les perturbations mesurées afin d'obtenir un front d'onde quasi plan au foyer de l'instrument;
- Un système d'asservissement temps réel qui pilote les deux éléments précédents et permet de transformer la mesure en déplacement du MD grâce à une loi de commande.

Le front d'onde perturbé par la turbulence atmosphérique est analysée par un ASO. Cette mesure est traitée par un système informatique temps réel afin de contrôler le DM. Ce miroir est alors déformé afin d'imprimer au front d'onde une correction opposée à la perturbation qu'il a subi lors de la traversée de la turbulence atmosphérique. Au final, le front d'onde corrigé doit redevenir plan et permettre donc d'observer sur une voie d'imagerie une image corrigée, proche de la limite théorique de diffraction du système optique.

Nouveaux concepts d'OA

Le concept GLAO

Le concept de Ground Layer Adaptive Optics (GLAO) [Rigaut (2002)], est un autre concept d'OA grand champ dédié à la correction de la couche turbulente proche du sol. Ce système utilise un unique miroir conjugué de la pupille ou à basse altitude. Le but est de proposer une correction modérée de la turbulence mais dans un grand champ et la plus homogène possible. Ce type de correction répond notamment aux besoins astronomiques pour les études extra-galactiques et la cosmologie, et ce pour un coût modéré. La couche basse de la turbulence représentant le plus souvent la majeure partie de la turbulence, sa correction par un unique miroir doit permettre de répondre à cet objectif. Le principe du GLAO est présenté sur la figure 3.1: plusieurs ASO permettent de sonder le volume turbulent. Les effets des couches en altitude se moyennent et s'annulent et la phase moyenne résultante est alors liée uniquement à la phase dans la couche au sol, commune à toutes les directions d'analyse.

Le concept LTAO

Comme les objets d'intérèt sont trés peu lumineux, il est necessaire d'utiliser des étoiles Guides (EG) laser réparties dans le grand champ pour sonder le volume turbulent et réaliser une reconstruction tomographique de la turbulence. C'est une correction par un miroir unique conjugué de la pupille d'entrée qui est appliquée, comme en OA classique. Le principe est ici d'offrir une correction de type OA classique (donc de champ limité) dans une zone du ciel dépourvue d'étoiles guides assez lumineuses (augmentation de la couverture de ciel). Par conséquent, l'utilisation de quelques étoiles naturelles, ou plus probablement laser, permet de réaliser l'analyse de la turbulence dans le volume et son estimation dans la direction d'intérêt afin de fermer la boucle de correction d'OA. La figure 3.3 présente le principe LTAO.

Le concept MOAO

L'OA Multi-Objet (MOAO) répond à un besoin astronomique particulier : celui de pouvoir observer simultanément plusieurs galaxies dans un grand champ pour faire de la spectro-imagerie. La MOAO peut être réalisée en utilisant pour chaque objet d'intérêt une OA tomographique miniature, se composant typiquement de trois analyseurs de front d'onde et d'un micro-miroir réalisant une correction dans la pupille. Des étoiles guides naturelles sont utilisées pour l'analyse du front d'onde. Une reconstruction tomographique de la turbulence est réalisée et la correction est optimisée pour la direction d'intérêt. L'asservissement fonctionne cependant en boucle ouverte. La figure 3.4 présente le principe du MOAO.

Simulation End-2-End de l'OA

La majeure partie de nos études de simulation est faite avec l'outil E2E-S, un simulateur E2E développé sous IDL pour le système d'optique adaptative, y compris les effets atmosphériques, les paramètres du télescope, les sous-systèmes de l'OA, ainsi que des observations scientifiques à grand champ de vu. Ce code est basé sur une grappe de PC et d'une bibliothèque dédiée développée en C. Il utilise un certain nombre de fonctions personnalisées à chaque modèle d'OA développé pour répondre à nos besoins. Ils peuvent être appelés tous ensemble afin de simuler l'ensemble du processus ou simuler des parties spécifiques du système d'OA pour étudier ou résoudre des problèmes particuliers tels que les problèmes relatifs au étoiles Laser (LGS).

Structure globale de E2E-S

Le simulateur E2E-S est développé dans le but de fournir une analyse détaillée du comportement physique d'un système d'OA. E2E-S est une concaténation des blocs représentant chacun un sous-système d'OA. Ce simulateur est utilisé pour quantifier la perfor-

mance du système en entier, et propose une étude physique détaillée de chaque sous-système. E2E-S est un ensemble de fonctions et de routines creuses sous IDL, développé au LAM en collaboration avec l'ONERA de Paris, afin de simuler les différents composant d'OA. Ces fonctions séparées peuvent être assemblées librement pour simuler différents systèmes (OA ... MOAO) avec différents niveaux de complexité et de degrés de liberté, en prenant les avantages du format des matrices creuses.
E2E-S est développé afin de mettre en œuvre et de résoudre les problèmes générés par l'ELT (effet de cône, indétermination de tip, tilt et défocus, fusion de données EGL / EGN). L'objectif final d'un tel outil est d'être capable de simuler EAGLE, un instrument de l'E-ELT. Dans cette partie on va exploiter les différents blocs modélisés par le E2E-S.

Systeme de configuration

Un fichier permet de lister les paramètres intervenants dans la simulation. Cette structure comprend les paramètres d'observation (caractéristiques du télescope, conditions atmosphériques, paramètres des étoiles guides ou des objets visés, champ de vue...), les paramètres de l'OA (caractéristiques du ou des miroirs déformables, des analyseurs de surface d'onde, de la loi de commande...) et les conditions de la simulation (paramètres visuels, nombre d'itérations, données à calculer et á sauvegarder...).

Un simulateur de turbulence

Ce simulateur de turbulence permet de générer une turbulence atmosphérique multi-couches dynamique sous la forme d'écrans de phase point à point. C'est une approche dite zonale. La turbulence sous forme de phases pixellisées est de type Kolmogorov ou Von Karman. Ces écrans sont mis a l'échelle afin de respecter les caractéristiques souhaitées pour la turbulence (D/r_0, vitesse de vent, L_0, altitude, Cn^2). On néglige la propagation de Fresnel, on se place en régime de faibles perturbations et les variations d'amplitudes sont négligées.

Un simulateur "creux" d'analyseur de front d'onde

Nous proposons dans ce paragraphe une modélisation linéaire de l'Analyseur de Front d'Onde (ASO) en format creux sans dynamique temporelle. Le modèle d'ASO fournit une mesure zonale du front d'onde. Ce modèle creux est le plus représentatif du comportement d'un analyseur de type Shack-Hartmann (SH). Cet ASO est basé sur une approximation discrète donnée par l'équation 9.2 qui relie la dérivée de la phase de chaque sous pupille á la pente locale mesurée.

$$S_x = \frac{\lambda}{2\pi d_x} < \phi_{xmax} - \phi_{xmin} > \tag{9.2}$$

Où d_x représente la taille en x d'une sous pupille, ϕ_{xmax} et ϕ_{xmin} sont les phases pixélisées, <. > désigne la moyenne spatiale de la phase. Le calcul se résume à moyenner sur chaque sous pupille les différences de phase d'un bord à l'autre de la sous pupille. Les sous pupilles partiellement éclairées sont gérées similairement en prenant en compte la portion éclairée de la sous pupille. Ce modèle nécessite de connaître la structure de l'ASO (nombre de sous pupilles) et le choix des sous pupilles valides. Cette approche discrète permet de fournir un modèle simple mais réaliste de la mesure d'un Shack- Hartmann, prenant en entrée un front d'onde discrétisé spatialement sur une carte de points (approche Zonale) et donnant en sortie une mesure de pente en x et y.
On se basant sur une librairie creuse on construit la matrice de l'ASO en format RCO donné par le tableau 5.1.

Un modèle creux de miroir déformable

Les miroirs sont modélisés sous forme de composants linéaires dont la réponse est instantanée et linéaire. Ils sont alors entièrement caractérisés par leurs Fonctions d'Influence (FI), c'est-à-dire la déformée générée à l'activation de chaque actionneur. Les FI sont estimées par le modèle à double gaussienne. Ce modèle est identique pour tous les actionneurs. Nous définissons chaque FI sur un certain nombre d'actionneurs. Ce nombre est décrit comme *Nacinf* : nombre d'actionneurs d'influence, au-delà de *Nacinf* la FI est mise à zéro. Les dimensions du DM sont également nécessaires comme le nombre d'actionneurs et le nombre de pixels par actionneur.
Le format RCO de la matrice des FIs est l'assemblage des vecteurs définis sur une base de pixels pixélisé N*N, qui représente chacun des actionneurs valides *NACT_valid*. Ces vecteurs se réfèrent à la phase formée par le miroir une fois l'actionneur en question activé. La matrice finale est de type RCO de [n * n, NACT_valid]. La figure 5.11 représente le profil de la fonction double Gaussienne pour un DM de 8 * 8 actionneurs avec 45% de couplage mécanique et *Nacinf* = 4. L'artefact montré explique la discontinuité sur la phase formée par le miroir comme illustré dans la figure 5.12 et affecte également les hautes fréquences soit l'erreur de *fitting*. Donc, il est important de minimiser ce nombre sans affecter le caractére creux de la matrice. Nous avons trouvé *Nacinf* = 6, ce qui signifie que FI est mise à zéro au-delà du troisième actionneur. Et comme cela est montré sur la figure 5.13 ce saut a disparaît et le miroir reproduit le tip mode.

Reconstruction creuse du front d'onde

Pour un profil de turbulence donné, composé de n_l couches turbulentes, la phase résultante pour une direction donnée α dans le champ se déduit de la phase dans le volume par la relation :

$$\varphi^{tur}_{\alpha_i}(r) = \sum_{l=1}^{n_l} \varphi^{tur}_{l}(r + \alpha_i h_l) \tag{9.3}$$

où φ_l^{tur} représente la phase turbulente pour la couche l située à l'altitude h_l. r est le vecteur des coordonnées spatiales dans la pupille. En décomposant les écrans de phase sur une base donnée, l'équation 9.3 peut se réécrire sous une forme matricielle :

$$\phi_\alpha^m = P_{s,\alpha}^h \phi^{tur} + n \tag{9.4}$$

où $P_{s,\alpha}^h$ est un projecteur creux linéaire relatif à la propagation de la phase dans une direction d'analyse α donnée. Ce projecteur permet d'ajouter la contribution de la phase provenant de chaque couche à l'altitude au plan pupille du télescope. On se basant sur une interpolation bilinéaire, on a construit $P_{s,\alpha}^h$ comme étant une matrice creuse formée de plusieurs blocs relatifs a chaque couche et chaque direction d'analyse. Alors l'équation 9.4 peut être expliciter comme:

$$\begin{pmatrix} \varphi_{pup}^{\alpha_1} \\ \vdots \\ \varphi_{pup}^{\alpha_i} \\ \\ \vdots \\ \varphi_{pup}^{n_\alpha} \end{pmatrix} = \begin{pmatrix} P_{\alpha_1}^{h_1} & \cdots & P_{\alpha_1}^{n_l} \\ & \ddots & \\ P_{\alpha_i}^{h_l} & \cdots & P_{\alpha_i}^{n_l} \\ \vdots & & \vdots \\ P_{n_\alpha}^{h_1} & \cdots & P_{n_\alpha}^{n_l} \end{pmatrix} \begin{pmatrix} \varphi_{h_1}^{tur} \\ \varphi_{h_2}^{tur} \\ \vdots \\ \varphi_{h_n}^{tur} \end{pmatrix} + \begin{pmatrix} n_{\alpha_1} \\ \vdots \\ n^{\alpha_i} \\ \\ \vdots \\ n_{n_\alpha} \end{pmatrix} \tag{9.5}$$

Le projecteur $P_{s,\alpha}^l$ peut alors être vu comme la matrice d'interaction du système qui, à partir des phases dans le volume (que l'on va chercher à estimer et à reconstruire) permet d'obtenir le jeu de mesures de phases résultantes sur la pupille du télescope dans les différentes directions d'analyse. La reconstruction de front d'onde à grand champ consiste à tenter de reconstruire au mieux le volume de turbulence, en adoptant l'estimateur Maximum *A Posteriori* la phase estimée dans les couches est donnée par la formule suivante:

$$\hat{\phi}^{tur} = (P_s^T C_n^{-1} P_s + C_{kol}^{-1})^{-1} P_s^T C_n^{-1} \phi_\alpha^m \tag{9.6}$$

où C_n et C_{kol} sont respectivement les matrices de covariance du volume de turbulence et du bruits dans les différentes directions d'analyse. On suppose que la statistique de bruit est la même sur chaque mesure et que ces statistiques sont décorrélées, alors $C_n^{-1} = \sigma_m^{-2} I$. Pour le calcul de la matrice C_ϕ l'approximation proposée par [Ellerbroek (2002)] est adoptée. Selon cet auteur

$$C_{kol}^{-1} \approx \gamma \nabla^4 \tag{9.7}$$

où γ est une constante, ∇^2 est le Laplacien. Equation 9.6 peut être alors écrite comme:

$$\hat{\phi^{tur}} = (P_s^T P_s + \sigma_m^2 C_{kol}^{-1})^{-1} P_s^T \phi_\alpha^m \tag{9.8}$$

9.8 se résoudre itérativement en utilisant la décomposition de Cholesky et le gradient conjugué avec un precoditionnement Jaccobi.

Validation du code E2E-S

On s'intéresse dans ce paragraphe à la validation du code E2E-S développé durant les années de ma thèse. Pour comparer, on a considèré un cas simple d'OA:

- 1 couche
- 1 direction d'analyse
- 6 pixels par sous-pupille
- N iterations = 100

Dans la figure 5.24 on présente le temps de calcul mis par le code E2E-S et un autre code européen CAOS pour comparaison. Ce temps est la somme des temps nécessaires pour la calibration et la reconstruction. Ce test nous montre qu'on est 7 fois plus rapide que CAOS. Ce code est alors capable de simuler un instrument E2E comme EAGLE par exemple.

Nouveaux enjeux en OA grand champ

Aprés avoir introduit l'outill de simulation développé durant ma thèse, on s'intéresse dans ce paragraphe aux problématiques posé suite à l'utilisation des étoiles Laser qui permettent d'augmenter la couverture de ciel et en théorie permettraient de donner accès à l'ensemble de la voute céleste. On limite notre étude à deux phénomènes majeurs : l'indétermination du tip-tilt et l'effet de cône.

Indétermination du tip, tilt et défocus

La position de l'EG laser sur le ciel est toujours inconnue du fait du retour inverse de la lumière. Le faisceau laser parcourt toujours le même trajet et n'est pas affecté par les modes tip-tilts dus à l'atmosphère. La mesure de ces modes n'est donc pas possible sur une EG laser. Pour palier à ce défaut, la plupart des systèmes à EG laser prévoit

l'utilisation d'EG naturelles pour faire la mesure de tip-tilt. Il est alors important de gérer, au niveau de la commande, ces données de natures différentes lors de la reconstruction du volume turbulent. En outre, la couche de sodium n'est pas statique, mais en constante évolution. La hauteur moyenne, ainsi que l'épaisseur et le profil de densité de l'atome de sodium sont en fluctuation continue. Cette fluctuation de la couche de sodium aura une incidence sur la connaissance de l'endroit où l'EGL est focalisée, introduisant par la suite une erreur de focalisation qui ne peut être distinguée de la turbulence optique et peut conduire à une perte de performance de système d'AO. Pour ces raisons, il est très intéressant de filtrer les modes tip-tilt et défocus. L'idée est de changer le vecteur mesure en un vecteur qui exclu les trois modes en question. Nous avons proposé trois méthodes. Dans ce paragraphe, nous allons expliciter deux méthodes, la première étant de mettre la moyenne des pentes à zéro et la deuxième de trouver une nouvelle bases orthogonale au tip-tilt et au défocus.

Mettre la moyenne des pentes a zéro

Dans cette méthode, on propose de trouver la matrice qui moyenne les pentes à zéro dans le but de trouver une nouvelle mesure $S_{hTT} = S - \bar{S}$ qui filtre le tip-tilt et le défocus. La nouvelle matrice de mesure devient :

$$D_{\perp} = (ID - MM^{\dagger})D_s \tag{9.9}$$

Où M est la matrice de transformation en question vers une nouvelle base orthogonale. Dans ce cas cette matrice est donnée par :

$$MM^{\dagger} = \frac{1}{n}\begin{bmatrix} 1 & \cdots & 1 \\ \vdots & 1 & \vdots \\ 1 & \cdots & 1 \end{bmatrix} \tag{9.10}$$

Slopes out of TTF evalulates to:

$$S_{OTT} = (ID - \frac{1}{n}\begin{bmatrix} 1 & \cdots & 1 \\ \vdots & 1 & \vdots \\ 1 & \cdots & 1 \end{bmatrix})S \tag{9.11}$$

Malheureusement, mettre la pente moyenne à zéro ne supprime pas la contribution totale de tip et de tilt. La figure 7.4 montre le résultat non satisfait : une fois la moyenne des pentes mise à zéro, il reste 7% de contribution de tip-tilt. Cette méthode n'a pas donc filtrer la contribution totale de tip-tilt et de plus elle n'a rien changé à la perturbation sphérique .

M contient la réponse de l'ASO à tous les modes générés par le MD

Dans cette méthode, la matrice M doit contenir la réponse de l'ASO a tous les modes générés par le system. $M^{\dagger}_{system} = [S_{TIP} S_{TILT} S_F \cdots S_{nmode}]^{\dagger}$, avant de passer à l'inversion généralisée.
Pour cela, on propose d'utiliser la base de Karhunen-Loëve afin de trouver tous les modes créées par le MD.

$$MM^{\dagger} = [S_{TIP} S_{TILT} S_F][S_{TIP} S_{TILT} S_F]^{\dagger} \tag{9.12}$$

Figure 7.6 montre les résultats de cette méthode où nous avons bien réussi à filtrer toute la contribution de tip-tilt et défocus. Par la suite, on adoptera cette solution pour le filtrage de tip-tilt et défocus, surtout pour la fusion des données EL et EN.

L'effet de Cône

l'EG laser émet sa lumière à une altitude finie, contrairement au cas d'un objet stellaire. L'onde reçue n'est donc plus plane mais sphérique. Ainsi, les perturbations de phase vues par l'ASO ne sont pas exactement les mêmes que celles obtenues sur une EG naturelle. Plus le diamètre du télescope est grand, plus l'effet de cône devient important. L'erreur résiduelle due à l'effet de commande est liée au diamètre du télescope. Pour limiter son impact, il est nécessaire d'utiliser plusieurs EG laser afin de synthétiser le cylindre d'une étoile naturelle avec plusieurs faisceaux coniques des EG lasers. La figure 7.8 présente le principe de la tomographie en utilisant les EG laser, qui nécessite par la suite l'utilisation d'un nouveau projecteur non linéaire afin d'étirer les couches à l'altitude d'un facteur de $rp_{zoom} = \dfrac{pup_{LGS}}{D_{pix}}$ et de les sommer au plan pupille du télescope. On a démontré que ce projecteur est un projecteur hyperbolique comme il est montré dans la figure 7.9.

L'effet de cône et le projecteur hyperbolique ont été évalués et simulés. En partant des conditions de simulation données, on a étudié l'impact sur la performance de la position des étoiles guides laser et naturelles. Les EG sont placées sur un cercle de rayon variable. On a étudiés les positions des EG pour des diamètres de 6" ,10", 22" ,30", 40" et 60". De plus, on a déterminé la position optimale des EG garantissant la meilleure performance en terme de SR au centre du champ. Les résultats obtenus avec des EG naturelles sont aussi présentés. Ces EG doivent alors être placées 'a au moins 22". Compte-tenu des contraintes du système, c'est le cas 4 EG où les EG sont placées sur un cercle de 11" de rayon qui a été retenu. Il s'agit du cas optimal d'après cette étude. Pour des champs supérieurs à 11", la performance obtenue avec des EG laser est plus faible que celle obtenue avec des EG naturelles car l'anisoplanetisme résiduel est plus fort en présence d'EG laser puisque les recouvrements des empreintes en altitude sont plus grands dans ce cas.

Fusion des donnees étoiles lasers et naturelles

Dans ce paragraphe on s'intéresse à la tomographie en utilisant des données étoiles laser et naturelles. Pour cela on fait appel à la deuxième méthode de filtrage tip-tilt et défocus et on compare deux approches de fusion des données EGL/EGN : *Integrated Tomography* et *Split Tomography*.
Integrated Tomography proposée dans la figure 8.2, consiste à estimer la phase mesurée au plan pupille du télescope, et donner les mesure hauts ordres EGL et bas ordres EGN. Ces phases sont ensuite concaténées dans un simple vecteur au plan pupille afin d'être appliquées au bloc *TOMO* pour la reconstruction de la phase turbulente dans le volume.

Split Tomography proposé dans la figure 8.1, consiste à séparer les boucles de mesures EGN et EGL. Cette approche est connue comme la solution optimale en termes de complexité de calcul. Le reconstructeur de tomographie est réduit à la tomographie par EGL. L'EGN ne participe pas à la résolution des méthodes itératives permettant moins d'itérations et de complexité au niveau du RTC.

On propose une simulation numérique E2E-S afin de comparer ces deux approches. On considère pour cette raison deux EGL placées sur un cercle de diamètre variable. Les performances sont calculées en terme du SR au centre du champ. La figure 8.4 représente la comparaison entre ces deux méthodes.

On a trouvé des performances un peu meilleures lors de l'utilisation de l'*Integrated Tomography*. Cependant *Split Tomography* presente une efficacité en terme de taux de calcule et de complexité, pour 4 hauts ordres EGL et 3 bas ordres EGN et pour les mêmes conditions de turbulence *Split Tomography* est 7 fois plus rapide que *Integrated Tomography*.

Conclusion

On a présenté dans cette thèse le développement d'un nouveau simulateur E2E basé sur les matrices creuses et dédié aux futurs télescopes avec de nombreux degrés de liberté. Cet outil de simulation a été validé bloc par bloc. Les nouveaux enjeux pour la nouvelle génération de télescopes ont été examinés et simulés en utilisant ce code. L'implémentation des étoiles laser ainsi que ses problématiques a été développée et validée. On a présenté une nouvelle méthode de filtrage des tip-tilt et defocus et un nouveau projecteur hyperbolique dédié à l'utilisation des étoiles guide laser. Ces méthodes ont été regroupées ensemble pour la simulation et le test des approches de fusion de données EGL et EGN.

Appendix A

The sparse row-wise format

For either nonsymmetric or symmetric the sparse storage representation of a general matrix A of $n\times$ m is given by the three vectors: IX, JX and XN.

- X: A vector of same data type as the matrix A, that contains all the nonzero values of A if it is nonsymmetric, and only the nonezero entries in each row on and above the main diagonal if A is symmetric so that a computer memory can be then saved. In both cases the entries are sequentially stored to X following the order of rows of A.
- J: An integer array of the same length as X, such that J[k] is the column number for the value X[k].
- I: A mapping integer vector is used to count the number of non-zero elements in each row of A. The elements of I thus specify where in J and X to start looking for the nonzero elements of a given row. I will contain n+1 elements.

As an example we considere a matrix A given by :

$$\begin{array}{ccccc} 0 & 2 & 0 & 9 & 0 \\ 6 & 0 & 9 & 0 & 10 \\ 3 & 2 & 0 & 8 & 0 \end{array} \tag{A.1}$$

Storing only the nonzero elements would give the RR(C)O structure (with a zero-indexing convention of IDL)

$$\begin{array}{c} X = \begin{pmatrix} 2. & 9. & 6. & 9. & 10. & 3. & 2. & 8. \end{pmatrix} \\ J = \begin{pmatrix} 1 & 3 & 0 & 2 & 4 & 0 & 1 & 3 \end{pmatrix} \\ I = \begin{pmatrix} 0 & 2 & 5 & 8 \end{pmatrix} \end{array} \tag{A.2}$$

The non zeros elements of the matrix A are then stored in the vector X, the first row of the matrix A is then given by I[0] = 0 of X and J, that means that the first row begins at J[0] and X[0].
I[1] = 2 that means that the second row begins at J[2] = 0 and X[2] = 6. The elements of I are thus pointers to where in X we start looking for the nonzero entries of each row,

and where in J to start looking for the column index of each nonzero number in the corresponding row. The last number of I represent the total number of nonzero elements to be stored.

Let us consider the case of symmetric row-wise storage, for a given symmetric matrix B :

$$B = \begin{matrix} 2 & 4 & 0 & 1 \\ 4 & 5 & 0 & 2 \\ 0 & 0 & 1 & 0 \\ 1 & 2 & 0 & 9 \end{matrix} \tag{A.3}$$

We use the RUO mode which only stores the upper triangle of B in I, J and X, while the diagonal is stored seperately in D.

$$\begin{aligned} X &= \begin{pmatrix} 4 & 1 & 2 \end{pmatrix} \\ J &= \begin{pmatrix} 1 & 3 & 3 \end{pmatrix} \\ I &= \begin{pmatrix} 0 & 2 & 3 \end{pmatrix} \\ D &= \begin{pmatrix} 2 & 5 & 1 & 9 \end{pmatrix} \end{aligned} \tag{A.4}$$

Appendix B

SOY library fine print

Now we care about the different sparse matrix routines dedicated for the numerical AO simulations, developped in C++ the routines are called from IDL using DLM (Dynamically Loadable Module) represented by **Call_External**. IDL is basiclly used as a wrapper for the C programs. SOY library allows the user to indicate the number of non-zero entries by setting a global default value or specifying memory allocation while calling for the function. The first one is done by indicating within the script **MR** and **MN** and it will cover most of applications without hogging too much memory. The second is accomplished by activating the keywords **(ur=,un=)** when calling the function once the memory needed exceeds the one indicated in **MR**. For both cases **MR** and **ur** indicate the maximum number of rows to accomodate which specify the length of IX and or D in the RUO scheme case, **MN** and **un** allow us to define the maximum number of non-zero elements to store or the lengh of J and X described in 5.3.
SOY library is a free software [Flicker (2009)] ported for both 64-bit and 32-bit compatibility and so for Mac OS 32-bit machines by compiling the IDL lines:

```
dir = './LIB/SOY/soi/'
!make_dll.compile_directory = dir
make_dll,'soi',",input=dir,output=dir+", compile=dir,/verbose,/show, extra_lflags=
'-m32', extra_cflags='-c -m32 -malign-double -O3 -shared -fnested-functions'
dir = './LIB/SOY/ptsoi/'
!make_dll.compile_directory = dir
make_dll,'ptsoi',",input=dir,output=dir+", compile=dir,/verbose,/show, extra_lflags=
'-m32', extra_cflags='-c -m32 -malign-double -O3 -shared -fnested-functions'
```

B.1 Functions and Routines

rco__define.pro Initializes *A* as the RCO structure:
As = rco
As.r = number of rows to accomodate
As.c = number of columns to accomodate
As.n = number of none zero elements to be stored

As.i = ptr_array(int,As.r)
As.j = ptr_array(int,As.n)
As.x = ptr_array(float,As.n)

ruo__define.pro
Initializes *A* as the RUO structure:
As = ruo
As.r = number of rows to accomodate
As.c = number of columns to accomodate
As.n = number of none zero elements to be stored
As.i = ptr_array(int,As.r)
As.j = ptr_array(int,As.n)
As.x = ptr_array(float,As.n)
As.d = ptr_array(float,As.r)

sprco.pro (sprco.c)
Compresses the 2D matrix *A* into a sparse RCO format, subject to the threshold level t, t is set by default to 0
: A_s=sprco(*A*,t=,**ur**=,**un**=)

spruo.pro (spruo.c)
Compresses the 2D symmetric matrix *A* into a sparse RUO format, subject to the threshold level t, t is set by default to 0
: A_s=spruo(*A*,t=,**ur**=,**un**=)

rcoadd.pro (rcoadd.c)
Sparse addition of two RCO matrices *A* and *B* with single and double precision, subject to the threshold level t (default t = 0) :
C_s= rcoadd(A_s,B_s,**ur**=,**un**=)

ruoadd.pro (ruoadd.c)
Sparse addition of two RUO matrices *A* and *B* with single and double precision, subject to the threshold level t (default t = 0) :
C_s= ruoadd(A_s,B_s,**ur**=,**un**=)

rcoata.pro (rcoata.c)
Computes the covariance matrix of an RCO structure *A*, sparse mutiplication of *A* with its transpose from the left:
$B_s = rcoata(B) = A^T A$

rcoinf.pro
Inflates RCO compressed matrix to full form:
A = rcoinf(A_s)

ruoinf.pro
Inflates RUO compressed matrix to full form:
A = ruoinf(A_s)

rcoxv.pro (rcoxv.c)
Sparse matrix-vector multiplication of an RCO matrix A_s and real vector v:
u = rcoxv(A_s,v)

ruoxv.pro (rcuoxv.c)
Sparse matrix-vector multiplication of an RUO matrix A_s and real vector v:
u = rcoxv(A_s,v)

ruopcg.pro
Preconditioned conjugate gradient solver for a symmetric positive definite sparse linear system, with Jacobi preconditioner. This algorithm is implemented straight out of Numerical Recipes, with the VMMs carried out sparsely by the ruoxv(a,v) function. Optionally one may invoke symmetric Gauss-Seidel iterations upon the Jacobi preconditioning, by setting the keyword **sgs=iters**. An initial guess is supplied in x_0, and the keyword **tol** specifies the threshold of convergence (default $47 * 10^{-7}$) for when to exit the iteration:
v = ruopcg(A_s,b,x_0,/tol,/sgs)

Bibliography

Ahmadia, A. J. and Ellerbroek, B. L. (2003). Parallelized simulation code for multi-conjugate adaptive optics. In Tyson, R. K. and Lloyd-Hart, M., editors, *Society of Photo-Optical Instrumentation Engineers (SPIE) Conference Series*, volume 5169 of *Society of Photo-Optical Instrumentation Engineers (SPIE) Conference Series*, pages 218–227.

Arsenault, R., Madec, P.-Y., Hubin, N., Paufique, J., and Stroebele, S. (2008). ESO adaptive optics facility. In *Society of Photo-Optical Instrumentation Engineers (SPIE) Conference Series*, volume 7015 of *Society of Photo-Optical Instrumentation Engineers (SPIE) Conference Series*.

Arsenault, R., Salmon, D., Kerr, J., Rigaut, F., Crampton, D., and Grundman, W. (1994). PUEO, the Canada-France-Hawaii Telescope Adaptive Optics Bonnette I: System Description. In Arsenault, R., editor, *Astronomy with the CFHT Adaptive Optics Bonnette*, page 1.

Babcock, H. W. (1953). The Possibility of Compensating Astronomical Seeing. *PASP*, 65:229.

Bacon, R., Bauer, S.-M., Bower, R., Cabrit, S., and Cappellari, M. (2004). The second-generation VLT instrument MUSE: science drivers and instrument design. In Moorwood, A. F. M. and Iye, M., editors, *Society of Photo-Optical Instrumentation Engineers (SPIE) Conference Series*, volume 5492 of *Society of Photo-Optical Instrumentation Engineers (SPIE) Conference Series*, pages 1145–1149.

Basden, A. G., Assémat, F., Butterley, T., Geng, D., Saunter, C. D., and Wilson, R. W. (2005). Acceleration of adaptive optics simulations using programmable logic. *Mon. Not. of the RAS*, 364:1413–1418.

Béchet, C., Tallon, M., and Thiébaut, E. (2006). FRIM: minimum-variance reconstructor with a fractal iterative method. In *Society of Photo-Optical Instrumentation Engineers (SPIE) Conference Series*, volume 6272 of *Society of Photo-Optical Instrumentation Engineers (SPIE) Conference Series*.

Beckers, J. M. (1988). Increasing the size of the isoplanatic patch with multiconjugate adaptive optics. In *Very Large Telescopes and their Instrumentation, Vol. 2*, volume 2, pages 693–703.

Boyer, C., Michau, V., and Rousset, G. (1990). Adaptive optics: interaction matrix measurements and real time control algorithms for the COME-ON project. In Tyson, R. K.

and Schulte In den Baeumen, J., editors, *Society of Photo-Optical Instrumentation Engineers (SPIE) Conference Series*, volume 1271 of *Society of Photo-Optical Instrumentation Engineers (SPIE) Conference Series*, pages 63–81.

Brusa, G. and del Vecchio, C. (1998). Design of an Adaptive Secondary Mirror: A Global Approach. AO, 37:4656–4662.

Carbillet, M., Boccaletti, A., Thalmann, C., and Fusco, T. (2008). The Software Package SPHERE: a CAOS-based numerical tool for end-to-end simulations of SPHERE/VLT. In *Society of Photo-Optical Instrumentation Engineers (SPIE) Conference Series*, volume 7015 of *Society of Photo-Optical Instrumentation Engineers (SPIE) Conference Series*.

Carbillet, M., Desiderà, G., Augier, E., and La Camera, A. (2010). The CAOS problem-solving environment: recent developments. In *Society of Photo-Optical Instrumentation Engineers (SPIE) Conference Series*, volume 7736 of *Society of Photo-Optical Instrumentation Engineers (SPIE) Conference Series*.

Carbillet, M., Vérinaud, C., Femenía, B., Riccardi, A., and Fini, L. (2005). Modelling astronomical adaptive optics - I. The software package CAOS. *Mon. Not. of the RAS*, 356:1263–1275.

Chassat, F. (1992). *Propagation optique a travers la turbulence atmospherique etude modale de l'anisoplanetisme et application a l'optique adaptative*.

Chebbo, M., Le Roux, B., Sauvage, J. F., and Fusco, T. (2010). Simulation of wavefront measurement and tomography for Extremely Large Telescope. In *Society of Photo-Optical Instrumentation Engineers (SPIE) Conference Series*, volume 7736 of *Society of Photo-Optical Instrumentation Engineers (SPIE) Conference Series*.

Cochran, G. M. (1986). Sparse matrix techniques in wavefront reconstruction. Technical Report TR-668, The Optical Sciences Company, Anaheim, Calif.

Conan, J. M., Madec, P. Y., and Rousset, G. (1992). Evaluation of Image Quality Obtained with Adaptive Optics Partial Correction. In Ulrich, M.-H., editor, *European Southern Observatory Conference and Workshop Proceedings*, volume 42 of *European Southern Observatory Conference and Workshop Proceedings*, page 475.

Conan, J.-M., Mugnier, L. M., Fusco, T., Michau, V., and Rousset, G. (1998). Myopic deconvolution of adaptive optics images by use of object and poin spread function power spectra. volume 37, pages 4614–4622.

Consortini, A., Ronchi, L., and Moroder, E. (1973). Role of the outer scale of turbulence in atmospheric degradation of optical images. *Journal of the Optical Society of America (1917-1983)*, 63:1246–1248.

Correia, E. (2010). *Design of high-performance adaptive optics control laws for large/very large astronomical telescopes*. PhD thesis, Ph.D.-Thesis, Université Paris-Nord.

Corrsin, S. (1951). On the Spectrum of Isotropic Temperature Fluctuations in an Isotropic Turbulence. *Journal of Applied Physics*, 22:469.

Costille, A. (2009). *Les optiques adaptatives grand champ : stratégie de correction et validations expérimentales*. PhD thesis, Ph.D.-Thesis, Universite Paris-Diderot - Paris VII , [2009].

Cuby, J.-G., Morris, S., Parr-Burman, P., Lehnert, M., and Evans, C. (2009). EAGLE: an MOAO fed multi-IFU working in the NIR on the E-ELT. In *Society of Photo-Optical Instrumentation Engineers (SPIE) Conference Series*, volume 7439 of *Society of Photo-Optical Instrumentation Engineers (SPIE) Conference Series*.

Demoment, G. (1989). Image reconstruction and restoration: overview of common estimation structures and problems. *IEEE Transactions on Acoustics Speech and Signal Processing*, 37(12):2024–2036.

Dessenne, C. (1998). *Commande modale et prédictive en optique adaptative classique*. PhD thesis, Ph.D.-Thesis, Universite Paris-Diderot - Paris VII , [1998].

Dicke, R. H. (1975). Phase-contrast detection of telescope seeing errors and their correction. *ApJ*, 198:605–615.

Diolaiti, E., Conan, J.-M., Foppiani, I., Lombini, M., and Petit, C. (2008). A preliminary overview of the multiconjugate adaptive optics module for the E-ELT. In *Society of Photo-Optical Instrumentation Engineers (SPIE) Conference Series*, volume 7015 of *Society of Photo-Optical Instrumentation Engineers (SPIE) Conference Series*.

Eikenberry, S., Andersen, D., Guzman, R., Bally, J., and Cuevas, S. (2006). IRMOS: The near-infrared multi-object spectrograph for the TMT. In *Society of Photo-Optical Instrumentation Engineers (SPIE) Conference Series*, volume 6269 of *Society of Photo-Optical Instrumentation Engineers (SPIE) Conference Series*.

Ellerbroek, B. L. (1994). First-order performance evaluation of adaptive-optics systems for atmospheric-turbulence compensation in extended-field-of-view astronomical telescopes. *Journal of the Optical Society of America A*, 11:783–805.

Ellerbroek, B. L. (2002). Efficient computation of minimum-variance wave-front reconstructors with sparse matrix techniques. *J. Opt. Soc. Amer. A*, 16:1803–1816.

Ellerbroek, B. L. (2005). Linear systems modeling of adaptive optics in the spatial-frequency domain. *Journal of the Optical Society of America A*, 22:310–322.

Ellerbroek, B. L., van Loan, C., Pitsianis, N. P., and Plemmons, R. J. (1994). Optimizing closed-loop adaptive optics performance using multiple control bandwidths. In Ealey, M. A. and Merkle, F., editors, *Society of Photo-Optical Instrumentation Engineers (SPIE) Conference Series*, volume 2201 of *Society of Photo-Optical Instrumentation Engineers (SPIE) Conference Series*, pages 935–948.

Evans, C., Morris, S., Swinbank, M., Cuby, J.-G., Lehnert, M., and Puech, M. (2010a). EAGLE: galaxy evolution with the E-ELT. *Astronomy and Geophysics*, 51(2):020000–2.

Evans, C., Yang, Y., Puech, M., Lehnert, M., and Barker, M. (2010b). EAGLE Spectroscopy of Resolved Stellar Populations Beyond the Local Group. In *Adaptative Optics for Extremely Large Telescopes*.

Evans, J. W., Macintosh, B., Poyneer, L., Morzinski, K., Severson, S., Dillon, D., Gavel, D., and Reza, L. (2006). Demonstrating sub-nm closed loop MEMS flattening. *Optics Express*, 14:5558–5570.

Flicker, R. (2009). http://homepage.mac.com/rflicker/soy.htm.

Flicker, R. and Rigaut, F. (2002). Tilt anisoplanatism and PSF retrieval in LGS MCAO using a predictive controller. In Vernet, E., Ragazzoni, R., Esposito, S., and Hubin, N., editors, *European Southern Observatory Conference and Workshop Proceedings*, volume 58 of *European Southern Observatory Conference and Workshop Proceedings*, page 377.

Flicker, R. C. (2003). Efficient first-order performance estimation for high-order adaptive optics systems. *Astron. & Astrophys.*, 405:1177–1189.

Foy, R. and Labeyrie, A. (1985). Feasibility of adaptive telescope with laser probe. *Astron. & Astrophys.*, 152:L29–L31.

Fried, D. F. (1977). Least-square fitting a wave-front distortion estimate to an array of phase-difference measurements. *Journal of the Optical Society of America*, 67:370–375.

Fried, D. L. (1982). Anisoplanatism in adaptive optics. *Journal of the Optical Society of America, vol. 72, issue 1, p.52*, 72:52+.

Fusco, T., Conan, J.-M., Michau, V., Mugnier, L. M., and Rousset, G. (1999a). Phase estimation for large field of view: application to multiconjugate adaptive optics. In Roggemann, M. C. and Bissonnette, L. R., editors, *Society of Photo-Optical Instrumentation Engineers (SPIE) Conference Series*, volume 3763 of *Society of Photo-Optical Instrumentation Engineers (SPIE) Conference Series*, pages 125–133.

Fusco, T., Conan, J.-M., Michau, V., Mugnier, L. M., and Rousset, G. (1999b). Phase estimation for large field of view: application to multiconjugate adaptive optics. In Roggemann, M. C. and Bissonnette, L. R., editors, *Society of Photo-Optical Instrumentation Engineers (SPIE) Conference Series*, volume 3763 of *Society of Photo-Optical Instrumentation Engineers (SPIE) Conference Series*, pages 125–133.

Fusco, T., Nicolle, M., Rousset, G., Michau, V., Beuzit, J.-L., and Mouillet, D. (2004). Optimization of a Shack-Hartmann-based wavefront sensor for XAO systems. In Bonaccini Calia, D., Ellerbroek, B. L., and Ragazzoni, R., editors, *Society of Photo-Optical Instrumentation Engineers (SPIE) Conference Series*, volume 5490 of *Society of Photo-Optical Instrumentation Engineers (SPIE) Conference Series*, pages 1155–1166.

Fusco, T., Petit, C., Rousset, G., Conan, J.-M., and Beuzit, J.-L. (2005). Closed-loop experimental validation of the spatially filtered Shack-Hartmann concept. *Optics LETTERS*, 30:1255–1257.

Gavel, D., Bauman, B., Dekany, R., Britton, M., and Andersen, D. (2006). Adaptive optics designs for an infrared multi-object spectrograph on TMT. In *Society of Photo-Optical Instrumentation Engineers (SPIE) Conference Series*, volume 6272 of *Society of Photo-Optical Instrumentation Engineers (SPIE) Conference Series*.

Gendron, E. and Lena, P. (1994). Astronomical adaptive optics. 1: Modal control optimization. *Astron. & Astrophys.*, 291:337–347.

Gilbert, J. R., Moler, C., and Schreiber, R. (1992). Sparse matrices in matlab: Design and implementation. *SIAM J. Matrix Anal. Appl*, 13:333–356.

Gilles, L. and Ellerbroek, B. (2006). Shack-Hartmann wavefront sensing with elongated sodium laser beacons: centroiding versus matched filtering. AO, 45:6568–6576.

Gilles, L. and Ellerbroek, B. L. (2005). *LAOS: Linear Adaptive Optics Simulator*. Thirty Meter Telescope Project. Office, TMT.AOS.TEC.05.084.DRF01.

Gilles, L. and Ellerbroek, B. L. (2010). Atmospheric tomography with separate minimum variance laser and natural guide star mode control. In *Adaptative Optics for Extremely Large Telescopes*.

Gilles, L., Wang, L., and Ellerbroek, B. (2008). Wavefront error budget development for the Thirty Meter Telescope laser guide star adaptive optics system. In *Society of Photo-Optical Instrumentation Engineers (SPIE) Conference Series*, volume 7015 of *Society of Photo-Optical Instrumentation Engineers (SPIE) Conference Series*.

Hardy, J. W. (1998). Adaptive optics for Astronomical Telescope. Technical report, Oxford University Press.

Hardy, J. W., Lefebvre, J. E., and Koliopoulos, C. L. (1977). Real-time atmospheric compensation. *Journal of the Optical Society of America (1917-1983)*, 67:360–369.

Hardy, J. W. and Thompson, L. (2000). Adaptive Optics for Astronomical Telescopes. *Physics Today*, 53(4):040000.

Henault, F., Bacon, R., Bonneville, C., Boudon, D., and Davies, R. L. (2003). MUSE: a second-generation integral-field spectrograph for the VLT. In Iye, M. and Moorwood, A. F. M., editors, *Society of Photo-Optical Instrumentation Engineers (SPIE) Conference Series*, volume 4841 of *Society of Photo-Optical Instrumentation Engineers (SPIE) Conference Series*, pages 1096–1107.

Herrmann, J. (1980). Least-squares wave-front errors of minimum norm. *Journal of the Optical Society of America*, 70:20–35.

Herrmann, J. (1981). Cross coupling and aliasing in modal wave-front estimation. *Journal of the Optical Society of America A*, 71:1917–1983.

Hubin, N., Beuzit, J. L., Gendron, E., and Demailly, L. (1994). ADONIS- a User Friendly Adaptive Optics System for the ESO 3.6m Telescope. In Merkle, F., editor, *European Southern Observatory Conference and Workshop Proceedings*, volume 48 of *European Southern Observatory Conference and Workshop Proceedings*, page 71.

Hubin, N. and Noethe, L. (1993). Active Optics, Adaptive Optics, and Laser Guide Stars. *Science*, 262:1390–1394.

Hubin, N. N., Le Louarn, M., Conzelmann, R., Delabre, B., Fedrigo, E., and Stuik, R. (2004). Ground layer AO correction for the VLT MUSE project. In Bonaccini Calia, D., Ellerbroek, B. L., and Ragazzoni, R., editors, *Society of Photo-Optical Instrumentation Engineers (SPIE) Conference Series*, volume 5490 of *Society of Photo-Optical Instrumentation Engineers (SPIE) Conference Series*, pages 846–857.

Hudgin, R. H. (1977). Wave-front reconstruction for compensated imaging. *Journal of the Optical Society of America*, 67:375.

Humphreys, R. A., Primmerman, C. A., Bradley, L. C., and Herrmann, J. (1991). Atmospheric-turbulence measurements using a synthetic beacon in the mesospheric sodium layer. *Optics Letters*, 16:1367–1369.

Jolissaint, L., Veran, J.-P., and Conan, R. (2006). Analytical modeling of adaptive optics: foundations of the phase spatial power spectrum approach. *Journal of the Optical Society of America A*, 23:382–394.

Karman, T. V. (1948). Progress in the Statistical Theory of Turbulence. *National Academy of Sciences*, 34:530–539.

Kelly C. T (1995). *Iterative Methods for Linear and Nonlinear Equation*. SIAM Frontiers inApplied Mathematics. Philadelphia.

Kern, P., Lena, P., Gigan, P., Fontanella, J.-C., Rousset, G., Merkle, F., and Gaffard, J.-P. (1989). Come-on: an adaptive optics prototype dedicated to infrared astronomy. In Swings, J.-P., editor, *Society of Photo-Optical Instrumentation Engineers (SPIE) Conference Series*, volume 1130 of *Society of Photo-Optical Instrumentation Engineers (SPIE) Conference Series*, pages 17–28.

Kolmogorov, A. (1941). The Local Structure of Turbulence in Incompressible Viscous Fluid for Very Large Reynolds' Numbers. *Akademiia Nauk SSSR Doklady*, 30:301–305.

Labeyrie, A. (1970). Attainment of Diffraction Limited Resolution in Large Telescopes by Fourier Analysing Speckle Patterns in Star Images. *Astron. & Astrophys.*, 6:85.

Lane, R. G. and Tallon, M. (1992). Wave-front reconstruction using a Shack-Hartmann sensor. AO, 31:6902–6908.

Le Louarn, M. (2010). Progress and prospects in AO simulation capabilities. In *Society of Photo-Optical Instrumentation Engineers (SPIE) Conference Series*, volume 7736 of *Society of Photo-Optical Instrumentation Engineers (SPIE) Conference Series*.

Le Louarn, M., Verinaud, C., Korkiakoski, V., and Fedrigo, E. (2004). Parallel simulation tools for AO on ELTs. In Bonaccini Calia, D., Ellerbroek, B. L., and Ragazzoni, R., editors, *Society of Photo-Optical Instrumentation Engineers (SPIE) Conference Series*, volume 5490 of *Society of Photo-Optical Instrumentation Engineers (SPIE) Conference Series*, pages 705–712.

Mahe, F. (2000). *Application d'un modele atmosph/'erique /'a l'/'etude des fluctuations d'indice de r/'efraction dans la couche limite. Influence de la scintillation sur l'analyse de front d'onde*. PhD thesis, Ph.D.-Thesis, Universit/'e de Nice [2000] vi, 242 p.

McCarthy, P. J. (2006). Galaxy formation and cosmology in the ELT era. In Whitelock, P., Dennefeld, M., and Leibundgut, B., editors, *The Scientific Requirements for Extremely Large Telescopes*, volume 232 of *IAU Symposium*, pages 119–129.

Michau, V., Rousset, G., and Fontanella, J. (1993). Wavefront Sensing from Extended Sources. In Radick, R. R., editor, *Real Time and Post Facto Solar Image Correction*, page 124.

Myers, R. M. (2010). Recent progress and perspectives for GLAO and MOAO. In *Society of Photo-Optical Instrumentation Engineers (SPIE) Conference Series*, volume 7736 of *Society of Photo-Optical Instrumentation Engineers (SPIE) Conference Series*.

Neichel, B., Fusco, T., and Conan, J.-M. (2008). Tomographic reconstruction for wide-field adaptive optics systems: Fourier domain analysis and fundamental limitations. *Journal of the Optical Society of America A*, 26:219.

Neichel, B., Rigaut, F., Bec, M., Boccas, M., and Daruich, F. (2010). The Gemini MCAO System GeMS: nearing the end of a lab-story. In *Society of Photo-Optical Instrumentation Engineers (SPIE) Conference Series*, volume 7736 of *Society of Photo-Optical Instrumentation Engineers (SPIE) Conference Series*.

Nicolle, M., Fusco, T., Michau, V., Rousset, G., Blanc, A., and Beuzit, J.-L. (2004). Ground layer adaptive optics: analysis of the wavefront sensing issue. In Bonaccini Calia, D., Ellerbroek, B. L., and Ragazzoni, R., editors, *Society of Photo-Optical Instrumentation Engineers (SPIE) Conference Series*, volume 5490 of *Society of Photo-Optical Instrumentation Engineers (SPIE) Conference Series*, pages 858–869.

Nijboer, B. R. A. (1942). *The diffraction theory of aberrations*. PhD thesis, Ph.D.-Thesis, University of Groningen, the Netherlands.

Noll, R. J. (1976). Zernike polynomials and atmospheric turbulence. *Journal of the Optical Society of America (1917-1983)*, 66:207–211.

Noll, R. J. (1978). Phase estimates from slope-type wave-front sensors. *Journal of the Optical Society of America A*, 68:139–140.

Obukhov, A. (1949). structure of the temperature field in a turbulent current. *Izv. Akad. Nauk. SSSR Georg. Geofiz*, 13:58–69.

O'Sullivan, C., Redfern, R. M., Ageorges, N., Holstenberg, H.-C., Hackenberg, W., Ott, T., Rabien, S., Davies, R., and Eckart, A. (2000). Short timescale variability of the mesospheric sodium layer. *Experimental Astronomy*, 10:147–156.

Poyneer, L. A. and Macintosh, B. (2004). Spatially filtered wave-front sensor for high-order adaptive optics. *Journal of the Optical Society of America A*, 21:810–819.

Poyneer, L. A., Palmer, D. W., LaFortune, K. N., and Bauman, B. (2005). Experimental results for correlation-based wavefront sensing. In Gruneisen, M. T., Gonglewski, J. D., and Giles, M. K., editors, *Society of Photo-Optical Instrumentation Engineers (SPIE) Conference Series*, volume 5894 of *Society of Photo-Optical Instrumentation Engineers (SPIE) Conference Series*, pages 207–220.

Puech, M., Lehnert, M., Yang, Y., Cuby, J.-G., and Morris, S. (2010). The physics of galaxy evolution with EAGLE. In *Adaptative Optics for Extremely Large Telescopes*.

Ragazzoni, R. (1996). Pupil plane wavefront sensing with an oscillating prism. *Journal of Modern Optics, Vol. 43, No. 2. (1996), pp. 289-293*, 43:289–293.

Ragazzoni, R., Diolaiti, E., Farinato, J., Fedrigo, E., Marchetti, E., Tordi, M., and Kirkman, D. (2002). Multiple field of view layer-oriented adaptive optics. Nearly whole sky coverage on 8 m class telescopes and beyond. *Astron. & Astrophys.*, 396:731–744.

Rigaut, F. (2002). Ground Conjugate Wide Field Adaptive Optics for the ELTs. In Vernet, E., Ragazzoni, R., Esposito, S., and Hubin, N., editors, *European Southern Observatory Conference and Workshop Proceedings*, volume 58 of *European Southern Observatory Conference and Workshop Proceedings*, page 11.

Rigaut, F., Arsenault, R., Kerr, J., Salmon, D., Northcott, M., Dutil, Y., and Boyer, C. (1994). The Canada-France-Hawaii Adaptive Optics Bonnette II: Simulations and Control. In Arsenault, R., editor, *Astronomy with the CFHT Adaptive Optics Bonnette*, page 11.

Rigaut, F. and Gendron, E. (1992). Laser guide star in adaptive optics - The tilt determination problem. *Astron. & Astrophys.*, 261:677–684.

Rigaut, F., Léna, P., Madec, P. Y., Rousset, G., Gendron, E., and Merkle, F. (1992). Latest Results of the COME-ON Experiment. In Ulrich, M.-H., editor, *European Southern Observatory Conference and Workshop Proceedings*, volume 42 of *European Southern Observatory Conference and Workshop Proceedings*, page 399.

Rigaut, F. J., Ellerbroek, B. L., and Flicker, R. (2000). Principles, limitations, and performance of multiconjugate adaptive optics. In Wizinowich, P. L., editor, *Society of Photo-Optical Instrumentation Engineers (SPIE) Conference Series*, volume 4007 of *Society of Photo-Optical Instrumentation Engineers (SPIE) Conference Series*, pages 1022–1031.

Robert, C., Conan, J.-M., Michau, V., Fusco, T., and Vedrenne, N. (2006). Scintillation and phase anisoplanatism in Shack-Hartmann wavefront sensing. *Journal of the Optical Society of America A*, 23:613–624.

Roddier, F. (1981). The effects of atmospheric turbulence in optical astronomy. *Progress in optics. Volume 19. Amsterdam, North-Holland Publishing Co., 1981, p. 281-376.*, 19:281–376.

Roddier, F. (2004). *Adaptive Optics in Astronomy*.

Roddier, F. and Roddier, C. (1988). Curvature sensing and compensation: a new concept in adaptive optics. In *Very Large Telescopes and their Instrumentation, Vol. 2*, volume 2, pages 667–673.

Roddier, F. J., Anuskiewicz, J., Graves, J. E., Northcott, M. J., and Roddier, C. A. (1994). Adaptive optics at the University of Hawaii I: current performance at the telescope. In Ealey, M. A. and Merkle, F., editors, *Society of Photo-Optical Instrumentation Engineers (SPIE) Conference Series*, volume 2201 of *Society of Photo-Optical Instrumentation Engineers (SPIE) Conference Series*, pages 2–9.

Roggemann, M. C. (1991). Limited degree-of-freedom adaptive optics and image reconstruction. AO, 30:4227–4233.

Roggemann, M. C. and Welsh, B. (1995). *Imaging through turbulence*.

Rousset, G., Beuzit, J. L., Hubin, N., and Gendron, E. (1994). The Come-On-Plus Adaptive Optics System: Results and Performance. In Merkle, F., editor, *European Southern Observatory Conference and Workshop Proceedings*, volume 48 of *European Southern Observatory Conference and Workshop Proceedings*, page 65.

Rousset, G., Fontanella, J. C., Kern, P., Gigan, P., and Rigaut, F. (1990). First diffraction-limited astronomical images with adaptive optics. *Astron. & Astrophys.*, 230:L29–L32.

Rousset, G., Lacombe, F., Puget, P., Hubin, N. N., and Gendron, E. (2003). NAOS, the first AO system of the VLT: on-sky performance. In Wizinowich, P. L. and Bonaccini, D., editors, *Society of Photo-Optical Instrumentation Engineers (SPIE) Conference Series*, volume 4839, pages 140–149.

Rousset, G., Madec, P.-Y., Beuzit, J.-L., and Cuby, J.-G. (1992a). The Come-On-Plus project. In *Adaptive Optics for Large Telescopes Topical Meeting*, pages 106–108.

Rousset, G., Madec, P. Y., and Rabaud, D. (1992b). Adaptive Optics Partial Correction Simulations for Two Telescope Interferometry. In Beckers, J. M. and Merkle, F., editors, *European Southern Observatory Conference and Workshop Proceedings*, volume 39 of *European Southern Observatory Conference and Workshop Proceedings*, page 1095.

Rutten, R. G. M., Myers, R. M., and Morris, T. J. (2006). The 4.2-m William Herschel Telescope as ELT testbed facility. In Whitelock, P., Dennefeld, M., and Leibundgut, B., editors, *The Scientific Requirements for Extremely Large Telescopes*, volume 232 of *IAU Symposium*, pages 496–497.

Sasiela, R. J. (1994). Wave-front correction using one or more synthetic beacons. *Journal of the Optical Society of America A*, 11:379–393.

Sauvage, J.-F., Fusco, T., Rousset, G., and Petit, C. (2007). Calibration and precompensation of noncommon path aberrations for extreme adaptive optics. *Journal of the Optical Society of America A*, 24:2334–2346.

Sauvage, J.-F., Fusco, T., Rousset, G., Petit, C., Neichel, B., Blanc, A., and Beuzit, J.-L. (2005). Fine calibration and pre-compensation of non-common path aberrations for high performance AO system. In Tyson, R. K. and Lloyd-Hart, M., editors, *Society of Photo-Optical Instrumentation Engineers (SPIE) Conference Series*, volume 5903 of *Society of Photo-Optical Instrumentation Engineers (SPIE) Conference Series*, pages 100–107.

Séchaud, M. (1999). *Wave-front compensation devices*, page 57.

Shewchuk, J. R. (1994). An introduction to the conjugate gradient method without the agonizing pain. Technical report, Pittsburgh, PA, USA.

Tallon, M. and Foy, R. (1990). Adaptive telescope with laser probe - Isoplanatism and cone effect. *Astron. & Astrophys.*, 235:549–557.

Tatarskii, V. I. (1971). *The effects of the turbulent atmosphere on wave propagation*.

Thiébaut, E. and Tallon, M. (2010). Fast minimum variance wavefront reconstruction for extremely large telescopes. *Journal of the Optical Society of America A*, 27:1046.

Thomas, S., Fusco, T., Tokovinin, A., Nicolle, M., Michau, V., and Rousset, G. (2006). Comparison of centroid computation algorithms in a Shack-Hartmann sensor. *MNRAS*, 371:323–336.

Thompson, L. A. and Gardner, C. S. (1987). Experiments on laser guide stars at Mauna Kea Observatory for adaptive imaging in astronomy. *Nature*, 328:229–231.

Tokovinin, A. (2004). Seeing Improvement with Ground-Layer Adaptive Optics. *Publications of ASP*, 116:941–951.

Tyler, G. A. (1994). Rapid evaluation of d_0: the effective diameter of a laser- guide-star adaptive-optics system. *Journal of the Optical Society of America A*, 11:325–338.

Tyson, R. K. (1991). *Principles of adaptive optics*.

van Dam, M. A., Le Mignant, D., and Macintosh, B. A. (2004). Performance of the Keck Observatory Adaptive-Optics System. *Applied Optics*, 43:5458–5467.

Van Trees Harry. L. (1968). *Detection, Estimation, and Modulation Theor*. John Wiley and Sons.

Veran, J.-P., Rigaut, F., Maitre, H., and Rouan, D. (1997). Estimation of the adaptive optics long-exposure point-spread function using control loop data. *Journal of the Optical Society of America A*, 14:3057–3069.

Viard, E. (2001). *Systemes d'optique adaptive avec etoiles laser : du systeme classique aux methodes multi-conjugees*. PhD thesis, Ph.D.-Thesis, Universite de Grenoble, [2001] vi, 216 p.

Wang, J. Y. and Markey, J. K. (1978). Modal compensation of atmospheric turbulence phase distortion. *Journal of the Optical Society of America (1917-1983)*, 68:78–87.

Welsh, B. M. and Gardner, C. S. (1991). Effects of turbulence-induced anisoplanatism on the imaging performance of adaptive-astronomical telescopes using laser guide stars. *Journal of the Optical Society of America A*, 8:69–80.

Wizinowich, P. L., Le Mignant, D., Bouchez, A. H., Campbell, R. D., and Chin, J. C. Y. (2006). The W. M. Keck Observatory Laser Guide Star Adaptive Optics System: Overview. *Publ. Astron. Soc. Pac.*, 118:297–309.

Zernike, F. (1934). Diffraction theory of the knife-edge test and its improved form, the phase-contrast method. *MNRAS*, 94:377–384.